

STATUS OF THESIS

Title of thesis Minimising False Detection of Retinal Microaneurysms using Curvelet, Hessian and Regional Feature Detection Techniques

I SYED AYAZ ALI SHAH

here by allow my thesis to be placed at the Information Resource Center (IRC) of Universiti Teknologi PETRONAS (UTP) with the following conditions:

1. The thesis becomes the property of UTP
2. The IRC of UTP may make copies of the thesis for academic purposes only.
3. This thesis is classified as

Confidential

Non-confidential

If this thesis is confidential, please state the reason:

The contents of the thesis will remain confidential for _____ years.

Remarks on disclosure:

Endorsed by

Signature of Author

Signature of Supervisor

Permanent address: Jeewan Mull out
side Hushtnagry gate Peshawar city
Khyber Pakhtunkhwa Khwa Pakistan

Name of Supervisor
Assoc. Prof. Dr. Tang Tong Boon

Date : August 2017

Date : August 2017

UNIVERSITI TEKNOLOGI PETRONAS

MINIMISING FALSE DETECTION OF RETINAL MICROANEURYSMS USING
CURVELET, HESSIAN AND REGIONAL FEATURE DETECTION
TECHNIQUES

by

SYED AYZ ALI SHAH

The undersigned certify that they have read, and recommend to the Postgraduate Studies Program for acceptance of this thesis for the fulfillment of the requirements for the degree stated.

Signature:

Main Supervisor:

Assoc.Prof. Dr. Tang Tong Boon

Signature:

Co-Supervisor:

Assoc. Prof. Dr. Ibrahima Faye

Signature:

Head of Department:

Assoc. Prof. Ir. Dr Nursyarizal Bin Mohd Nor

Date:

August 2017

MINIMISING FALSE DETECTION OF RETINAL MICROANEURYSMS USING
CURVELET, HESSIAN AND REGIONAL FEATURE DETECTION
TECHNIQUES

by

SYED AYAZ ALI SHAH

A Thesis

Submitted to the Postgraduate Studies Program

as a Requirement for the Degree of

DOCTOR OF PHILOSOPHY

ELECTRICAL AND ELECTRONIC ENGINEERING

UNIVERSITI TEKNOLOGI PETRONAS

BANDAR SERI ISKANDAR,

PERAK

AUGUST 2017

DECLARATION OF THESIS

Title of thesis

Minimising False Detection of Retinal Microaneurysms using Curvelet, Hessian and Regional Feature Detection Techniques

I SYED AYAZ ALISHAH

hereby declare that the thesis is based on my original work except for quotations and citations which have been duly acknowledged. I also declare that it has not been previously or concurrently submitted for any other degree at UTP or other institutions.

Witnessed by

Signature of Author

Signature of Supervisor

Permanent address Jeewan Mull out
side Hushtnagry gate, Peshawar city
Khyber Pakhtunkhwa Khwa, Pakistan

Name of Supervisor
Assoc. Prof. Dr. Tang Tong Boon

Date : August 2017

Date : August 2017

DEDICATION

To my parents, my wife and my children, you were the source of this courage that I have to finish this work and to achieve the level that I am in. Whatever I do will not be enough to repay for what you did to me through my life. Thank you.

ACKNOWLEDGEMENTS

All praise to Allah the most merciful and the most generous for giving us the ability to finish this task and to achieve this level of knowledge. Without Allah guidance and gifts I would never be able to finish anything in my life.

I am thankful to my supervisor Associate Professor Dr. Tang Tong Boon for his supervision, advice, and guidance. I am also thankful to my co-supervisor Associate Professor Dr. Ibrahima Faye who guided me and encouraged me always. I am grateful to Universiti Teknologi PETRONAS who provided me funding to do my research. I would like to mention my lovely friends in UTP especially in CISIR who always helped and encouraged me in this long journey of PhD.

Finally, I am thankful to my father, mother, wife, children, and father in law and mother in law who suffered a lot due to my studies and have given me time to do the work.

Thanks to all of you.

ABSTRACT

Diabetic Retinopathy (DR) is one of leading causes of blindness. It can be diagnosed from symptoms like hemorrhages, exudates, microaneurysm (MA), blood vessels areas etc. Among these symptoms, MAs, are said to be the first sign of DR. Hence their detection is very important. Due to low and varying contrast and noise inherited in color fundus images, MA detection in color fundus images is a very challenging task. Although many state of the art algorithms have been proposed, many MAs are often missed in the process, thus resulting in low sensitivity. To achieve a higher sensitivity with comparable specificity, there is a need for addressing the issue of false positives (F_P). Automated microaneurysm detection system is proposed in which F_P by category are addressed. The categories of F_P are (i) those from background (ii) from the blood vessel (iii) and from other objects/ lesions in the image. In the proposed system, candidate MAs are extracted in two parallel modules. In module one, blood vessels are removed from preprocessed green band image and preliminary MA candidates are selected by local thresholding technique. In module two, based on statistical features, the image background is estimated. The results from the two modules allowed us to identify preliminary MA candidates which are also present in the image foreground. A collection set of features is fed to a rule-based classifier to classify the candidates into true MAs and false MAs. The proposed system is tested with Retinopathy Online Challenge database. The automated system detected 162 MAs out of 336, thus achieved a sensitivity of 48.21% with 65 false positives per image. The retinal vessel segmentation was further refined to reduce F_P . Image homogenization was proposed to ameliorate the effects of low and varying contrast. The proposed blood vessel segmentation system uses local and Hessian features and classifies each pixel into vessel and non-vessel using a LMSE classifier. We achieved a sensitivity of 0.77 with 0.0283 FPR on DRIVE test images database. Counting MA is a means to measure the progression of DR. Hence, the proposed system may be deployed to monitor the progression of DR at early stage in population.

ABSTRAK

Diabetic retinopathy (DR) adalah penyebab utama kepada masalah hilangnya daya penglihatan boleh didiagnosis melalui simtom-simtom seperti hemorrhages, exudates, microaneurysm (MA), pembuluh darah dll. Di antara simtom ini, MA merupakan tanda-tanda awal DR. Maka pengesanan MA adalah amat penting. Disebabkan kontra imej fundus yang rendah dan sentiasa berubah serta terdapat hingar maka pengesanan imej warna fundus merupakan tugas yang sukar. Walaupun terdapat banyak pengaturcaraan terkini yang dicadangkan bagi pengesanan MA namun masih lagi terdapat kekurangan kerana kepekaan yang rendah. Kajian ini mencadangkan sistem microaneurysm secara automatic di mana ia memperincikan false positive mengikut kategori. Kategori Fp adalah seperti (i) dari latar belakang (ii) dari pembuluh darah (iii) dari objek lain/lika di dalam imej. Di dalam sistem ini, sampel MA diekstrak kepada dua langkah secara selari. Langkah pertama imej pembuluh darah diasingkan sebelum proses spektrum imej hijau dan sampel MA ini dipilih melalui teknik nilai ambang. Langkah kedua ialah dengan menggunakan elemen statistik bagi menganggar imej latar belakang. Ciri-ciri pengelasan disuap kepada pegelas berasaskan peraturan bagi mencirikan calon-calon MA dan bukan MA. Sistem ini diuji dengan pangkalan data Retinopathy Online Challenge. Sistem automatic ini mengesan 162 MA daripada 336 jesteru mencapai sensitiviti sebanyak 48.21% dengan 65 false positives bagi setiap imej. Segmentasi pembuluh retina diperhalusi bagi mengurangkan Fp. Penyeragaman imej dicadangkan bagi menyelesaikan kesan kontra yang berubah dan rendah. Cadangan tersebut menggunakan ciri local dan Hessian serta memperincikan piksel kepada pembuluh dan bukan pembuluh menggunakan perincian LMSE. Sensitiviti sebanyak 0.77 dengan 0.0283 FPR dapat dicapai dengan menggunakan imej-imej pengujian pangkalan data DRIVE. Mengira MA bermaksud mengukur perkembangan DR. Maka sistem yang dicadangkan boleh

dibangunkan bagi memantau perkembangan DR pada peringkat awal.

In compliance with the terms of the Copyright Act 1987 and the IP Policy of the university, the copyright of this thesis has been reassigned by the author to the legal entity of the university,

Institute of Technology PETRONAS Sdn Bhd.

Due acknowledgement shall always be made of the use of any material contained in, or derived from, this thesis.

© Syed Ayaz Ali Shah, 2017
Institute of Technology PETRONAS Sdn Bhd
All rights reserved.

TABLE OF CONTENT

ABSTRACT	vii
ABSTRAK.....	vii
LIST OF FIGURES	xiv
LIST OF TABLES.....	xvi
LIST OF ABBREVIATIONS.....	xvii
BACKGROUND ESTIMATION.....	xvii
LIST OF SYMBOLS	xix
CHAPTER 1 INTRODUCTION	1
1.1 The Human Eye	1
1.1.1 Layers of the Eye.....	2
1.2 Diabetic Retinopathy (DR)	3
1.2.1 Stages of Diabetic Retinopathy	4
1.3 Problem Statement.....	6
1.4 Research Hypotheses	7
1.5 Objectives of the Study.....	7
1.6 Scope of the thesis	7
1.7 Organizational Structure of the Thesis	8
CHAPTER 2 LITERATURE REVIEW	11
2.1 Overview.....	11
2.2 Fundus Photography	11
2.2.1 Fluorescein angiography	12
2.2.2 Fundus Photography.....	12
2.2.3 Ultrasonography	14
2.2.4 Optical Coherence Tomography	14
2.3 Preprocessing.....	15
2.3.1 Correction of Non-uniform Illumination.....	15
2.3.2 Color Normalization.....	16
2.3.3 Contrast Enhancement.....	18
2.4 Microaneurysm Detection	19
2.4.1 Mathematical Morphology	20
2.4.2 Matched Filter	22

2.4.3 Neural Networks.....	22
2.4.4 Miscellaneous Approaches	23
2.5 Summary of the Literature Review of Microaneurysm Detection	26
2.6 Blood Vessel Segmentation	28
2.6.1 Filter based Blood Vessel Detection	29
2.6.2 Multiscale Based Blood Vessel Detection	32
2.6.3 Mathematical Morphology based Blood Vessel Detection.....	33
2.6.4 Hierarchical based Blood Vessel Detection	35
2.6.5 Active Contours and Model based Blood Vessel Detection	36
2.6.6 Miscellaneous Approaches for Blood Vessel Detection	37
2.7 Summary of the Literature Review of Blood Vessel Segmentation.....	38
2.8 Summary.....	40
CHAPTER 3 METHODOLOGY OF AUTOMATED MICROANEURYSM	
DETECTION	40
3.1 Overview.....	40
3.2 Materials and Method for Microaneurysm Detection	41
3.2.1 Materials for MA detection	41
3.2.2 Method for Microaneurysm Detection	41
3.2.2.1 Candidate Selection	43
a) Preprocessing	44
b) Blood Vessel Extraction Based on Gabor Wavelet	44
c) MA candidate selection using local thresholding	47
d) Background Estimation and Removal of False Positives:	49
3.2.2.2 Candidate Feature Extraction.....	50
3.2.2.3 Candidate Classification MA and false MA	60
3.2.3 Evaluation Metrics for Microaneurysm Detection.....	61
3.3 Summary.....	61
CHAPTER 4 RESULTS AND DISCUSSION ON MICROANEURYSM	
DETECTION	63
4.1 Overview.....	63
4.2 Automated Microaneurysm Detection.....	63
4.2.1 Blood Vessel Segmentation Based on Gabor Wavelet	63
4.2.2 MA Candidate Selection	65
4.2.3 Background Estimation	65

4.2.4 Color Based Features.....	66
4.2.5 Hessian Based Features	66
4.2.6 Curvelet Based Features	67
4.3 The Overall Results and Discussion	67
4.4 Summary.....	71
CHAPTER 5 BLOOD VESSEL SEGMENTATION METHODOLOGY, RESULTS AND DISCUSSION.....	73
5.1 Overview.....	73
5.2 Materials and Method for Blood Vessel Segmentation	74
5.2.1 Materials for Blood Vessel Segmentation.....	74
5.2.2 Method of Blood Vessel Segmentation	74
5.2.2.1 Image Preprocessing	74
5.2.2.2 Features Extraction	75
5.2.2.3 Pixel Classification	78
5.2.2.4 Post processing.....	79
5.2.3 Evaluation Metrics for Blood Vessel Segmentation	82
5.3 Results and discussion of Blood Vessel Segmentation	84
5.3.1 Preprocessing.....	84
5.3.2 Pixel Classification.....	84
5.3.2.1 Results at the Output of Classifier	84
5.3.2.2 Post Processing Results.....	85
5.3.2.3 Results after Background Estimation Post Processing	86
5.3.2.4 Results after Mathematical Morphology Based Post Processing	86
5.3.3 Results on the Test Images	86
5.3.4 Discussion and Comparison	91
5.4 Summary.....	94
CHAPTER 6 CONCLUSION AND FUTURE WORK	97
6.1 Overview.....	97
6.2 Conclusion of the Microaneurysms Detection System.....	97
6.3 Conclusion of the Blood Vessel Detection System	98
6.4 Future Work.....	99
6.4.1 MA Detection	99
6.4.2 Blood Vessel Segmentation.....	100

APPENDIX A LIST OF PUBLICATION.....	116
Journal Publications	117
Conference Publications.....	117
APPENDIX B FUNDUS IMAGES DATASETS	118
APPENDIX C TECHNICAL TERMS	121

LIST OF FIGURES

Figure 1.1: Different structures in human eye[2].....	2
Figure 1.2: Different layers in the eye[4].....	3
Figure 1.3: (a) encircled bright lesions are exudates while encircled red one are hemorrhages (b) encircled yellowish are drusen (c) encircled red is microaneurysm... 4	4
Figure 1.4: Organization of the thesis.....	9
Figure 2.1: Fluorescein angiography shows scattered microaneurysms [26]	13
Figure 2.2: Standard color fundus image, 30° of the posterior pole	14
Figure 2.3: Based on 7-field color fundus photography, same patients montage image as in Figure 2.2.....	14
Figure 2.4: Non-uniform illumination correction, (a) original colored image, (b) green channel image, (c), background estimated image and (d) non-uniform illumination corrected image, obtained by dividing the original image by the filtered image.....	17
Figure 2.5: Color normalization, are two different coloration images, while (c) and (d) are the color normalized images of (a) and (b) respectively, reproduced from [46] ...	18
Figure 2.6: Contrast enhancement	19
Figure 2.7: Generalized block diagram of CAD system for MA detection	20
Figure 2.8: Angiofluorography (positive image), MAs are the white dots.....	21
Figure 2.9: Generalized block diagram of automated blood vessel segmentation	31
Figure 3.1: Automated MA detection system flow chart.....	43
Figure 3.2: Preprocessing of fundus image. (a) Original color fundus image (b) Green channel (c) background estimation (d) Pre-processed image	46
Figure 3.3: Preprocessing to artificially increasing the ROI. (a) original ROI (b) artificially increased ROI, reproduced from [94]	46
Figure 3.4: Supervised pixel classification approach, reproduced from[94]	48
Figure 3.5: (a) color image (b) background estimated image (G_{fb})	50
Figure 3.6: HSV color space	53
Figure 3.7: Curvelet tiling of space and frequency, reproduced from [125]	56
Figure 3.8: The figure illustrates the basic digital tiling. The windows $U_{j,l}$, smoothly localize, reproduced from [100].....	57
Figure 3.9: Steps of Curvelet Transform, reproduce from [92].....	59
Figure 4.1: Examples of BV segmentation based on Gabor Wavelet. Right column colored ROC images, left column segmented vessels.	64

Figure 4.2: At high threshold MA (encircled in red) in (a) is detected and in (b) is missed. At low threshold, MA in (a) large cluster of pixels (c), but the MA previously missed in (b) can now be detected (d)	66
Figure 4.3: Examples of MA that are very close to the BVs but detected by the proposed system: (a)–(d) full color images and (e)–(h) in green band.....	69
Figure 4.4: FROC plot of the proposed system	70
Figure 4.5: Objects encircled in blue are T_P , encircled in red are F_N , whereas objects inside the red squares are F_P , (a) full-color images while (b) in green band	71
Figure 4.6: Different cases where the proposed system was unable to detect the MAs: (a)–(d) examples of missed MA because the center pixel does not have the minimum intensity, (e)–(h) examples of missed MA because their colors are very faint, and (i)–(l) examples of missed MA due to abnormal shape.....	72
Figure 5.1: Flow chart of the proposed blood vessel segmentation system.....	75
Figure 5.2: The second order derivative of a Gaussian kernel probes inside/outside contrast of the range $(-1,1)$, reproduced from [137]	78
Figure 5.3: Left original image, right top hat transformed image	81
Figure 5.4: a) color fundus image (b) gray channel image (c) enhanced gray channel (d) homogenized background image with vessels	85
Figure 5.5: Left column color images while right column segmented vessel. Shown in top row is image with the best sensitivity and bottom row image with the best specificity, green pixel are the F_N and red are the F_P	87
Figure 5.6: Image achieving the best accuracy. Top row: left color image, right ground truth. Bottom row: left segmented BV while on the right, green pixel are the F_N and red are the F_P	90
Figure 5.7: Image achieving the worst accuracy. Top row: left color image and right ground truth. Bottom row: Left segmented BV, right, green pixel represent the F_N and red are the F_P	91
Figure 5.8: 1st and 2 nd column are respectively colored and green patches of the image, 3 rd and 4 th column patches represents the vessel detected using Gabor wavelet method and the proposed method respectively	93

LIST OF TABLES

Table 1.1: Different stages of DR	5
Table 2.1: Summary of the most relevant approaches for MA detection	26
Table 2.2: Summary of the most relevant approaches for BV segmentation	38
Table 3.1: Types of images used in the proposed approach	41
Table 3.2 : Parameter values	60
Table 4.1: Result comparison of different MA detection methods.....	69
Table 5.1: Image by image results of the developed system on test dataset based on first manual segmentation	87
Table 5.2: Image by image results of the developed system on test dataset based on second manual segmentation	88
Table 5.3: Comparative performance of the proposed method with existing works ...	92

LIST OF ABBREVIATIONS

AAO	American Academy of Ophthalmology
CAD	Computer Aided Diagnosis
2D	Two Dimensional
3D	Three Dimensional
dB	Decibel
dB _i	Decibel Isotropic
dBW	Decibel Watt
DCT	Discrete Cosine Transform
DST	Discrete Sine Transform
F _N	False Negative
F _P	False Positives
FPPI	Average Number of False Positives Per Image
FPR	False Positive Rate
G-BV	Image obtained after removing blood vessel from Gnpr
Gcand	Image containing candidate MA after local thresholding and removal false positives using background estimation
GLT	Image obtained by binerizing G-BV
G _n	Green Band
G _{npr}	Preprocessed image for MA detection
G _r	Red Band
G _y	Gray Band
H _s	Hemorrhages
ImgFinal _{BV}	The final image containing the segmented blood vessel
ImgFP _{removed}	Blood Vessel image obtained after removal of FP using

BACKGROUND ESTIMATION

ImgBV_Rconst	Image obtained after reconstruction of the vessel pixels after FP removal step
ImgMod	Image containing blood vessel before the length filtering step
ImgTHt	Image containing blood vessel obtained using THT
MA	Microaneurysm
MF	Matched Filter
MM	Mathematical Morphology
THT	Top Hat Transform
T _N	True Negative
T _P	True Positive
TPR	True Positive Rate

LIST OF SYMBOLS

B	Linear Operator
c	Speed of light (3×10^8 m/sec)
C	Set of Complex numbers
e	Euler's constant
E_0	Electric field magnitude in V/m
E	Electric Field
f	Arbitrary function; Frequency
$\text{Img}_{\text{FP_removed}}$	False Positive Removed Image
F	Fast Fourier transform
F^{-1}	Inverse fast Fourier transform
Δz	Equidistance Height Grid

CHAPTER 1

INTRODUCTION

1.1 The Human Eye

Cameras are developed to mimic the eyes, similar to camera where lens focuses light on film, cornea focuses light on retina [1]. The eye gives us the sense of sight. In comparison with other four senses, we may observe and learn more about the surrounding world by using our eyes. Eye detects and converts the light reflected or emitted by objects, into neural impulses which are processed by different parts in brain. Thus eyes allow us to see and interpret colors, shapes and dimensions. As shown in Figure 1.1, three main structures of an eye are as follows.

1. The pupil, a black-looking aperture, through which light enters the eye. Due to absorbing pigments in the retina, it looks dark in color. It is round in shape. Its size varies depending upon the amount of light allowed to enter the eye. The size of the pupil is controlled by iris.
2. The iris is colored circular muscle, giving us our eye's color (Figure 1.1). Due to different amounts of eumelanin (brown/black melanins) and pheomelanin (red/yellow melanins), iris may have different colors, thus people with different colored eyes. This circular muscle, regulates the amount of light by controlling the size of the pupil.
3. White part of the eye or the sclera, is part of the supporting wall of the eyeball. The sclera is continuous with the cornea (transparent, protective outer layer). Furthermore the sclera is in continuity with the dura of the central nervous system, as shown in Figure 1.1.

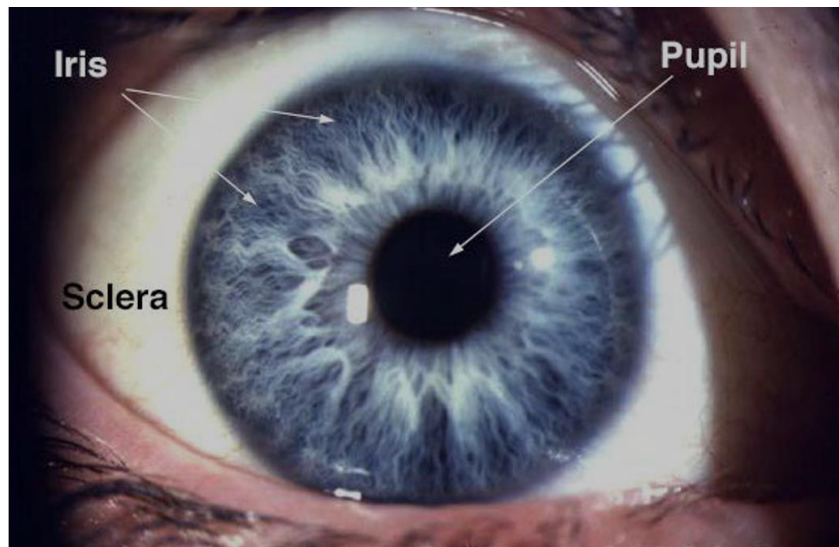


Figure 1.1: Different structures in human eye[2]

1.1.1 Layers of the Eye

There are three layers in the thick wall of the eye. [3], as shown in Figure 1.2.

1. The sclera is the first or outer most layer of the eye, and it is the white part of the eye [3]. The eye ball gets its white color from sclera and the muscles that control eye movement are connected to it. It extends from the cornea to the optic nerve at the back of the eye. It is a thick layer and protects the eye. The eye gets its structural stability and shape due to sclera. A clear mucus membrane called conjunctiva covers the sclera. This membrane helps in lubricating the eye.
2. The choroid is the second layer of the eye. It is made up of blood vessels and dense pigment[3]. The nutrients to the retinal layers are supplied by these blood vessels. The pigmentation of the choroid layer is visible in iris. In the center of iris, there is a round opening called pupil. The change in its size controls both the quantity of light incident on the retina and retinal image quality. Lens which is solid ellipsoid but elastic and transparent resides behind the iris. It focuses the light on the retina, which is the third and innermost layer of tissue.
3. The retina is a network of nerve cells, notably the photoreceptors (rods and cones), and nerve fibers [3]. The function of the photoreceptors is to absorb and convert the visible light into nerve impulses. These impulses via optic nerve are

sent to the brain. Macula, located in the central part of the retina, is the specialized area for perceiving color and fine detail. Fovea is the center of macula and contains only cone photoreceptors. The optic nerve is composed of millions of nerve fibers. The function of these fibers is to send the information received from the eye to the brain visual cortex.

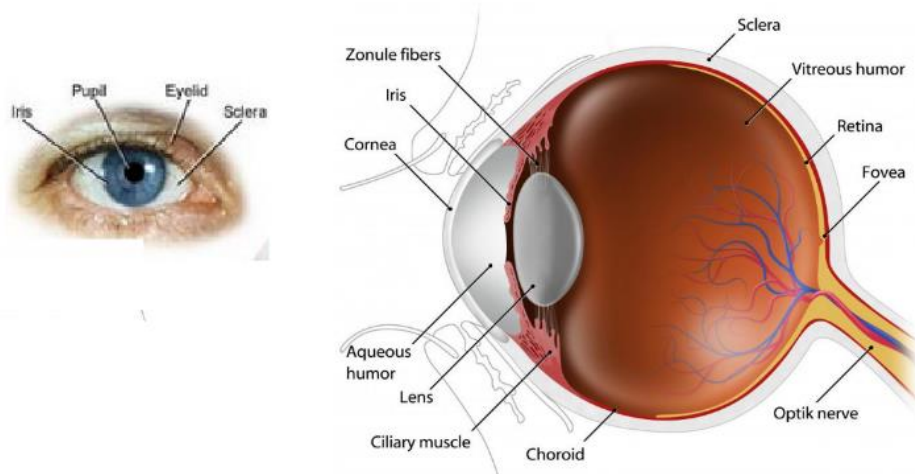


Figure 1.2: Different layers in the eye[4]

1.2 Diabetic Retinopathy (DR)

DR is a complication of diabetes mellitus and the second most common cause of blindness and the most important cause of blindness in the working age population[5]. Diabetes affects over 2% of the population and retinal screening is very costly, both in terms of technical resources and personnel [6]. Majority of the people suffering from diabetes mellitus will eventually develop this eye disease. It can only be controlled if detected early. With the advent of digital fundus photograph technology and availability of fast computers, automatic systems are being designed to detect DR. DR is known as a silent disease due to the fact that patient can only realize it when the retinal changes have developed into such a condition where treatment is complicated and cannot be done[7]. It can be diagnosed from symptoms like:

1. Hemorrhages: They are red in color similar to microaneurysms. Their shape may be large round, hemispherical or flame shaped or irregular. Hemorrhages are shown in Figure 1.3 (a).

2. Exudates: They may be soft or hard. Soft exudates also called cotton-wool-spots have fluffy indistinct margins but the hard exudates are small, discrete waxy looking with crenated margins[8]. Exudates are shown in Figure 1.3 (a)
3. Drusen: They are also called colloid bodies. They are numerous, minute, yellowish lesions [8] as shown in the Figure 1.3 (b).
4. Microaneurysms: They are round in shape and they have red color similar to blood vessels[9]. Their diameter lies normally between $10\mu\text{m}$ and $100\mu\text{m}$, but it is always smaller than $125\mu\text{m}$ [10, 11]. Example of MA is shown in Figure 1.3 (c).
5. Neovascularization/Blood vessels areas: To compensate for hypoxia, fresh vascular channels may be formed in the retina.

Among these symptoms, MAs are the first to appear. Hence their detection is important.

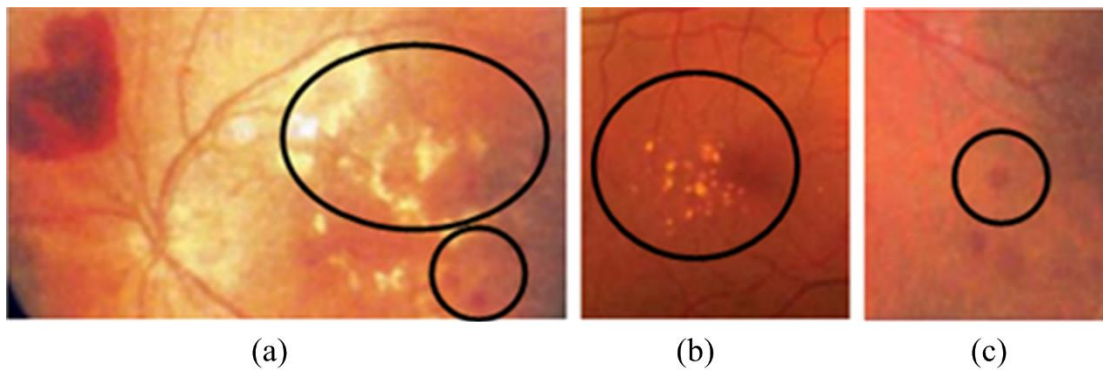


Figure 1.3: (a) encircled bright lesions are exudates while encircled red one are hemorrhages (b) encircled yellowish are drusen (c) encircled red is microaneurysm

1.2.1 Stages of Diabetic Retinopathy

For healthy people, if the blood sugar level were too high, insulin will be released by a group of special cells in the pancreas (called beta cells). Insulin is a hormone and it causes cells to take in sugar as energy or to be stored as fat. This causes blood sugar

level to go back down. The body needs insulin to utilize sugar as a source of energy. Diabetes is a chronic disease, in which the body either cannot produce enough insulin or cannot properly use the insulin it produces. Thus diabetes has two types, type I and type II. In case of type I diabetes, the beta cells of pancreases are mistakenly attacked and killed by the immune system. Thus no, or very little, insulin is released into the body. In case of type II, insulin is produced but cannot be utilized by the body. Ninety percent of the people suffering from diabetes are type II. During the first twenty years of having diabetes, nearly all patients with type I and more than sixty percent of patients with type II will develop DR [12]. DR can be categorized into two main categories i.e. Non Proliferative DR (NPDR) and Proliferative DR (PDR). According to the international classification by American Academy of Ophthalmology (AAO), NPDR is graded as: No DR, mild NPDR, moderate NPDR and severe NPDR. Table 1.1 lists different stages of DR[13]. Mild non-proliferative diabetic retinopathy (NPDR) is indicated by no haemorrhage (H_s) and the count of microaneurysms (MAs) equals to or less than 5; while DR stage will be considered as severe NPDR if there are more than 15 MAs or H_s is more than 5. Neovessel on the optic disc indicates the progression to the stage of proliferative diabetic retinopathy (PDR). Microaneurysm detection in color fundus images is very challenging and is still an open issue. Some of the approaches for MA detection using color fundus images are scale-adapted blob analysis with semi-supervised learning scheme proposed by [14] while local rotating cross-section profile analysis was used for MA detection by [15, 16] and [17] proposed multiscale correlation coefficients for the detection of MA. Hough transform based approach was proposed by [18]. Diameter closing based approach was used by [11]. Although these algorithms are good but to achieve comparable specificity, many MAs are still missed, thus resulting in lower sensitivity (see appendix C). To achieve a higher sensitivity with comparable specificity, there is a need for addressing the issue of false positives. One alternative approach may be multiscale based features for MA description. As there is similarity between vision and multiscale image processing[19, 20], hence Curvelet Transform being, multiscale and capable of extracting geometric properties of structures, may be used.

Table 1.1: Different stages of DR

DR Stage	Findings in color fundus image
----------	--------------------------------

No DR	No apparent diabetic changes, MA=0 and Hs=0
Mild NPDR	$1 \leq MA \leq 5$, Hs=0
Moderate NPDR	$5 < MA < 15$, $0 < Hs \leq 5$
Severe NPDR	$15 \leq MA$ or $Hs > 5$
PDR	Neovessel on the disc

1.3 Problem Statement

The detection of MA is not only important for the screening of DR but also it is very important for monitoring the progression of DR. However MA detection is a very challenging task using color fundus images. Color fundus images suffer from low and varying contrast, non-uniform illumination and noise. These result in fuzzy boundaries of MA. Moreover, the shape of the MA is not always circular. The color of the background in retinal images is reddish, making the MA detection even more difficult. In addition, MA detectors based on intensity may falsely detect parts of blood vessels as MA and blood vessels are both red in color as shown in Figure 1.3(c). Hence, blood vessels should be detected and removed more accurately. The main categories of F_P are therefore image background, blood vessels and other objects/lesions in the image.

The problems that have been identified from literature review and which will be investigated are as follows:

1. Due to irregular shape, poor contrast and reddish background, the detection of microaneurysms is challenging using state of the art methods, with limited sensitivity of MA detection.
2. Retinal vasculature is a major feature in the fundus image and is required to be removed before MA detection. Any remaining parts of vasculature after retinal vessel segmentation will cause false MA detection and hence reduce the system specificity in MA detection.

1.4 Research Hypotheses

On the basis of problem statement, it is hypothesized that:

1. Addressing the false positives by category and using geometry based multiscale techniques may help to improve sensitivity of microaneurysm detection.
2. Preprocessing color fundus images with non-uniform illumination, low and varying contrast together with multiscale feature based technique (e.g. Hessian Matrix) may improve the blood vessel segmentation.

1.5 Objectives of the Study

In this research work we aim to design and develop a computer aided diagnosis (CAD) system that can be used as a monitoring or screening system for diabetic retinopathy. The proposed system may assist the ophthalmologists in reducing their workload. On the basis of the hypotheses, the research objectives are defined as:

1. To design and develop MA detection algorithm based on category of false candidates and geometry based multiscale technique such as Curvelet transform, to increase the sensitivity in early detection of DR.
2. To design and develop blood vessel segmentation technique using multiscale technique.

1.6 Scope of the thesis

The scope of the thesis is limited to color fundus images only. This study involves automated detection of diabetic retinopathy using color retinal images. It consists of two parts. In part I, the primary aim is to design and develop an automated MA detection with high sensitivity. The dataset for training and testing the MA detection will be from Retinopathy Online Challenge (ROC). The algorithm for MA detection is based on Hessian features, color features and Curvelet Transform. The second part of the study is to design and develop blood vessel segmentation system. For blood vessel

segmentation publicly available dataset called Digital Retinal Images for Vessel Extraction (DRIVE) will be utilized. The algorithm for blood vessel segmentation is based on image homogenization, regional features and Hessian features at multiple scale. The expected outcomes of the study are:

- I. An automated MA detection system which can be deployed to assist the clinicians in screening and or monitoring the progression of diabetic retinopathy.
- II. Blood vessel segmentation system which can be deployed to diagnosis of different diseases such cardiovascular disease, stroke, glaucoma, DR, hypertension etc.

Following are the knowledge contributions of the proposed study:

- 1) The application of Curvelet Transform for MA detection
- 2) The application of category based approach (background, blood vessel and other objects/lesions) in feature removal to extract the true candidates of MA.
- 3) The introduction of homogenization technique using per pixel contrast to design and develop blood vessel segmentation system, together with a LMSE classifier to achieve results comparable to those of state-of-art methods.

1.7 Organizational Structure of the Thesis

The organization of the thesis is as shown in Figure 1.4. The thesis comprises of five chapters. Chapter 2 describes the literature review, and in Chapter 3 methodology of automated microaneurysm system is described. In Chapter 4, the results on MA detection are presented. The methodology of blood vessel segmentation and results are given in Chapter 5. Chapter 6 concludes the thesis and discusses about future work. The publications resulted from this work are listed in Appendix A. The weblinks for downloading the fundus image datasets are given in Appendix B while technical terms are explained in Appendix C.

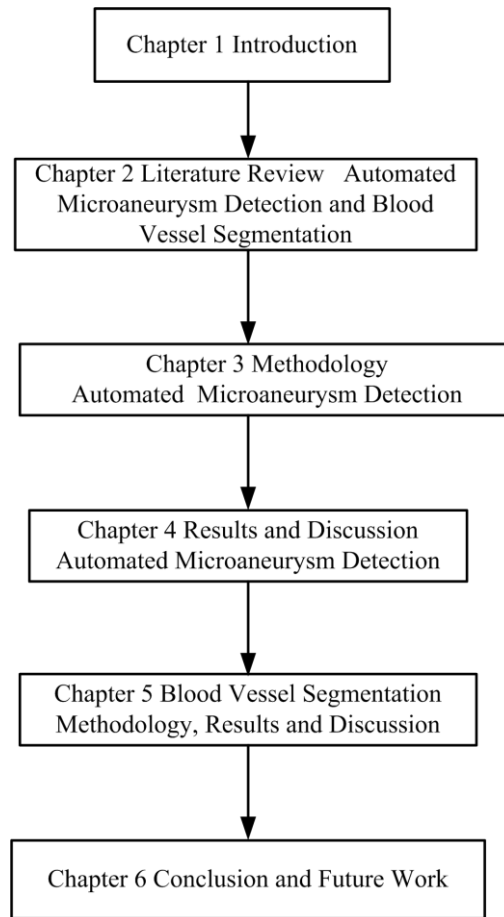


Figure 1.4: Organization of the thesis

CHAPTER 2

LITERATURE REVIEW

2.1 Overview

Retinal image analysis is not only important for the diagnosis of diabetic retinopathy but it has showed potential in the diagnosis of many other systematic diseases and medical conditions such as heart, kidney, stroke etc. It is due to the fact that many medical conditions do manifest their symptoms in eyes. This chapter describes literature review of the different preprocessing techniques, state of the art methods designed for detection of microaneurysm and blood vessel segmentation.

In section 2.2 fundus photography is described while in section 2.3 the preprocessing is discussed. Literature review about microaneurysm is described in section 2.4 and it is summarized in section 2.5. Literature review of blood vessel segmentation is given in section 2.6. Section 2.7 describes the summary of the literature review of blood vessel segmentation. Finally chapter is concluded with section 2.8.

2.2 Fundus Photography

Fundus photography is an imaging technique to image the back of eye called fundus. The fundus camera that is used for fundus photography consists of an intricate microscope attached to a flashed enabled camera[21]. The central and peripheral retina, optic disc and macula are the main structures that are captured on fundus images. Some of the applications of the fundus photography are:

- a) To record abnormalities of disease affecting the eye.

- b) To follow up on the progress of the eye condition/disease such as diabetes, age-macular degeneration (AMD), Neoplasm of the choroid, glaucoma, cranial nerves etc.
- c) For monitoring the progression of certain eye conditions/diseases.
- d) For diagnosing different diseases like arteriosclerosis, cardiovascular disease, stroke, glaucoma, diabetic retinopathy etc. [5].

Among these conditions, DR and glaucoma result in vision loss. In fact these two are the leading causes of vision loss. Moreover in eye, we can observe the vascular condition in vivo. Therefore, detection and analysis of retinal blood vessels is an extremely important task. To improve the accuracy of any automated DR detection system, the detection and segmentation of the blood vessels plays a vital role. Following are some of the techniques used for fundus photography.

2.2.1 Fluorescein angiography

Gass et al. in 1967 [22], introduced Fluorescein angiography (FA) into mainstream ophthalmology. In FA photography, before capturing the images using fundus camera, a sterile aqueous solution, sodium fluorescein is injected intravenously [23]. Imaging photos from FA can show microaneurysms, increase in the foveal avascular zone, abnormal blood vessels, neovascularization etc. Figure 2.1 shows the example of FA image, the white small round objects are microaneurysms. The part of the retina most affected by diabetes is blood vessels and FA is currently the gold standard for evaluating them. Researchers working on automated microaneurysm detection using FA images achieved results similar to clinicians. Although injecting sodium fluorescein improves the contrast of the FA images but this improvement is accompanied by a number of potential side effects. These include transient nausea, vomiting and allergic reactions. About 2.9% of patients face the transient nausea and vomiting is observed in 1.2% of the patients [24]. In case of allergic reactions, the examples of mild reactions are pruritus and urticarial while in severe case, anaphylaxis has also been reported[25].

2.2.2 Fundus Photography

In color fundus photography, fundus camera is used to record color images of the fundus. Traditionally, film based fundus photography were performed. With the introduction of digital fundus camera, now digital color fundus photography has become widely chosen.

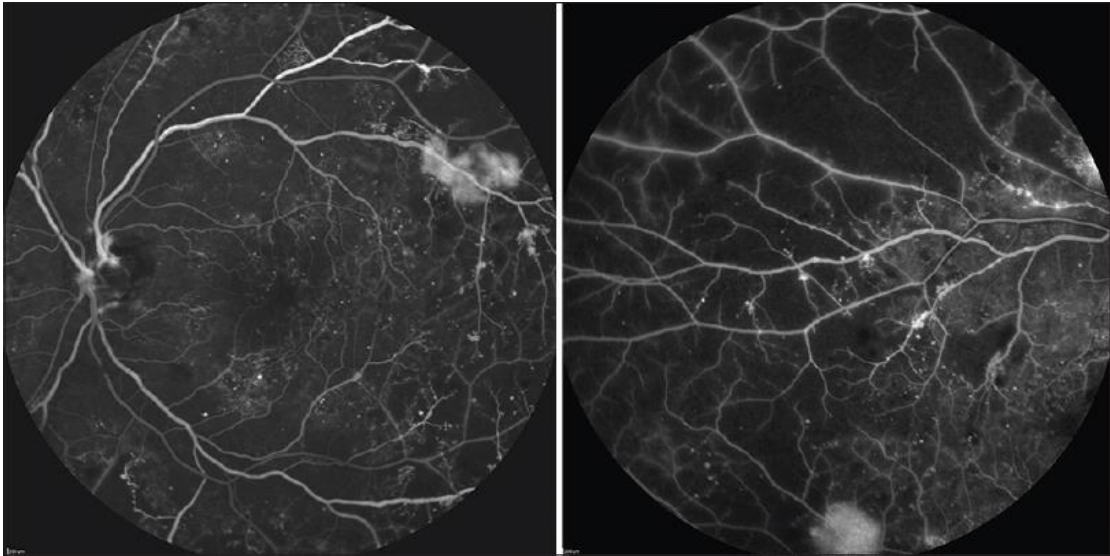


Figure 2.1: Fluorescein angiography shows scattered microaneurysms [26]

Types of fundus photography are standard, wide field, and stereoscopic. 30° of the posterior pole of the eye includes the optic nerve and the macula can be captured by standard macular fundus photography, as shown in the Figure 2.2. In wide field fundus photography, a montage image showing a 75° field of view can be created by combining seven fields using standard fundus camera, as shown in Figure 2.3. Newer cameras are capable of capturing fundus images up to 200° field of view. Thus more than 80% of the total surface area of the retina can be viewed [27]. Similar to direct ophthalmoscopy, stereoscopic fundus images allows for examination of the pathology in three dimensions. In stereoscopic imaging, two images are created by laterally shifting the fundus camera and when viewed appropriately, they become fused and thus form a singular stereoscopic picture [28].

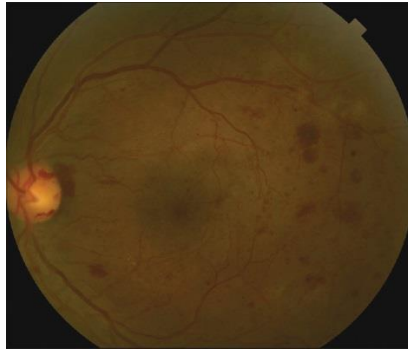


Figure 2.2: Standard color fundus image, 30° of the posterior pole



Figure 2.3: Based on 7-field color fundus photography, same patients montage image as in Figure 2.2

2.2.3 Ultrasonography

B-scan ultrasonography is another fundus imaging modality. It is useful in proliferative DR. In this case an eye image is created by using sound waves [29]. In patients with media opacity such as vitreous hemorrhage, the retina cannot be accessed directly through standard ophthalmic examination. In such cases B-scan ultrasonography is most useful. The presence of retinal detachment can be shown using B-scan ultrasonography. B-scan ultrasonography can also be used to show other retinal pathologies such as a posterior vitreous detachment or vitreous hemorrhage [30]. However for clear media, this imaging technique is not useful especially for diabetic retinopathy.

2.2.4 Optical Coherence Tomography

The technique that can evaluate retinal morphology with microscopic resolution is optical coherence tomography (OCT) [31]. The working principle of OCT is to emit light and measuring the time taken for light to be reflected back from the tissue. It is similar to ultrasonography where sound waves are used. For the management of various retinal diseases, especially in macular diseases, the OCT has now become the main stream. It is the most useful in measuring and quantifying macular edema. In managing patients with diabetic macular edema, it has developed into the most important imaging tool.

2.3 Preprocessing

Fundus images have non-uniform illumination and suffer from low and varying contrast. Therefore, they are generally preprocessed to overcome these variations in illumination and contrast. The retinal images contain noise as well as variation within and between the retinal images. To obtain meaningful information, this variation must be compensated. Intra retinal variation is due to the presence of abnormalities, differences in light diffusion, fundus thickness and variation in fundus reflectivity [32]. Variation in fundus reflectivity causes intensity shading, the shade however may be corrected usually by median filtering. While inter retinal images variation is due to factors such as differences in cameras, retinal pigmentation, illumination, and acquisition angle. Preprocessing can be mainly classified for the rectification of the following [32]:

1. Correction of non-uniform illumination.
2. Color normalization.
3. Contrast enhancement.

2.3.1 Correction of Non-uniform Illumination

Non-uniform illumination causes shading artifacts and vignetting [33], which hinders the quantitative image analysis. The subsequent reliable global operators are also badly affected due to non-uniform illumination. Other adverse effects are altering of local statistical characteristics i.e. mean, variance and median. Different techniques have been proposed to attenuate this deviation and refining the reliability of subsequent operators. Image formation models for describing the observed retinal images, typically in terms of foreground image, background image and an acquisition transformation function has been proposed by several authors e.g. [34, 35]. All illumination variation due to the transformation function or the original background can be contained in the background image while the objects in the foreground image are vasculature, visible lesions and optic disc. The non-uniform variations in the background image can be removed using a method called shade-correction. In this method, by smoothing the original image using a mean or median filter with a large kernel, a background image is approximated. Shade-corrected image is obtained by either the filtered image subtracted from the original image or original image divided by the filtered image [36-38], as shown in Figure 2.4. (a) original colored image, (b) green channel image, (c), background estimated image and (d) non-uniform corrected image. Alternating sequential filtering and brightness adjustment procedure are respectively proposed by [39, 40].

2.3.2 Color Normalization

Color is a powerful descriptor and can be used for discriminating between different retinal features. But there is a significant variability in the color of intra-image and inter-image. Also variability in pigmentation of skin and inter patient color of iris affect the coloration of the images. The age of patient also affects the color of the images. Therefore, it is necessary to normalize the color of retinal images. There are different approaches for color normalization. In the histogram equalization based approach, the histogram of each color channel in the original colored image is redistributed so that the histogram equalized image holds a uniform distribution of pixel values. The histogram of each channel is equalized by applying a monotonic, non-linear transformation function. Thus each grey level value of the input image is

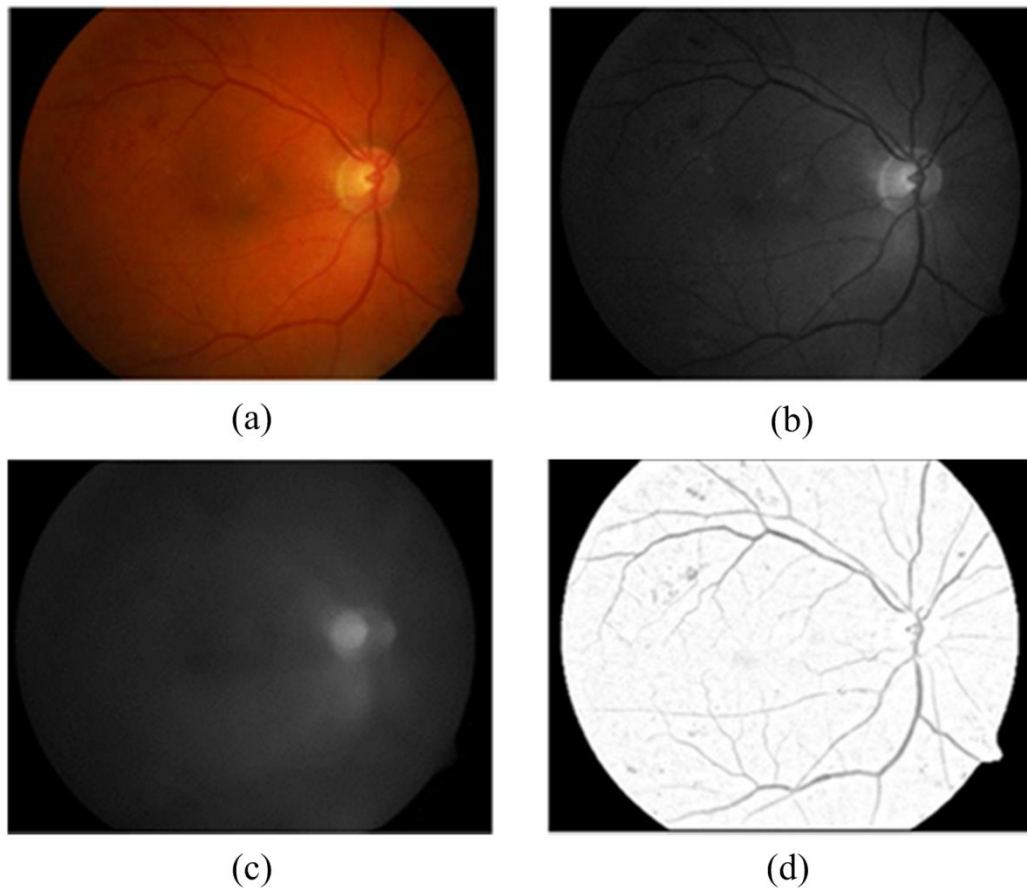


Figure 2.4: Non-uniform illumination correction, (a) original colored image, (b) green channel image, (c), background estimated image and (d) non-uniform illumination corrected image, obtained by dividing the original image by the filtered image.

mapped to a new corresponding value in the output image. Another approach is histogram specification, this involves interpolation of the distribution of each channel to closely match to a reference channel. The image with very good contrast and coloration is selected as reference as shown in Figure 2.5 (top row represents the colored images while shown in bottom are the color normalized images). Some of the prominent works based on histogram equalization/specification are [41-44]. Sinthanayothin et al. [45] transformed the original RGB image to an intensity-hue-saturation. This results in separating the different channels and normalization without any effect on perceived relative pixels color values.

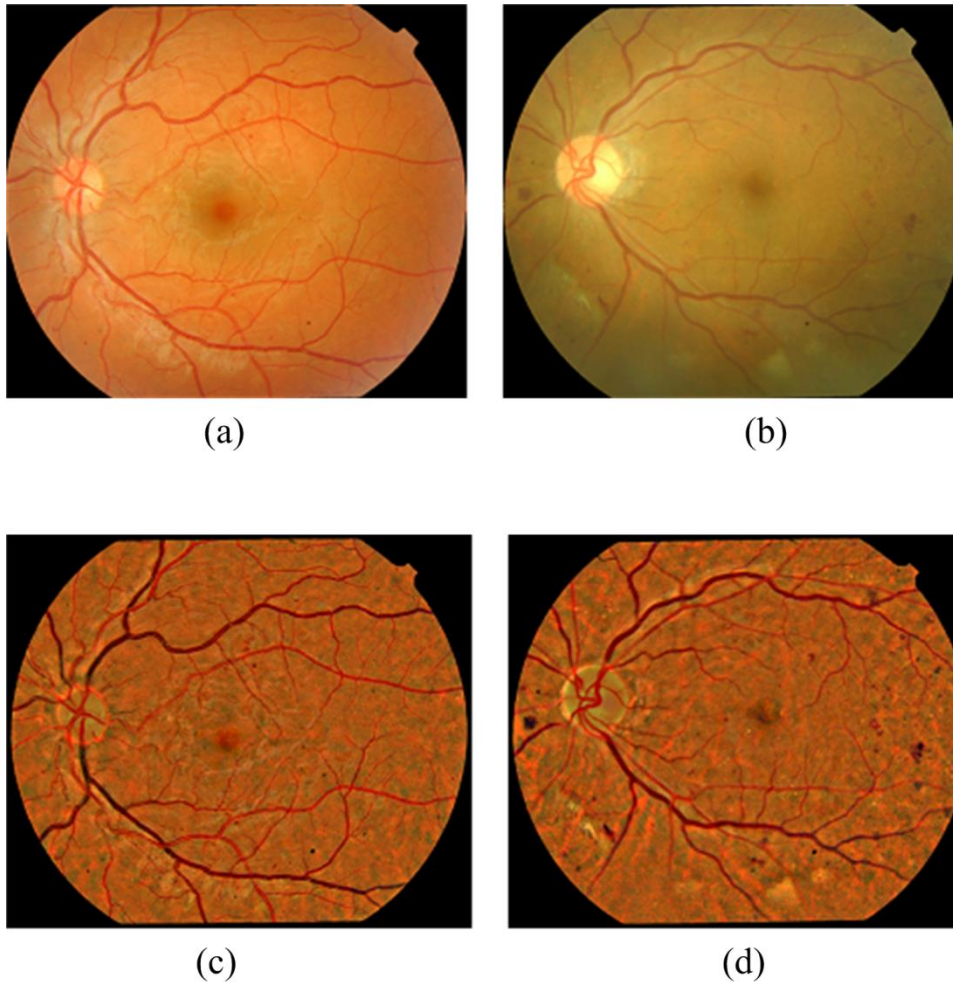


Figure 2.5: Color normalization, are two different coloration images, while (c) and (d) are the color normalized images of (a) and (b) respectively, reproduced from [46]

2.3.3 Contrast Enhancement

The contrast enhancement techniques aim to alter the visual appearance so that objects can be distinguished from the background and other objects. Many contrast enhancement algorithms have been proposed to more easily distinguishable retinal features. Usually after correcting non-uniform illumination and color normalization, contrast enhancement approaches are applied to the images. Shown in Figure 2.6 (a) original color image, (b) green channel, (c) background and (d) contrast enhanced image obtained after non-uniform illumination correction and histogram specification. The color fundus images acquired often contain photographic artifacts and exhibit low contrast. Typically the center of the image has a higher contrast while moving outw-

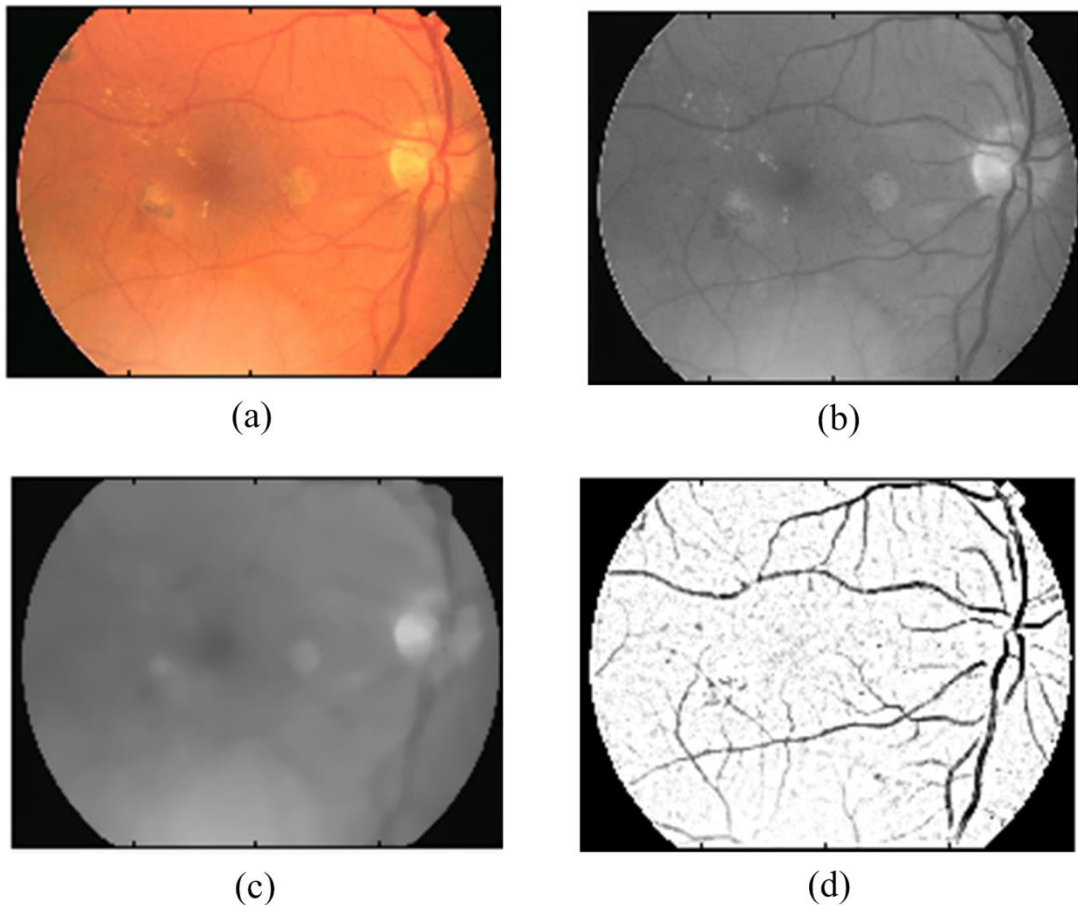


Figure 2.6: Contrast enhancement

-ard from the center reduced contrast is observed [43, 47]. Some of the approaches for contrast enhancement of retinal images are [45, 48-50].

2.4 Microaneurysm Detection

Figure 2.7 depicts the generalized block diagram of computer aided diagnosis (CAD) system for detecting MAs. The MA detection system can be classified into three main classes. Class I in which MA candidates are first detected, then using some features, the candidates are classified into true MA and false MA. Class II are all those MA detection systems that straight away using some features to detect MA at full fundus image level. Whereas in case of Class III, blood vessels are removed and candidate MA are detected and finally candidates are classified into true MA and false MA. The proposed system for MA detection belongs to this class of MA detection system. Microaneurysms (MAs), which are basically the saccular enlargement of the venous ends of retinal

capillaries, are said to be the first sign of DR. They are round in shape and have red color similar to blood vessel [9, 14, 51]. MAs appear and disappear during the early course of retinopathy. The MA count and turnover are important measures of DR progression [52, 53]. Therefore, accurately detecting MA is not only important for DR detection, but also it may assist in monitoring DR progression. They are one of the first lesions selected for automated image due to the fact that they have definite clinical implications and they are reasonably easy to describe. Hence people started working in early 1980s on automated MA detection. Following are some of the important approaches used for MA detection.

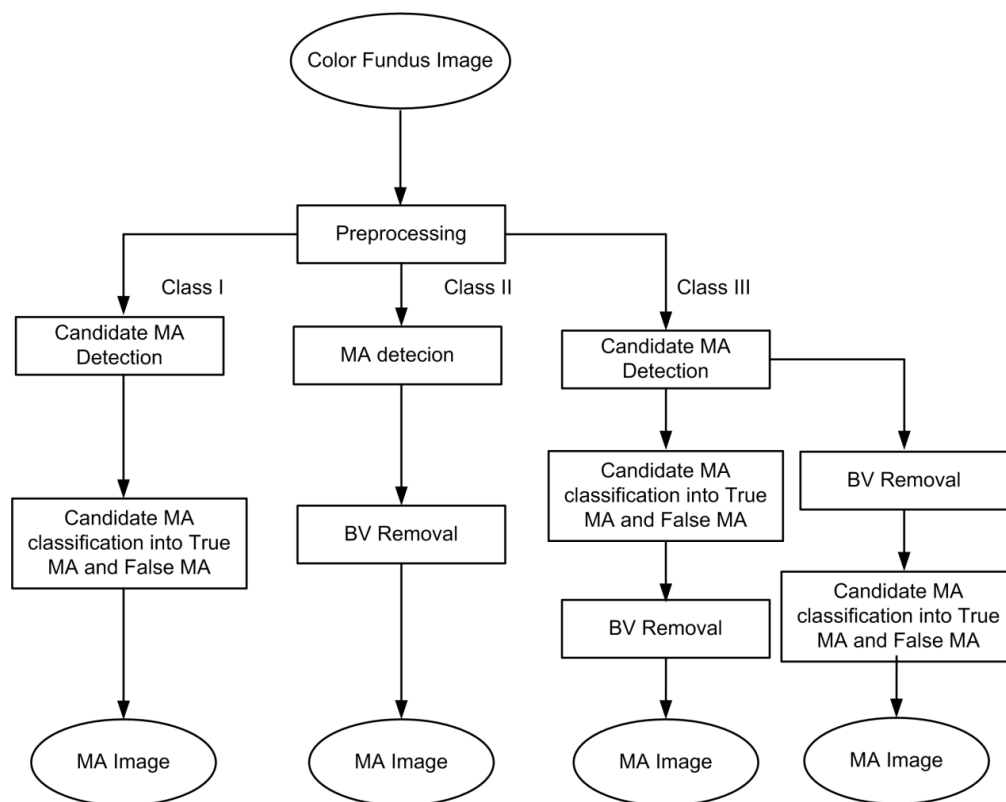


Figure 2.7: Generalized block diagram of CAD system for MA detection

2.4.1 Mathematical Morphology

Lay et al. [54] proposed MA detection approach based on morphology. The images were digitized film negatives and covered a small field of view of macula so MAs were well resolved. In these images MAs appeared dark because they used image negatives.

They applied top hat transform to identify local minima. For blood vessel identification top hat transform with a linear structuring element at various orientations was used too. The dataset used has 10 angiographic images containing 177 MAs. The resolution of the images was 256×256 pixels with 100 gray levels. The system had a sensitivity of 58% with 4.2 false positives per image. Baudoin et al. [55] improved the system of Lay et al. [47] by adding an extra morphological processing to remove false detection. There were 1045 MAs in 25 retinal angiographic images used. The system achieved a higher sensitivity of 70 % with slightly higher false positives of 4.4 per image and time taken by the process was 30-40 minutes. Shown in Figure 2.8 is an angiographic image with MAs which are white dots. Spencer et al. [36] proposed a strategy for MA detection in which initial segme-

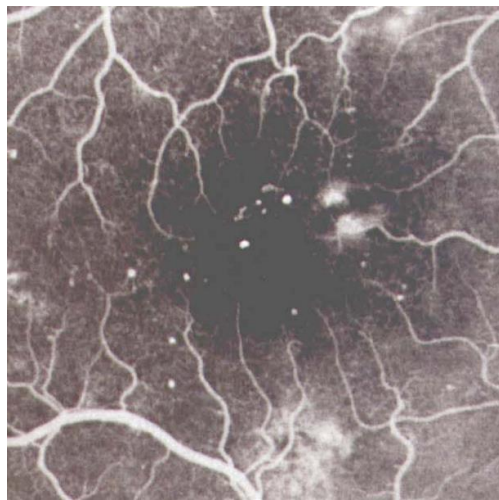


Figure 2.8: Angiography (positive image), MAs are the white dots

ntation was achieved after preprocessing images and then using bilinear top-hat transformation and matched filtering. Following this process, the images which contain candidate MAs were binarized. A novel region-growing algorithm was used and subsequently based on the size, shape, and energy characteristics, the candidates were classified. They claimed to have similar performance as the clinicians. Thus the system could be deployed to accurately monitor the progression of DR. Walter et al. [56] proposed MA detection based on bounding box closing. Bounding box closing is basically a diameter closing instead of a linear structuring element. After preprocessing the image, bounding box closing was used to detect the MA candidates. Based on image quality, automatic threshold was calculated. In the final step, using position, area and contrast, false positives were removed. The algorithm was tested with 5 images

containing 133 MAs and achieved a sensitivity of 86.4%. Some of the other approaches based on morphology are [57, 58].

2.4.2 Matched Filter

Spencer et al. [59] used Matched Filter (MF) to detect MAs and blood vessel. After preprocessing the images, they used MF to studying the intensity cross-sections of microaneurysms from various digitized fluorescein angiograms. They concluded that MAs could be approximated to a two-dimensional Gaussian. MF was used for both blood vessel detection and MA detection. Cree et al. [60] proposed automated MA detection system using MF. After preprocessing and blood vessel removal, MF was used to locate all possible microaneurysms in the image. The resultant image was thresholded in such a way to keep maximum number of MA candidates to retain the maximum sensitivity. Subsequently region growing was deployed and using 13 features, the candidate MA was classified into MA and false positive using rule based classifier. The dataset consisted of 20 test images containing 297 MAs. A sensitivity of 82% and a specificity of 84% was achieved which corresponded to a false-positive rate of 5.7 microaneurysms per image. Cree [61] designed an automated microaneurysm detector for color retinal images. After preprocessing the green channel, top hat transform by reconstruction in various orientations was used to remove the blood vessels. The small round objects detected in the blood vessels were removed from the image by using a 2D matched-filter. The matched image was thresholded to obtain the MA candidates. To properly delineate the candidates, region growing was used. Seven features were extracted from the region growing candidates and using a Naïve Bayes classifier, the candidates were classified into MAs and non-MAs. Other approaches based on MF are [36, 62].

2.4.3 Neural Networks

Gardner et al. [63] used a neural network (NN) to determine whether diabetic features in fundus images can be detected by neural networks. The network was compared against an ophthalmologist for screening a set of fundus images. The images were broken into small windows of size 20×20 and 30×30 for detecting blood vessels/exudates and hemorrhages respectively. Pixel data of the window and Sobel operator images were used as features and NN was trained and tested. In detecting diabetic retinopathy, the system achieved a sensitivity of 88.4% and a specificity of 83.5%. Similar approach was used by Kamel et al.[64] to detect microaneurysms. Usher et al. [47] used NN to classify each image into those with lesions and those without lesions.

2.4.4 Miscellaneous Approaches

Sanchez et al. [65] proposed MA detection system in which after preprocessing, background and foreground objects are separated using Mixture Model-based Clustering. In this way different image regions can be obtained which may correspond to lesions. The method is robust to changes in the appearance of color fundus images. Based on color, shape and texture characteristics, a likelihood of each region is generated using logistic regression. The probability map is then thresholded to obtain final MA classification. For evaluation of the algorithm, ROC dataset [66] is utilized. Zhang et al. [17] detected microaneurysms using multi-scale correlation coefficients. Algorithm is based on two levels, first level called coarse level in which MA candidates are extracted and the second level called the fine level in which MA candidates are classified into true MA and false positives. Based on similarity between the Gaussian function and grayscale distribution of MA, correlation coefficient was used to extract the initial MA candidate. In case of the MA, the coefficient would be high, and low otherwise. To match the different sizes of MAs, multiple scales of the Gaussian kernel were used. At fine level, 31 features were used for each candidate. These are based on shape, grayscale pixel intensity, color intensity, responses of Gaussian filter-banks, and correlation coefficient values. The algorithm was evaluated with ROC dataset.

Mizutani et al.[67] used double ring filter to detect MA. After image preprocessing, a double ring filter was used. This filter consisted of an inner circle and an outer ring with diameters of 5 and 13 pixels respectively to detect the candidate MA. The blood

vessels were segmented and those candidates which were from blood vessel were removed. Subsequently twelve image features were extracted and rule based and artificial neural network (ANN) classifier was employed to classify candidate lesions into microaneurysms or false positives. On ROC training dataset, a sensitivity of 50.6% and 44.9 % with 105.28 and 27.04 false positives per image was achieved using rule based and ANN classifier respectively. Adal et al.[14] modelled MAs by finding regions or blobs of interest. After preprocessing, candidates were detected using Hessian features. Due to variation in size MA and variation in the resolution of images, scale adaptive approach with an automatic local-scale selection technique was proposed. The features extracted are 18 scale-space, 64 Speeded up robust features (SURF), 3 Radon-space and 2 image features from each MA candidate. A semi-supervised based learning approach was used to classify each candidate into MA and false positive. Four classifier namely K-Nearest Neighbor (KNN), Naïve Bayes, Random Forest, and Support Vector Machines (SVM) were used. A performance evaluation was conducted to find optimum classifier-feature pairing. The best classifier-feature pair was Radon and SURF features coupled with SVM and KNN classifiers. On ROC training dataset, a sensitivity of 44.64% with 35.20 false positives per image were achieved.

Lazar et al. [16] used rotating cross-section profile analysis to detect MA. In the inverted green channel, MAs are local intensity maximum structures. MA candidates were selected based on local maximum region (LMR) after preprocessing the image and inverting the green channel. In each LMR, for a pixel with maximum intensity, a set of cross-sectional intensity was obtained. Furthermore on each profile, peaks were detected and attributes of peaks such as the height, size and shape were calculated. The feature set consists of orientation of the cross-section changes and statistical measures of these attribute values. A naïve Bayes classifier was used to classify the candidates. They tested their algorithm on two datasets i.e. ROC and their private dataset. Giancardo et al. [68] proposed a MA detection based on Radon transformation and rule based classification, while Giancardo et al. [69] extracted features from Radon-transform and used support vector machine. Abdulazeem [18] proposed the MA detection system based on circular Hough transform. In this approach blood vessel were first removed. Then based on the fact that microaneurysms are circular, circular Hough transform was applied on all the remaining objects in the image. The algorithm was

tested on angiographic images. An improvement in terms of sensitivity and specificity was observed. Their technique was implemented by [70] for color images. A sensitivity of 28% with 505.85 false positive per image was achieved. Quellec et al. [71] proposed a method to detect MAs using template matching in wavelet domain. A wide range of shapes can be modeled by the generalized Gaussian function for instance MAs may be modeled with 2D rotation-symmetric generalized Gaussian function template. One hundred reference lesions were randomly selected, to study shape deviation of the lesions. The dataset used consists of green-filtered color (GFC) photographs, angiographs and color photographs. Sensitivity of 90%, 94% and 90 % and positive predictive values of 90%, 92% and 89% were achieved respectively on GFC, angiographs and color photographs. Sopharak et al. [58] proposed a scheme for detecting MAs consists of three main steps. In the first step images are preprocessed and exudates and blood vessel which may cause a false detection are detected in the second step. And in the third step, MAs were detected by using a set of optimally adjusted mathematical morphology. The scheme was evaluated on 45 non-dilated retinal images. Sensitivity of 81.61%, specificity of 99.99%, precision of 63.76% and accuracy of 99.98% were achieved.

Akram et al. [72] proposed a three-stage system for identification and classification of MA. Images were preprocessed in two parallel steps. They enacted the contrast for dark lesions detection and enhanced the vessel for blood vessel segmentation. Blood vessels were removed from the dark lesion enhanced image using threshold to obtain the candidate MAs. In the second stage, the shape based, gray level based, color based and statistical features of the candidates were extracted. While in the third stage, a hybrid classifier was used. To improve the accuracy, the ensemble approach was utilized. GMM, SVM and multimodal medoid were combined. The publically available dataset DIARETDB0 [73] and DIARETDB1 [74] were used to evaluate the algorithm. Sensitivity of 98.64%, specificity of 99.69% and accuracy of 99.40% were achieved.

Antal et al. [70] proposed an ensemble based approach for improving the MA detection. In their proposed scheme, preprocessing methods and candidate extractors were combined. The preprocessing methods include Walter–Klein Contrast Enhancement [10], contrast limited adaptive histogram equalization (CLAHE) [75], vessel removal and extrapolation [76], illumination equalization [77]. While the

candidate extractor were Walter et al.[10], Spencer et al.[36], Circular Hough-Transformation[18], Zhang et al.[17] and Lazar et al.[78]. Using optimal voting scheme, preprocessing-candidate extractor were selected and using threshold, final decision on the presence of MA was made. The datasets used was Retinopathy Online Challenge (ROC), DiaretDB1 2.1 Database [74] and private database provided by Moorfields Eye Hospital. They obtained the best score on ROC dataset among all the participant of that time. Ram et al.[79] proposed MA detection system using successive clutter-rejection-based. Detection of microaneurysm as target detection from clutter was formulated. To progressively lower the number of clutter responses, a successive rejection-based scheme was proposed. Based on a set of specialized features, processing stages were designed to pass majority of true MAs and reject specific classes of clutter. After the final rejecter, true positives that remain are assigned a score based on their similarity to a true MA. Wang et al. [80] proposed singular spectrum analysis (SSA) based MA detection. Using dark object filtering process, the candidate objects were located. After performing SSA based candidate cross-section profile analysis, 11 features from the scaled profile were extracted. For candidate classification, kNN, support vector machines (SVMs) and naive Bayes (NB) classifiers were compared and the best results obtained was using the kNN. The algorithm was evaluated on ROC dataset. Some of the other approaches are [58, 81-83].

2.5 Summary of the Literature Review of Microaneurysm Detection

The summary of the literature review of the most relevant MA detection approaches is presented in Table 2.1. The fundus images used for automated microaneurysm detection are either angiographic or color retinal images. The performance of those MA detectors based on angiographic images is better.

Table 2.1: Summary of the most relevant approaches for MA detection

First Author	Year	Method	Dataset used	Results and comments
Spencer [36]	1996	Top-hat transformation & matched filtering, thresholding, region growing,	13 angiographic images	Results achieved are similar to the clinicians. The method achieved very good re-

		classification using size, shape and energy		sults because MA are well contrasted in angiographic images.
Cree [61]	2008	Bood vessel removal and matched-filtering to detect small round objects. Region growing and using seven features and Naïve Bayes classifier for candidate classification	758 color retinal images of 1560×1360 pixel size at 50° FOV.	The achieved sensitivity is 85% with 90% specificity. This is in the context of a diabetic retinopathy screening programme. Thus the detector is made more specific and less sensitive.
Gardener [63]	1996	The images are divided into small windows of size 20×20 and 30×30 for detecting blood vessel/exudates and hemorrhages respectively. Pixel data of the window and Sobel operator images are used as features and NN was trained and tested.	147 images containing DR and 32 normal images are used.	System achieved the sensitivity of 88.4% and a specificity of 83.5% for the detection of diabetic retinopathy.
Quellec [84]	2008	Template matching in wavelet is used and MA is modeled based on 2D rotation-symmetric generalized Gaussian function template. They used 100 reference lesions, to study their shape deviation.	914 color images	The achieved sensitivity is 89.62%
Lazar [16]	2013	MA candidates based on local maximum region (LMR) and obtained a set of cross-sectional intensity. Candidates are classified	50 color images of ROC dataset	Sensitivity of 48% with 73.944 FPPI is achieved.

		using different attributes and naïve Bayes classifier.		
Adal [14]	2014	Hessian features based candidate extraction and using, scale space, SURF Radon-space and image features and four classifier, found optimum classifier feature pair	50 color images of ROC dataset	44.64% sensitivity with 35.20 FPPI is achieved.

That is owing to the contrast enhancement agent injected intravenously. On the other hand, the performance of the microaneurysms detectors using color fundus images is limited due to low and varying contrast. The challenge is to find a balance between sensitivity and specificity. Simply increasing sensitivity may result in an increase in false positives. Based on microaneurysm literature review, most of the false positives come from blood vessels, background and other objects/lesions. To improve the sensitivity while keeping the similar number of false positives per image we need to address the issue of various types of false positives. The existing literature review do not address the issue of false positives by type. We, however, believe that addressing the issue of false positives by type is a more effective way. Secondly the multiscale techniques which are good at representing geometric properties of structures such as Curvelet Transform can be good in detecting MA.

2.6 Blood Vessel Segmentation

The block diagram of generalized automated blood vessel segmentation system is shown in Figure 2.9. Similar to MA, blood vessel segmentations can also be roughly classified into three main classes. In Class I, firstly BV candidates are detected followed by candidates classification into BV and non BV; in case of Class II BV detection system, all the pixels in the image are classified into BV and non BV pixels; whereas in case of Class III BV detection system, there is a post processing after all the pixels in the image are classified into BV and non BV pixels. The proposed algorithm of BV segmentation belongs to the class III BV segmentation system. Blood vessel detection and analysis are being used in diagnosing different diseases. Moreover accurate blood

vessels segmentation may improve the performance of automated DR detection system such as MA [85].

2.6.1 Filter based Blood Vessel Detection

Chaudhuri et al. [86] firstly proposed the idea of matched filter to detect the piecewise linear segments of blood vessels. The following three properties of the blood vessel are observed.

1. Due to the fact that BV typically have small curvatures, the anti-parallel pairs are assumed to be piecewise linear sections.
2. In comparison with other retinal surfaces, blood vessels have lower reflectance, thus relative to the background, they appear darker. Based on observation that ideal step edges in blood vessel are rare, therefore, Gaussian curves may approximate the intensity profiles of the blood vessels.
3. There is a gradual change in the vessel caliber when it travels radially outward from the optic disc.

It may be realized that blood vessel may be oriented at any orientation and there will be a peak response of matched filter only if it is aligned with that particular orientation. Therefore, extending the idea of matched filter to 2D images requires a filter to be rotated at all possible angles. In addition, comparison of corresponding responses must be done and maximum response for each pixel can then be obtained. To find the blood vessel segments in all possible directions, 12 different templates are required. The limitation is the method being sensitive to edges. For instance, the method may detect some response due to edges of other bright objects (such as lesions, optic disc etc.) which do not resemble any vessel segment. This is due to the fact that the local contrast is very high and the edges of the objects partially match the shape of the kernel. A post- processing step is needed to identify and subsequently eliminate such false detection. Hoover et al.[87] improved the matched filter system of Chaudhuri et al. [86] by adding probing technique. Using a novel probing technique, the Matched Filter Response image was thresholded. The probe examined the image based on a number of properties. The constituent pixels were simultaneously segmented and

classified when the probe decided a pixel belonged to a vessel. Contrary to classifier-based methods, this method allowed, before final classification, a pixel to be tested in multiple region configurations. Similarly in comparison with tracking based methods, the probing method was driven by a two-dimensional (2-D) MFR. Using local and regional properties, each pixel is classified into vessel and non-vessel. 15 times reduction in false positives comparing to basic MFR with 0.75 true positive rate was achieved. An improved matched filter was proposed by Al-Rawi et al. [88] for blood vessel detection. Better filter parameters (size, standard deviation and threshold) were proposed to increase the response of the matched filter for the detection of blood vessels. Twenty training images from DRIVE dataset were used and exhaustive search optimization procedure was adopted to find the best parameters of matched filter. Matched filter being a simple and effective method for blood vessel segmentation is prone to false detection because it is sensitive to edges. It detects vessel as well as non-vessel edges. The first-order derivative of Gaussian (FDOG) was incorporated by Zhang et al. [89] along with MF to remove false detections. The system is called MF-FDOG. Blood vessels were

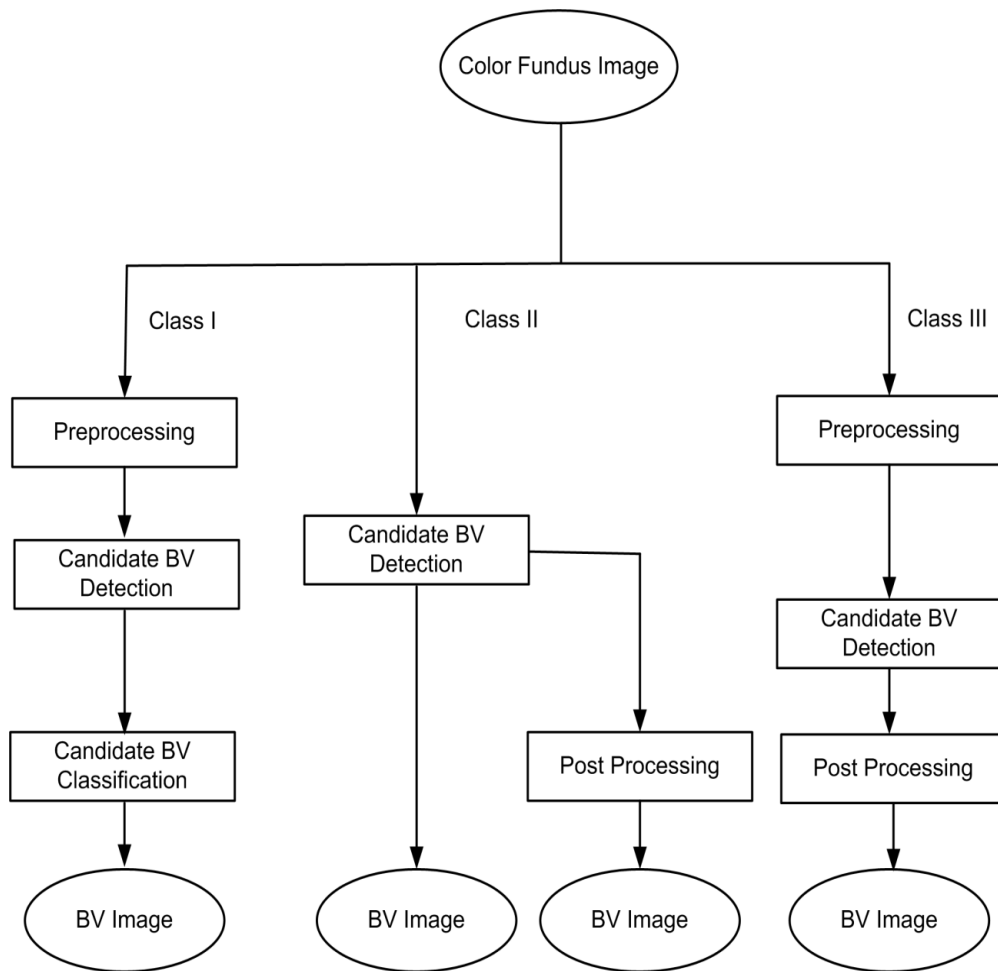


Figure 2.9: Generalized block diagram of automated blood vessel segmentation

obtained by thresholding the response of the MF, whereas the FDOG was employed to adjust the threshold. The MF-FDOG method is not only very simple but also very effective in improving the overall accuracy i.e. significant reduction in false positives while detecting fine vessels missed by original MF. Cinsdikici et al. [90] introduced the hybrid of MF with ant colony to overcome the deficiency of MF. The blood vessel was detected in two parallel steps i.e. using ant colony algorithm and MF filter. The detected vessel in both steps were combined to get the full set of vessels. In post

processing step length filtering was used. The method could not get rid from the pathological areas detected as blood vessels. To improve the performance of the MF, Gang et al. [91] used amplitude-modified second order Gaussian filter. Width

measurement in the detection process was added. Thus there was a significant increase in the success rate of detection. It is shown that when the magnitude coefficient of the Gaussian filter is suitably assigned, the vessel width can be measured in a linear relationship with the spreading factor of the Gaussian filter. Second-order Gaussian filter for retinal vessel detection based on this elaboration was proposed. Using the vessel width measurement the size of the blood vessels could be found. Also it can be used in optimization of MF.

2.6.2 Multiscale Based Blood Vessel Detection

The approaches using multiple scales to segment the blood vessel are based on the fact that blood vessels have varying width. Hence they can be better segmented using multiple scales. These methods can be further classified into wavelet based, Curvelet based and Gaussian based.

Miri et al. [92] used Curvelet Transform (CT) to enhance the edges of retinal images for segmenting the blood vessels. Edges of the colored retinal images were enhanced by modifying the coefficients of the CT. The ridges were found by applying morphological operators using multistructure elements on the enhanced image. The scheme was tested with DRIVE dataset, achieving more than 0.94 accuracy for blood vessel detection. Esmaeili et al. [93] enhanced the image using CT and intensified blood vessels using matched filter while CT was again utilized to segment vessel from background. Soares et al. [94] proposed a vessel segmentation method based on 2-D Gabor wavelet. Using Gaussian Mixture Model (GMM), each pixel is classified into vessel and non-vessel. Gabor wavelet has the capability to be tuned to specific frequencies, which may be exploited for vessels contrast enhancement and noise removal in a single step. Pixel intensity in the green band and two-dimensional Gabor wavelet transform responses taken at multiple scales (they used five scales) were used as features. All the features were normalized to have zero mean and unit standard deviation. The approach was tested with two publicly available datasets DRIVE and STARE. On the DRIVE database, they achieved an average accuracy of 0.9466 with area under the receiver operating characteristic curve of 0.9614. Based upon scale space analysis of the first and second derivative of the intensity image, Martinez-Perez et al. [95] proposed a blood vessel segmentation method. The region was grown in two

stages using local maxima over scales of the magnitude of gradient and maximum curvature. In stage I, the growth was restricted to regions of low gradient magnitude along with the 8-neighboring pixels spatial information. In the stage II, to allow borders between regions to be defined, this constraint was relaxed. The algorithm was tested on both fluorescent retinal images and red free images. Martinez-Perez et al. [96] modified the Martinez-Perez et al. [95] by adding a diameter-dependent equalization factor to the multiscale information and tested the system on DRIVE and STARE datasets. On STARE dataset the average TPR of 0.7506, average FPR of 0.0431 and average accuracy of 0.9410 were achieved. While on DRIVE dataset, average TPR of 0.7246, average FPR of 0.0345, with average accuracy of 0.9344 were achieved. Fast retinal vessel detection and measurement based on wavelets and edge location refinement was proposed by [97]. On DRIVE dataset the method achieved accuracy of 0.9371 with 0.7027 sensitivity. Some of the other methods using wavelet are [98, 99].

2.6.3 Mathematical Morphology based Blood Vessel Detection

Zana et al. [100] presented an algorithm to segment blood vessel using Mathematical Morphology (MM). A vessel was assumed to be a bright pattern, piece-wise connected, and locally linear. Based on this description of vessel, MM was the ultimate choice. But many other patterns fit to such a description. So a cross curvature evaluation to differentiate vessels from analogous background patterns was also used. They were separated out as they had a specific Gaussian-like profile whose curvature varies smoothly along the vessel. The algorithm consists of the following steps:

1. Noise reduction
2. Improvement of linear pattern with Gaussian-like profile
3. Cross-curvature evaluation
4. Linear filtering

Inverted green channel without any preprocessing was used. The dataset used consists of 33 images of poor quality. Out of the 33 images 31 images contained pathologies. The images were obtained by scanning the transparent negatives developed on paper.

The algorithm was able to detect most of vasculature tree in 14 images including two images from eye without any pathology. In the remaining 19 images few vessels were detected. In those images where most of the vessels could not be detected were due to the low contrast. The length of the structuring element determines the performance of the algorithm. Algorithm was also tested on other images that contains tree like structures e.g. road. Mendonca et al. [101] segmented the vessel by combining the detection of enter lines and morphological reconstruction. The three main processing phases of their algorithm were:

1. Preprocessing: To normalize the background and enhance the thin vessels.
2. Vessel centerline detection: To define a connected segments set in the central part of the vessels.
3. Vessel segmentation: To ultimately label those pixels which belong to blood vessel.

In the Preprocessing phase, background normalization was achieved by subtracting an estimate of the background obtained by filtering with a large arithmetic mean kernel. Using set of line detection filters at four orientations (0° , 45° , 90° and 135°), the thin vessel were enhanced by keeping the highest filter response for each pixel. The candidates for blood vessel centerline were chosen based on directional information supplied by four directional Difference of Offset Gaussians filters. Candidate points were connected by a region growing process guided by some image statistics while characteristics of the line segments were used to validate the detection of centerline segment candidates. To enhance the vessels of different widths, modified top-hat transform with variable size structuring elements was applied. Binary morphological reconstruction was used at four scales to obtain binary maps of the vessels and finally vessels were filled by region growing. Green component of the original RGB image, the gray band, the luminance channel of the National Television Systems Committee (NTSC) color space and the a^* component of L^*a^*b representation were used. Algorithm was tested with STARE and DRIVE datasets. The maximum accuracy on DRIVE dataset using gray band was 0.9463 while on STARE dataset they achieved 0.9479 using a^* component. Vlachos et al. [102] utilized morphological directional filtering and morphological reconstruction in the post processing step. Retinal vessel

segmentation technique based on line-tracking was used. Candidates were selected using multi-scale line tracking procedure. Then median filtering was applied to restore disconnected vessel lines and eliminate noisy lines. In the post-processing steps, morphological directional filtering was utilized to keep only vessel like structures whereas to remove erroneous regions such as blob morphological reconstruction was used. The approach was evaluated using DRIVE dataset. The achieved results were accuracy 0.9285 with 0.7468 sensitivity. [92, 98, 99, 103-106] are some of the other approaches utilizing mathematical morphology.

2.6.4 Hierarchical based Blood Vessel Detection

Xu et al. [107] used both Wavelet and Curvelet Transform based on hierarchical approach. Using adaptive local thresholding, a binary image was obtained from which large vessels were segmented. While for thin vessels, residual fragments in the binary image were used to classify them into vessels and none vessels. Twelve dimensional feature vector was constructed using Curvelet and wavelet coefficients which were then fed to a SVM. Finally to form the whole vascular network, tracking growth was used on thin vessel segments. DRIVE database was used to test the algorithm. The algorithm achieved average sensitivity of 0.7760 with average accuracy 0.93. Wang et al. [108] introduced a hierarchical blood vessel segmentation based on ensemble learning. Combination of two superior classifiers: Convolutional Neural Network (CNN) and Random Forest (RF) was utilized. CNN was used as a trainable hierarchical feature extractor whereas the ensemble RFs work as a trainable classifier. The algorithm was evaluated using two publicly available datasets (DRIVE and STARE). The method outperformed the state of the art methods by achieving accuracy of 0.9767 with 0.8173 sensitivity on DRIVE dataset while on STARE dataset, it achieved accuracy of 0.9813 with 0.8103 sensitivity. Roychowdhury et al. [105] proposed blood vessel to be segmented in two stages. Firstly major vessels were detected and then the fine vessel were detected. Green channel was preprocessed to enhance the contrast of blood vessel. High pass filtered image was obtained from the enhanced image which was then thresholded to get a binary image. Another binary image was obtained from the morphologically reconstructed enhanced image for the vessel regions. The major vessels were the common regions in the aforementioned two images. Using Gaussian

mixture model (GMM) all the remaining pixels in the two binary images were classified into vessel and non-vessel pixels. The feature set consisted of the neighborhood features and first and second-order gradient features, in all eight features. In the post processing step, the major portions of the blood vessels were combined with the classified vessel pixels. The algorithm was tested on STARE, DRIVE, and CHASE_DB1 datasets achieving accuracy of 0.953, 0.952, 0.9515 in an average of 11.7, 3.1, and 6.7, seconds respectively.

2.6.5 Active Contours and Model based Blood Vessel Detection

Based on hybrid region information of the image, Zhao et al. [109] proposed an infinite active contour model. It was presumed that in comparison with the length of a feature's boundaries based approach, small oscillatory structures could be detected using Lebesgue measure of the ϵ -neighborhood of boundaries. As local phase based enhancement map was a capable in preserving vessel edges whereas image intensity information guarantees a correct feature's segmentation. Therefore, to achieve superior general segmentation performance, model used region information i.e. combination of intensity information and local phase based enhancement map. The model was tested using three publicly available datasets DRIVE, STARE and VAMPIRE. For DRIVE dataset, it achieved sensitivity (0.742), specificity (0.982) and accuracy (0.954). A model based method for blood vessel detection was proposed by Vermeer et al. [104]. This approach was based on a Laplacian filter and thresholding segmentation step. This was followed by a classification to improve performance. The last step assured incorporation of the inner part of large vessels with specular refraction. This approach achieved a sensitivity of 0.92 with a specificity of 0.91. Lam and Hong [110] proposed a novel vessel segmentation algorithm based on the divergence of vector fields for pathological retinal images. Using the normalized gradient vector field, the centerlines were detected. Subsequently, based on the gradient vector field of a pixel, the candidate blood vessels were detected. The spurious detected candidate blood vessel were pruned using the distance from detected centerlines. The method achieved average accuracy of 0.9474 and area under the ROC curve (AUC) of 0.9392 on pathological images in the STARE database. Gonzalez et al. [111] proposed blood vessels detection technique based on graph cut. On DRIVE and STARE datasets, they

achieved accuracy of 0.9412 and 0.9481 with sensitivity of 0.7512 and 0.7887 respectively. Graph cut with Retinex and local phase based scheme for retinal vessel segmentation was proposed by Zhao et al. [109]. In this technique, image inhomogeneity was corrected by using Retinex. Images were enhanced using local phase while for the segmentation of the vessel graph cut based active contour was utilized. Using DRIVE dataset the approach achieved average sensitivity of 0.744 and average accuracy of 0.953.

2.6.6 Miscellaneous Approaches for Blood Vessel Detection

Orlando et al. [112] proposed an algorithm for retinal blood vessels segmentation based on fully connected conditional random field model. Support vector machine was used for classification. The approach was evaluated using DRIVE dataset and achieved sensitivity of 0.785 with 0.967 specificity. Azzopardi et al. [113] proposed trainable COSFIRE filters that selectively responded to vessels, and called it B-COSFIRE (Combination Of Shifted Filter Responses) with B (standing for bar). By computing the weighted geometric mean of the output of a pool of Difference-of-Gaussians filters, the orientation selectivity was achieved. While for achieving rotation invariance, shifting operations were used. B-COSFIRE filter was versatile because in an automatic process, its selectivity could be tuned. It was configured as symmetric filter for selecting the bars and asymmetric filters for selecting bar-endings. By adding the responses of the two rotation-invariant B-COSFIRE filters and thresholding, the vessel were segmented. The algorithm evaluation was done on three publically available datasets. The algorithm achieved sensitivity of 0.7655, 0.7716, 0.7585 and specificity of 0.9704, 0.9701, 0.9587 respectively on DRIVE, STARE and CHASE_DB1. An unsupervised method for blood vessel segmentation was proposed by Oliveira et al. [114]. Images were enhanced by combining matched filter, Frangi's filter and Gabor Wavelet filter. Two approaches for filter combinations investigated were weighted mean and median ranking. In case of weight mean based enhancement, deformable models were used i.e. the minimization of Oriented Region-Scalable Fitting energy (ORSF) and fuzzy C-means (FCM) for vessel segmentation. While in case of median ranking based enhancement they used simple threshold criteria. The performance of the algorithm was assessed on DRIVE and STARE datasets. Based on Median ranking it achieved

accuracy of 0.9464, 0.9532 with sensitivity of 0.8644, 0.8254 on DRIVE and STARE dataset respectively. Based on Weighted mean using ORSF, it achieved accuracy of 0.9356, 0.9429 with sensitivity of 0.7988, 0.8377 on DRIVE and STARE dataset respectively. While in case of weighted mean using FCM, the accuracy of 0.9402, 0.9446 with sensitivity of 0.9106, 0.8049 on DRIVE and STARE dataset were achieved respectively.

2.7 Summary of the Literature Review of Blood Vessel Segmentation

Summary of the literature review of the most relevant approaches for Blood Vessel segmentation is presented in Table 2.2. The algorithms using the angiographic images achieved a good performance for BV segmentation similar to the case of MA detection. But as far as the color fundus images are concerned, they suffer from low and varying contrast. The approach using color images that achieved the best accuracy is based on convolutional neural network [108]. Most of the approaches use the features which rely on edge detection and suffers from the false positives due to boundary of ROI and edges on the optic disc regions. Although the algorithms for blood vessel segmentation generally achieve a very low false positive rate but their sensitivity is relatively low if we set false positive rate (FPR) of ≤ 0.03 . Low sensitiv-

Table 2.2: Summary of the most relevant approaches for BV segmentation

First Author & Year	Algorithm	Evaluation Metrics (Sn, Sp, Acc)		
		Sn	Sp	Acc
Hoover [87], 2000	Matched Filter with thresholding Dataset: Angiographic images	0.7500	x	x
Soares [94], 2006	Pixel intensity in the green band and two-dimensional Gabor wavelet transform and GMM classifier. Dataset: DRIVE (colored images)	0.7283	x	0.9466

Vlachos [102], 2010	Multi-scale line tracking, median filtering and mathematical morphology. Dataset: DRIVE (colored images)	0.7468	x	0.9285
Wang [108], 2015	Combination of Convolutional Neural Network (CNN) and Random Forest (RF). Dataset: DRIVE (colored images)	0.8173	x	0.9767
Zhao [115], 2015	Infinite active contour model that uses hybrid region information of the image to approach this problem Dataset:DRIVE. (colored images)	0.7420	0.9820	0.954
Azzopardi [113], 2015	B-COSFIRE (Combination Of Shifted Filter Responses) with B standing for bar .Capable of achieving orientation selectivity and rotation invariance Dataset: DRIVE (colored images)	0.7655	0.9704	x

Note: x denotes the unknown values while Sn, Sp and ACC represent sensitivity, specificity and accuracy respectively.

-ity in blood vessel detection in this case, contributes to many false positives in automated MA detection algorithms in which blood vessels needs to be removed. Thus it is very important for a blood vessel segmentation algorithm to have a good sensitivity while keeping the false positive rate low. In order to have a good sensitivity, preprocessing should overcome the problem of non-uniform illumination, low and varying contrast. Therefore, there is a need to introduce additional steps in preprocessing the images to overcome these issues, and use some multiscale techniques such as Hessian to cope with various widths of the blood vessel in retinal images.

2.8 Summary

In this chapter different imaging techniques used for fundus photography have been presented. In addition different techniques used for preprocessing, microaneurysm detection and blood vessel segmentation have also been presented. Preprocessing is very important for any computer aided diagnosis (CAD) system. It corrects the non-uniform illumination, normalizes the color variation and helps to improve the contrast of the retinal images. The overall effect of the preprocessing shows an improvement in the performance of the CAD system. Most of the early works whether on MA detection or blood vessel segmentation used angiographic images. These algorithms achieved results similar to clinician's assessment. Although the contrast enhancement agent injection improved the contrast but it is also accompanied by many adverse effects. Thus this research moved away from angiographic images to digital color fundus photography. In general digital color fundus photography, MA, blood vessel and other pathologies are not well contrasted. Therefore, the performance of automated detection systems based on color retinal images is limited and this is still an open problem. In chapter 3, methodology of the proposed system for automated MA detection is described.

CHAPTER 3

METHODOLOGY OF AUTOMATED MICROANEURYSM DETECTION

3.1 Overview

Majority of the people suffering from diabetes mellitus will eventually develop diabetic retinopathy (DR). DR is one of the leading causes of blindness and can be controlled if

detected early. This chapter describes the methodology of microaneurysm detection system. In section 3.2.1, materials used for training and testing the proposed MA detection system is presented. Section 3.2.2 presents in detail the proposed automated MA detection system. The evaluation metrics for MA detection are presented in section 3.2.3. The chapter concludes with a summary presented in section 3.3.

3.2 Materials and Method for Microaneurysm Detection

3.2.1 Materials for MA detection

Publically available Retinopathy Online Challenge (ROC) dataset [66] will be used to evaluate the proposed system . The dataset consists of 50 images with ground truth at different resolutions mimicking the real world scenario. The MAs were annotated by four eye specialists at the Department of Ophthalmology, University of Iowa. The ROC dataset is challenging due to the presence of noise, compression artifacts and the general image quality. These are in common to the image quality found in mass screening projects. The images were acquired using different types of camera and at different resolutions, which makes it more difficult to detect MAs in such images. The fundus cameras used were Topcon NW 100, a Topcon NW200 and a Canon CR5-45NM. Niemeijer selected them from 150,000 photographs collected in a DR screening program to form the ROC dataset. Table 3.1 describes the different image types.

Table 3.1: Types of images used in the proposed approach

Type	Resolution(height x width in pixels)	Coverage of the retina	Number of images
Type I	768 x 576	45°	22
Type II	1058 x 1061	45°	03
Type III	1389 x 1383	45°	25

3.2.2 Method for Microaneurysm Detection

This section presents our proposed method for automated MA detection system Figure 3.1 depicts the complete procedure of the proposed MA detection system which consists of the following steps:

1. Candidate selection
2. Candidate features extraction
3. Candidate classification into true MA and false MA

As shown in the Figure 3.1(b), blood vessels are segmented from green band using Soares et al. method [94] and are extracted from preprocessed image to obtain image shown in Figure 3.1 (d). The image shown in Figure 3.1(d) is thresholded to obtain preliminary MA candidates. Similarly using gray band, image is segmented into foreground and background as shown in Figure 3.1 (f). Figure 3.1 (g) depicts the image obtained after separating the preliminary MA candidate image and background foreground image. Thus all those MA candidates which are from background are removed in this step. The objects in the image, shown in Figure 3.1 (g) are passed to the classifier to classify these objects into true MA and false MA. The classifier used in the proposed system is rule-based and consisted of three sequential stages. In stage one, false MA candidates are removed based on color features while in stage two, false candidates appeared as elongated objects are removed using Hessian features.

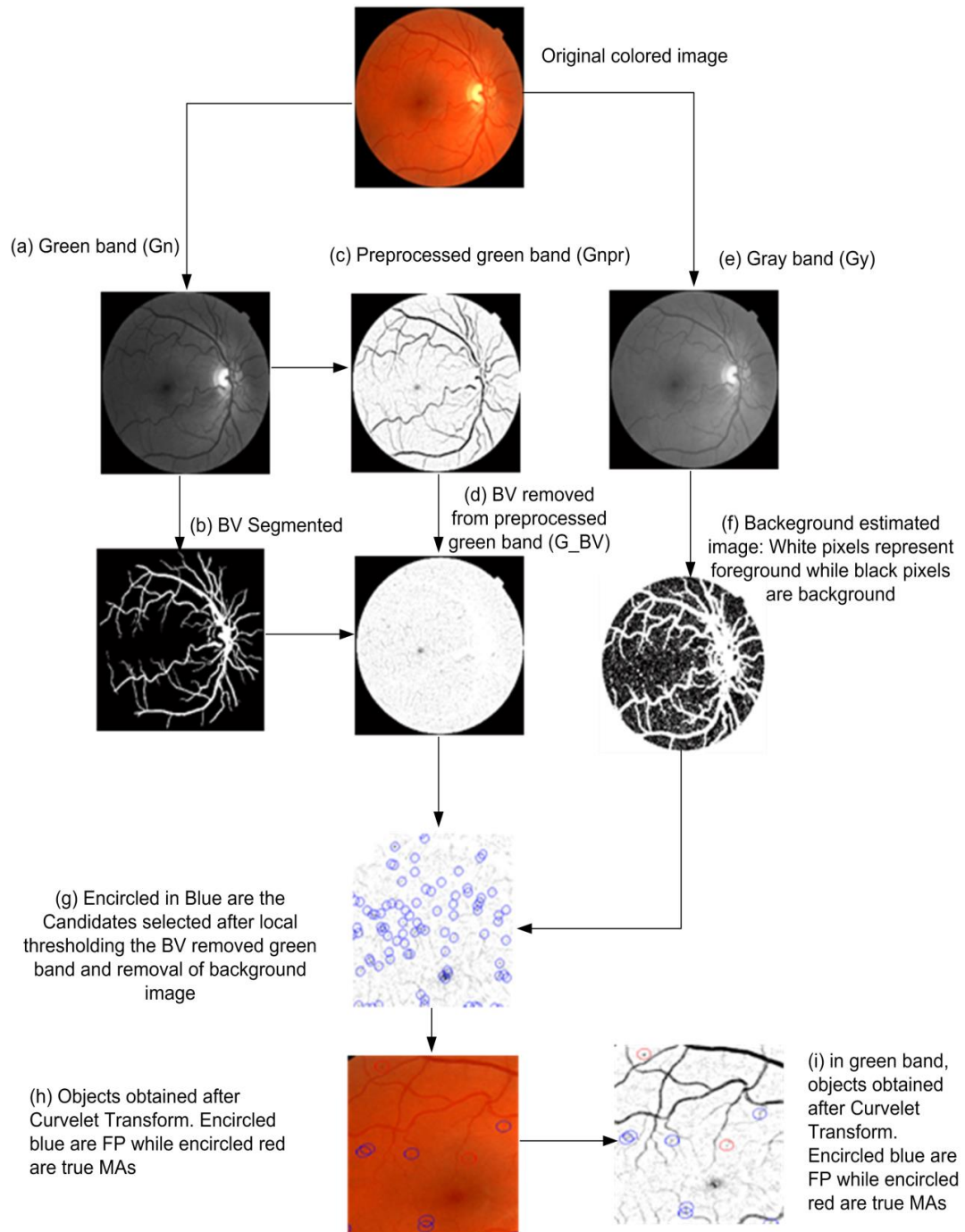


Figure 3.1: Automated MA detection system flow chart

Finally in stage three, false MA candidates are removed using Curvelet Coefficient based features. Shown in Figure 3.1(h) and Figure 3.1(i) are the objects after classification in colored and green band respectively.

3.2.2.1 Candidate Selection

Candidate selection is done in two parallel processes i.e. local thresholding and background estimation based. Candidates that are selected by both are kept as the potential MA candidates. Following steps are involved in candidate selection:

- a) Preprocessing
- b) BV extraction
- c) MA candidate selection using local thresholding
- d) Background estimation and removal of false positives

a) *Preprocessing*

As described in the section 3.2.1, ROC dataset will be used to evaluate the performance of the proposed system which consists of images at different sizes. Therefore, the height of all the images is resized to a standard 800-pixel while maintaining their original width/height ratio. After resizing, fundus image is divided into red band (Rd), green band (Gn), and gray band (Gy). We preprocessed the green band as the MAs being red are well contrasted in green band. Color fundus images suffer from non-uniform illumination. These images also have low and varying contrast. To address the problem of non-uniform illumination, a median filter with large kernel size is used to estimate the background followed by division of the image by its background estimated image. We estimated the background of green band by using a median filter with a 35 x 35 kernel and subsequently the green band is divided by the background estimated image to obtain image Gnb. Using another median filter with a small kernel of size 5x5, the noise in Gnb is minimized. To overcome the problem of low and varying contrast, histogram specification is utilized. We performed histogram specification on noise minimized image to get preprocessed image, denoted by Gnpr as shown in Figure 3.2.

b) *Blood Vessel Extraction Based on Gabor Wavelet*

To extract the blood vessel, Soares et al. [94] method is used. This method is described here for completeness sake. This method is based on two-dimensional (2-D) Gabor wavelet transform responses taken at multiple scales and Gaussian mixture model (GMM) classifier. Soares et al.[94] chose the 2-D Gabor wavelet because it has directional selectiveness capability of detecting oriented features and can be fine-tuned to specific frequencies. The 2-D Gabor wavelet is defined as:

$$\psi_G(x) = e^{jk_0x} e^{-\frac{1}{2}|Ax|^2} \quad (3.1)$$

where A is 2x2 diagonal matrix and $A = \text{diag}[\epsilon^{-\frac{1}{2}}, 1]$, $\epsilon \geq 1$, anisotropy of the filter is defined by it. The parameter k_0 defines the frequency of the complex exponential. The filter is made elongated by setting $\epsilon = 4$ and k_0 is set to $[0, 3]$. Due to the fact that Gabor wavelet responds strongly to high contrast edges, borders of the camera's aperture may lead to false detection as a consequence. In order to reduce this effect, a preprocessing technique is proposed in which region of interest (ROI) is iteratively grown as explained below:

- i. Determine the set of pixels of the exterior border of ROI, here called I_{bod} . I_{bod} pixels are defined as those pixels that are outside the ROI and are neighbors (using 4-neighborhood) to pixels inside it.
- ii. Each pixel value of this set I_{bod} , is replaced with the mean value of its neighbors inside the ROI, here using 8-neighborhood.
- iii. Expand the ROI by inclusion of this set of changed pixels.
- iv. Repeating steps (i) - (iii) results in artificially increasing the ROI.

Figure 3.3, shows an example of increased ROI. Features are the maximum response of the Gabor wavelet over all possible orientations at each scale. Mathematically this can be described as:

$$M_\psi(b, a) = \max_{\theta} |T_\psi(b, \theta, a)| \quad (3.2)$$

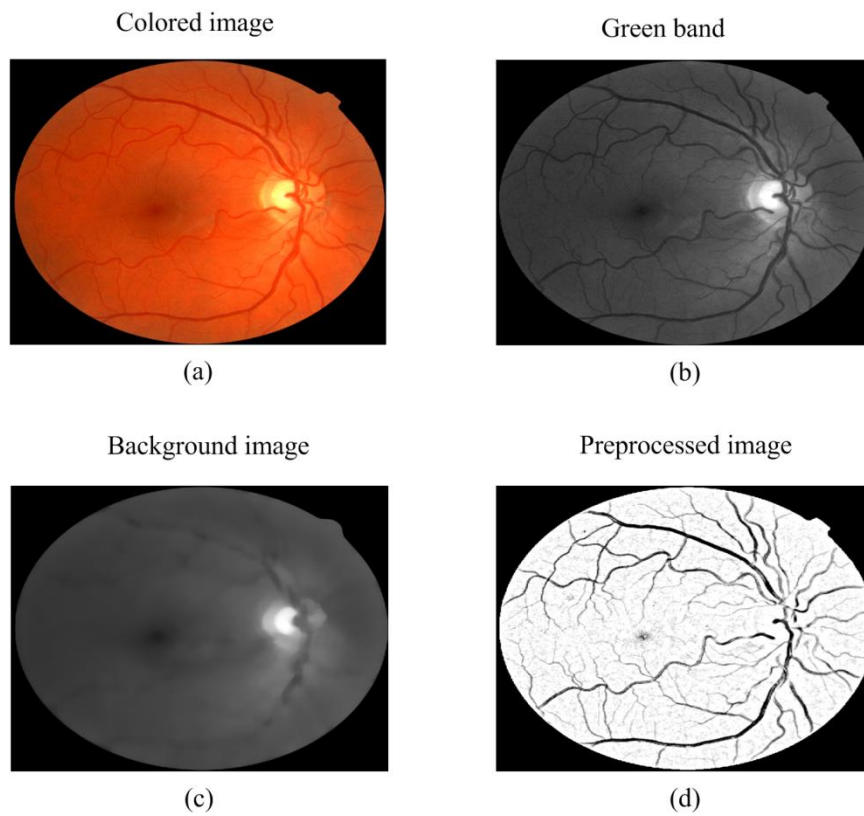


Figure 3.2: Preprocessing of fundus image. (a) Original color fundus image (b) Green channel (c) background estimation (d) Pre-processed image

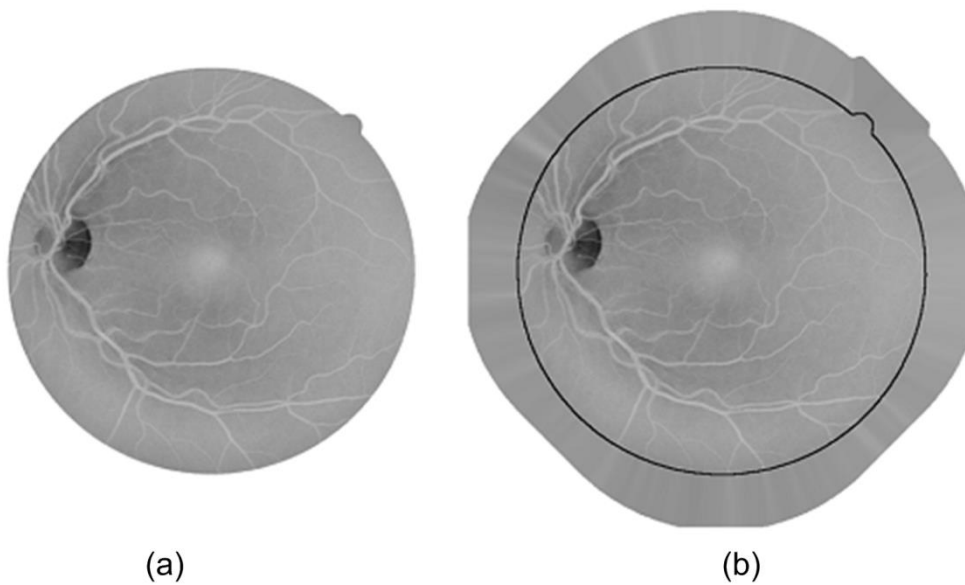


Figure 3.3: Preprocessing to artificially increasing the ROI. (a) original ROI (b) artificially increased ROI, reproduced from [94]

where a is scale parameter, b is the position and θ represents the angle/orientation parameter. From 0° to 170° in the steps of 10° , Gabor wavelet is taken and the maximum response, using above formula, is found and kept as feature. To accommodate all the blood vessel of different widths, four scales i.e. $a=2, 3, 4, 5$ are used. Thus for each pixel in total five features are extracted, which are the maximum response of Gabor wavelet over all angles on four scales and intensity of the pixel in inverted green channel. Thus using these features Gaussian Mixture Model (GMM) is trained. More details about GMM can be found at [116-118]. Shown in Figure 3.4, is training and testing of the classifier. The left diagram illustrates the supervised training of a classifier. The trained classifier can then be applied to the segmentation of test images, as illustrated in the right diagram in Figure 3.4. The training data consists of randomly selected one million pixels from 20 training images of the DRIVE dataset images[119] and the trained classifier is tested using DRIVE test dataset of 20 images. Subsequently the trained GMM classifier is used to segment the blood vessel from the Gn of ROC dataset as shown in Figure 3.1(b). Blood vessels are bright objects once inverted green band is used. Therefore, keeping low threshold will result in not only detecting almost all the vessels but also many of the MAs will be removed as part of blood vessels, whereas keeping threshold high will result in missing many vessels but only few of the MA will be removed as part of blood vessel. Thus in this step threshold is kept high so that those MAs near to blood vessels can be isolated. Keeping threshold high results in better sensitivity as many of the MAs are not removed along with blood vessel but many segments of blood vessel are also undetected which adds to false positives. These blood vessels are removed from the Gnpr to obtain BV-removed image, denoted by G_{-BV} as shown in Figure 3.1(d).

c) MA candidate selection using local thresholding

MAs appear dark in the green band similar to the retinal blood vessels, and can be extracted using threshold. Using global thresholding, many of the true MAs are not captured if the threshold is set too high [120]. On the other hand,

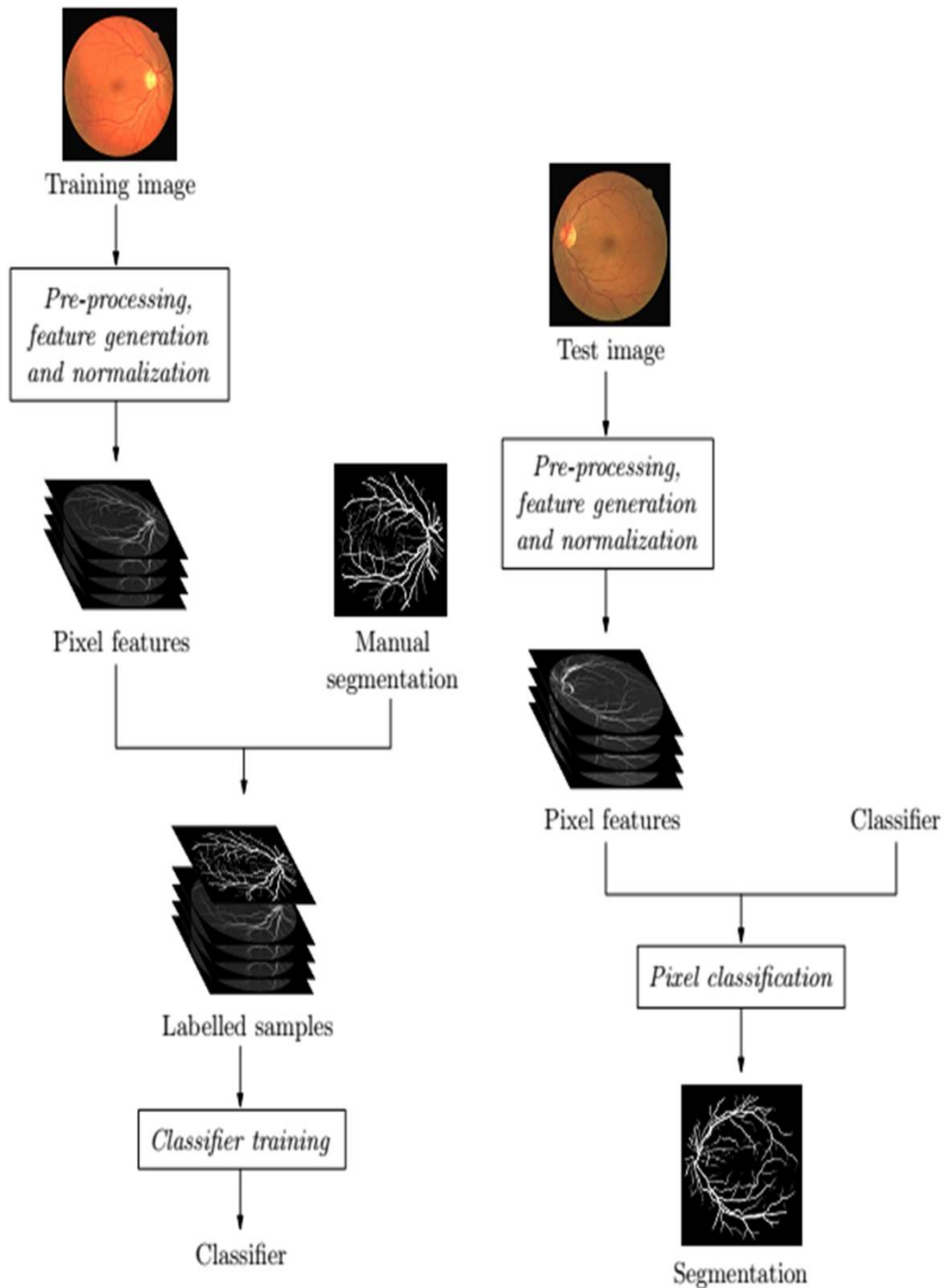


Figure 3.4: Supervised pixel classification approach, reproduced from[94]

many MAs and background subjects would clump together if the threshold is kept too low. Both missing MAs and having multiple MAs clumped together caused lower MA count than the actual number. This effectively reduced the sensitivity of MA detection. As intra- and inter-image variability in intensity was significant in color fundus image datasets, local thresholding was adopted

instead. Based on minimum intensity in a small window of size 9x9 (empirically determined value), we binarized each pixel in the G_{BV} image to obtain candidate image, denoted by G_{lt} , a part of which is shown in Figure 3.1 (g). Since we use none-overlap window, so we have one MA candidate in almost each and every window with exception of those in which all the pixels are dark. Thus in this step we detect almost all of the MAs accompanied by thousands of false positives.

d) *Background Estimation and Removal of False Positives:*

From gray channel image (G_y), shown in Figure 3.1 (e) we also detect the candidates. Based on per pixel contrast (PPC) and standard deviation (STD), we classify each pixel into MA and background, as shown in Figure 3.1(f). PPC is defined as the average intensity difference between a pixel and its adjacent pixel. Using 17x17 window (the window size is empirically determined), PPC and STD are calculated. We randomly selected 10 images containing 50 MAs and 50 background regions to estimate the values for PPC and STD. Based on the estimated values for background, all the pixels in the images are classified into background and foreground. Foreground pixels are assigned value equal to one while background pixels are assigned value of zero as shown in Figure 3.5 (b). In this case we keep the threshold low so that as many MAs as possible are picked. The image thus obtained is denoted by G_{fb} . We multiple the two images to obtained G_{cand} i.e.

$$G_{cand} = G_{fb} \times G_{lt} \quad (3.3)$$

Thus G_{cand} image contains most of the MAs while many of the false candidates that are from background are removed. At this stage the F_P s are mainly from traces of the BV and the background, some of these are from red lesions. Therefore, many candidate pixels are close to each other and actually belong to single object. Thus we merge all those candidates which are in the neighborhood of one pixel and have similar intensity.

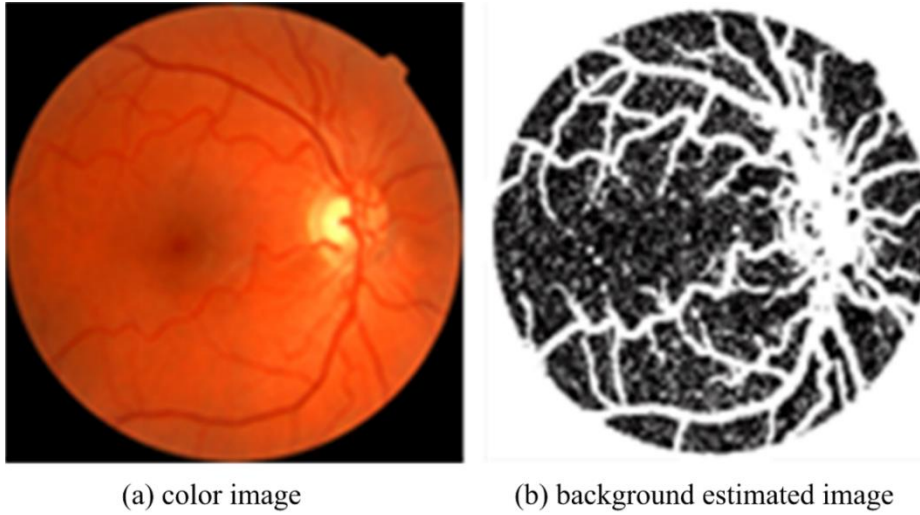


Figure 3.5: (a) color image (b) background estimated image (G_b)

3.2.2.2 Candidate Feature Extraction

In general, MAs are red in color and have round shape. Based on their morphology and intensity, we use three feature sets to describe the MAs, namely color-based, Hessian matrix-based, and Curvelet coefficients-based features.

a) Color Based features

The color features are one of the important descriptors in pattern recognition and computer vision. In the proposed system many of the F_{Ps} are those that are not red in color. Hence many F_{Ps} are removed in this stage. Color based features we use in the proposed system include:

1. Mean intensity in red band: Mean intensity in red band E_{meanRB} is defined as sum of values of pixels in a region divided by the total number of pixels in a region. Mathematically it can be written as:

$$E_{meanRB} = \frac{1}{M \times N} \left(\sum_{i=1}^M \sum_{j=1}^N RB_{norm}((i, j)) \right) \quad (3.4)$$

where M and N are the number of rows and column in the region. And RB_{norm} is normalized region in red band obtained by normalizing red band using following equation [121]

$$\hat{v}_i = \frac{v_i - \mu_i}{\sigma_i} \quad (3.5)$$

where v_i is the i^{th} feature assumed by each pixel, μ_i is the average value of the i^{th} feature, and σ_i is the associated standard deviation.

2. Standard deviation in red band: Standard deviation of red band or Std_r is defined as measure of the degree of spread among a set of intensity values or a measure of the tendency of individual intensity values to vary from the mean intensity values in the red band. Mathematically it can be described as:

$$Std_r = \left(\frac{1}{n-1} \sum_{k=1}^n (RB_{norm} - E_{meanRB})^2 \right)^{\frac{1}{2}} \quad (3.6)$$

where n is total number of pixels in the region.

3. Mean intensity in green band: Mean intensity in green band E_{meanGB} is defined as sum of values of pixels in a region divided by the total number of pixels in a region. Mathematically it can be written as

$$E_{meanGB} = \frac{1}{M \times N} \left(\sum_{i=1}^M \sum_{j=1}^N GB_{norm}((i,j)) \right) \quad (3.7)$$

where M and N are the number of rows and column in the region. And GB_{norm} is normalized region in green band obtained by normalizing green band using equation 3.5.

4. Standard deviation in green band: Standard deviation in green band or Std_g is defined as measure of the degree of spread among a set of intensity values or a measure of the tendency of individual intensity values to vary from the mean intensity values in the green band. Mathematically it can be described as:

$$Std_g = \left(\frac{1}{n-1} \sum_{k=1}^n (GB_{norm} - E_{meanGB})^2 \right)^{\frac{1}{2}} \quad (3.8)$$

where n is total number of pixels in the region.

5. Histogram based features: Histogram is a graph showing the number of pixels in an image at each different intensity value. This method analyses image based on intensity. In the proposed work histogram based features are histogram of S and V band in HSV color space. Histogram is computed from all of the pixels in the candidate MA in S and V band, and the peaks in the histograms are used as feature to differentiate between MA and false MA.

The color space red, green and blue (RGB) describes the colors in terms of red, green and blue. This color space is defined in terms of combination of primary colors. While in case of HSV color space, colors are described in terms of the Hue, Saturation, and Value as shown in Figure 3.6 . The HSV colors space is similarly to how the human eye tends to perceive color. The HSV model was created by A. R. Smith in 1978 [122]. The coordinate system is cylindrical, and the colors are defined inside a hexcone. Details can be found in [122]. In RGB space, most of the information is available in green and red bands. Therefore, we use only green and red bands. Similarly for HSV, we use S and V bands. The above color features are calculated using 11x11 circular window centered on the center of the candidate objects, the size of the window is empirically determined.

b) Hessian Based Features

The Hessian matrix is a square matrix which is composed of second-order partial derivatives of multivariable scalar valued function. Shape characteristics of objects can be captured based on eigen values of the Hessian matrix[123]. Hessian matrix for 2D image is given by:

$$H = \begin{bmatrix} I_{xx} & I_{xy} \\ I_{yx} & I_{yy} \end{bmatrix} \quad (3.9)$$

where I_{xx} and I_{yy} are the second order partial derivatives of image I and I_{xy} and I_{yx} are the mixed derivatives of image I . Based on the fact that $I_{xy} = I_{yx}$, it can be stated that the Hessian matrix is symmetrical with real eigenvalues

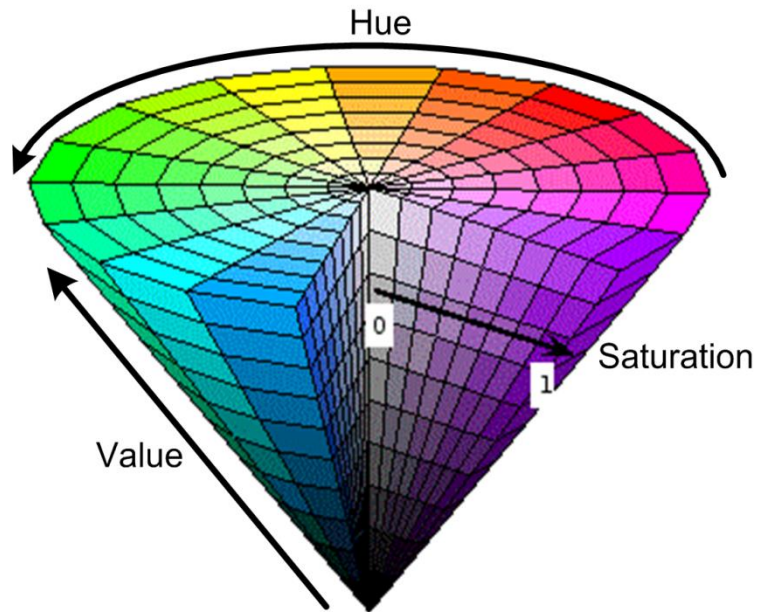


Figure 3.6: HSV color space

and orthogonal eigenvectors. The eigenvalues of the Hessian, represented by λ_1 and λ_2 , taking $|\lambda_1| \leq |\lambda_2|$, measure convexity and concavity in the corresponding eigen directions. The eigenvalues of H are called principal directions/ curvatures and are directions of pure curvature (no mixed partial derivative). They are always orthogonal and invariant under rotation. Different structures such as tubular, blob etc. can be detected based on these eigenvalues [124]. In the proposed system we use four Hessian features. These are the eigenvalues, their product, and their ratio. Using 17x17 window centered on candidate MA, the aforementioned features are extracted.

c) Curvelet Coefficient

The basic concept of Curvelets is to represent a curve as a superposition of multiple functions of various lengths and widths obeying the scaling law $\text{width} \approx \text{length}$. Because Curvelet Transform (CT) has a highly redundant dictionary. Thus for those signals that have edges along regular curve, it can provide sparse representation. It is localized in angular orientation in addition to localization in spatial and frequency domains a very important feature missing in the classic wavelet transform. Initial construction of Curvelet has been redesigned and was reintroduced as fast digital CT [125]. Most natural images/signals exhibit line-like edges, i.e., discontinuities across curves (so-

called line or curve singularities). Traditional wavelets perform well only at representing point singularities, since they ignore the geometric properties of structures and do not exploit the regularity of edges. The solution to this problem and some other limitations of the wavelet is provided by CT. Unlike the isotropic elements of wavelets, the needle-shaped elements of this transform possess very high directional sensitivity and anisotropy [95]. Before explaining Curvelet transform in 2-D, we define some terms. Let x be a spatial variable, w as frequency-domain variable, and with r and θ polar coordinates in the frequency domain. We have, $W(r)$ radial window and $V(t)$, angular window, which are smooth, nonnegative and real valued. With W taking positive real arguments and supported on $r \in (1/2, 2)$ and V taking real arguments and supported on $t \in [-1, 1]$. These windows will always obey the admissibility conditions [125] :

$$\sum_{j=-\infty}^{\infty} W^2(2^j r) = 1, \quad , r \in \left(\frac{3}{4}, \frac{3}{2}\right) \quad \square \quad (3.10)$$

$$\sum_{l=-\infty}^{\infty} V^2(t - l) = 1, \quad , t \in \left(-\frac{1}{2}, \frac{1}{2}\right) \quad \square \quad (3.11)$$

Now, for each $j \geq j_0$, we introduce the frequency window U_j defined in the Fourier domain by

$$U_j(r, \theta) = 2^{\frac{-3j}{4}} W(2^{-j} r) V\left(\frac{2^{\lfloor \frac{j}{2} \rfloor} \theta}{2\pi}\right) \quad (3.12)$$

Thus the support of U_j is a polar “wedge” defined by the support of W and V , the radial and angular windows, applied with scale-dependent window widths in each direction. Define the waveform $\varphi_j(x)$ by means of its Fourier transform $\hat{\varphi}_j(\omega) = U_j(\omega)$, let $U_j(\omega_1, \omega_2)$ be the window defined in the polar coordinate system by (3.12). We may think of φ_j as a “mother” Curvelet in the sense that all Curvelets at scale 2^{-j} are obtained by rotations and translations of φ_j .

With rotation angles

$$\theta_l = 2\pi \cdot 2^{\lfloor j/2 \rfloor} \cdot l \quad (3.13)$$

where $l = 0, 1, \dots, 4 \cdot 2^{\lfloor j/2 \rfloor} - 1$, such that $0 \leq \theta < 2\pi$. It should be noted that the spacing between the consecutive angles depends on scale. For example in case of 2nd scale, we have 8 orientations/angles in total, while in case of 4th scale, we have total 16 orientations/angles. Thus at higher scale, we have higher orientations/angles resolution.

Similarly, the sequence of translation parameters are $k = (k_1, k_2) \in \mathbb{Z}^2$. Now we define Curvelets (as function of $x = (x_1, x_2)$) at scale 2^{-j} orientation θ_l , and position:

$$x_k^{(j,l)} = R_{\theta_l}^{-1}(k_1 \cdot 2^{-j}, k_2 \cdot 2^{-j/2}) \quad (3.14)$$

by

$$\varphi_{j,l,k}(x) = \varphi_j\left(R_{\theta_l}(x - x_k^{(j,l)})\right) \quad (3.15)$$

where R_θ is the rotation by θ radians.

$$R_\theta = \begin{pmatrix} \cos\theta & \sin\theta \\ -\sin\theta & \cos\theta \end{pmatrix} \quad (3.16)$$

A Curvelet coefficient is then simply the inner product between an element $f \in L^2(\mathbb{R}^2)$ and a Curvelet $\varphi_{j,l,k}$,

$$c(j, l, k) := \langle f, \varphi_{j,l,k} \rangle = \int_{\mathbb{R}^2} f(x) \overline{\varphi_{j,l,k}(x)} dx \quad (3.17)$$

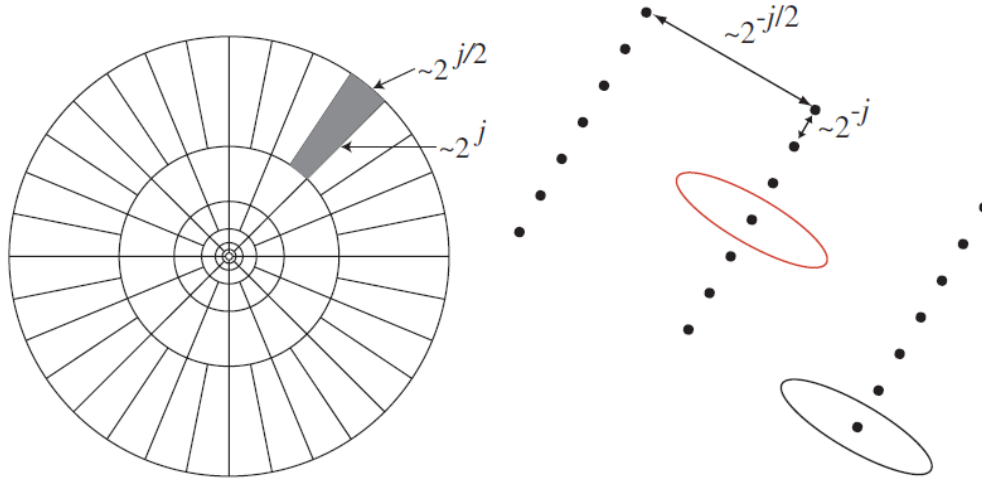


Figure 3.7: Curvelet tiling of space and frequency, reproduced from [125]

Referring to Figure 3.7: Curvelet tiling of space and frequency, reproduced from [125], parabolic shape of wedges is achieved by splitting the Fourier plane into radial and angular divisions. Image is decomposed into multiple scales (different frequency bands) using the concentric circles. Similarly different orientations/angles in particular band are obtained by angular divisions. Therefore, scale j and angle l is used to deal with a particular wedge. Taking the inverse FFT of such a wedge corresponds to an ellipse as shown in Figure 3.7 right. This indicates that the inverse FFT of a particular wedge if taken, will determine the Curvelet coefficients for that scale and angle [126]. Figure 3.7 represents the continuous Curvelet transform tilings, in case of digital coronization, we have Cartesian arrays where coronae and rotations of continuous time are not especially adapted to Cartesian arrays. So in this case we have Cartesian coronae which are based on concentric squares instead of circles and shears instead of rotations, as shown in Figure 3.8.

The digital counter part of equation 3.12 is

$$U_j(\omega) = W_j(\omega)V_j(\omega) \quad (3.18)$$

while we have shear matrix instead of rotation matrix in digital domain.

$$S_\theta = \begin{pmatrix} 1 & 0 \\ -\tan\theta & 1 \end{pmatrix} \quad (3.19)$$

where S_θ is the shear matrix.

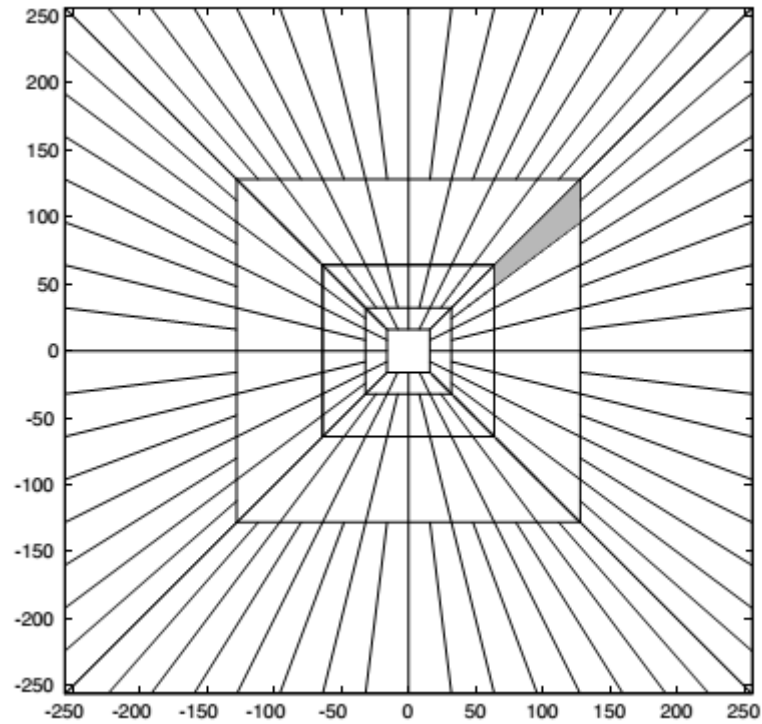


Figure 3.8: The figure illustrates the basic digital tiling. The windows $\tilde{U}_{j,l}$, smoothly localize, reproduced from [100]

Curvelets are used in many medical image analysis applications like computed tomography [127], breast cancer diagnosis in digital mammogram [128], ulcer detection[129], retinal image analysis [92], and so on.

d) Curvelet Coefficient Based Features

The second generation Curvelet transform called Fast Digital Curvelet Transform (FDCT) was introduced by [125] by redesigning the initial construction of the Curvelet. This second generation FDCT is simpler to understand, use, also faster and less redundant compared to its first generation version. Algorithm of CT is shown in Figure 3.9. It is based on two windows, namely scale window V and radial window W, and consists of four steps:

1. Compute the 2-D Fourier transform of the original image.
2. For each scale s and orientation n , estimate frequency window $U_{s,n}$ as a product of the scale and radial windows.
3. Wrap this product around the origin.

4. Compute a 2-D inverse fast Fourier transform to derive the Curvelet coefficients.

More details and mathematical description can be found in [125]. In digital implementation of the CT, the two main parameters are:

- a. number of scales at the coarsest level
- b. number of orientations at the coarsest level

We find in our case that two scales and 16 orientations work well. Based on Curvelet coefficients, we calculate aspect ratio, circulatory, mean energy and standard deviation of energy.

1. Aspect ratio: Aspect ratio A_R is defined as the ratio of the width to the height of an object. It describes the proportional relationship between its width and its height. Mathematically it is expressed as:

$$A_R = \frac{D_w}{D_H} \quad (3.20)$$

where D_w is the width of an object and D_H is its height. For a circular object the value of AR will be one.

2. Circulatory : Circularity C is a function of the perimeter and the area of object and is defined as:

$$C = \frac{4 \times \pi \times A}{P^2} \quad (3.21)$$

where A is area of an object and P is its perimeter. For round object, the value of C will be one.

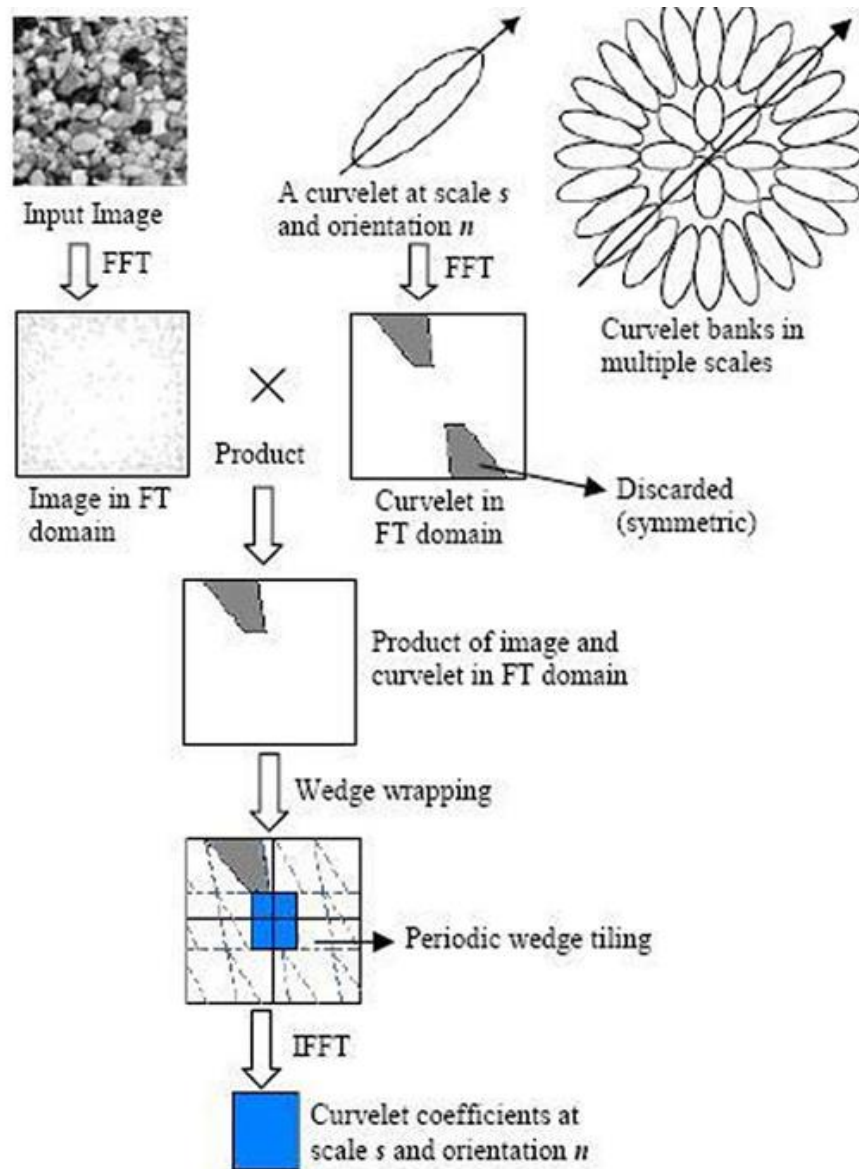


Figure 3.9: Steps of Curvelet Transform, reproduce from [92]

3. Mean energy: Mean energy E_{mean} is defined as the sum of squared values of pixels in a region divided by the total number of pixels in a region. Mathematically it can be written as :

$$E_{mean} = \frac{1}{M \times N} \left(\sum_{i=1}^M \sum_{j=1}^N Pixel(i,j) \right)^2 \quad (3.22)$$

where M and N are the number of rows and column in the region respectively.

4. Standard deviation of energy: Standard deviation of energy Std_{engy} is defined as measure of the degree of spread among a set of energy values or a measure of the tendency of individual energy values to vary from the mean energy values. Mathematically it can be described as:

$$Std_{engy} = \left(\frac{1}{n-1} \sum_{k=1}^n (Engy_k - E_{mean})^2 \right)^{\frac{1}{2}} \quad (3.23)$$

where E_{mean} is the mean of energy and $Engy$ is the normalized energy in different orientations.

3.2.2.3 Candidate Classification MA and false MA

A simple rule based classifier is designed to classify the candidates into MA and false MA. To estimate the range of values we select 10 images. Out of these 6 images contain MA whereas 4 images do not contain any MA. The values of very clear MAs and false positives are selected and used for estimating the range of parameters. Based on the range selected, we test those 10 images and by trial and error a range of parameters are found as shown in Table 3.2. After finding the range of parameters value, we test all the fifty images. The classification is done in three sequential stages. In stage one, using color features we remove the false positives which are from non-red objects. In stage two, using Hessian matrix based features we remove those candidates that are from traces of blood vessels and other elongated objects. While in stage three, Curvelet Coefficients based features are utilized to remove non-circular objects.

Table 3.2 : Parameter values

Filter	Function	Parameters range
--------	----------	------------------

Median filter	Background estimation	35x35
Median	Noise removal	5x5
Color RGB	Std in red band	0.0106<R_std>0.167
Color RGB	Std in green band	0.006641<G_std>0.120945
Color RGB	Mean intensity in red band	-0.0434<R_mean>0.1915
Color RGB	Mean intensity in green band	-0.0320<G_mean>0.137780
Color HSV	Intensity values in S channel	0.78<S
Color HSV	Intensity values in V channel	0.65<V
Hessian	λ_1	$\lambda_1>0$
Hessian	λ_2	$\lambda_2>0$
Hessian	$\lambda_1 \times \lambda_2$	$\lambda_1 \times \lambda_2>0$
Hessian	Ratio of λ_1 and λ_2 ($R_{o1,2}$)	$R_{o1,2}<85$
Curvelet	Aspect ratio (AR)	$AR<3.7$
Curvelet	Circulatory (C)	$0.1<C<1.5$
Curvelet	Mean Energy (E_{mean})	$E_{mean}<5.9$
Curvelet	Std of Energy (Std_E)	$Std_E>1.5$

3.2.3 Evaluation Metrics for Microaneurysm Detection

The performance of the automated MA detection system will be evaluated using free-response receiver operating characteristic (FROC) curve. FROC is the plot of sensitivity (see appendix C) vs. average number of false positives per image (see appendix C). In this plot sensitivity is on the y axis while average number of false positives per image is on the x-axis. It can extend indefinitely to the right, but the ordinate is limited to unity or less.

3.3 Summary

In this chapter, the methodology of the proposed MA detection has been presented. The proposed system for MA detection is designed to have maximum sensitivity. The candidates are extracted in two parallel steps. To achieve better sensitivity with

comparable number of false positives, a three stage sequential mechanism to remove the false positives has been proposed. Thus using features based on color, Hessian and Curvelet, most of the false positives are expected to be removed while keeping maximum number of microaneurysms. The results of the automated microaneurysm system are presented in chapter 4 section 4.2 and 4.3.

CHAPTER 4

RESULTS AND DISCUSSION ON MICROANEURYSM DETECTION

4.1 Overview

This chapter discusses the evaluation of the proposed microaneurysm detection system. As illustrated in chapter 3, in case of MA detection, the preliminary MA candidates were extracted using local thresholding and background estimation. The false positives were removed using three sequential stages: color features based, Hessian based and Curvelet transform based. The overall results and discussion of the proposed system for MA detection are described in section 4.3, while section 4.4 concludes the chapter with a summary.

4.2 Automated Microaneurysm Detection

This section presents the results of the proposed system. We have used 50 images from ROC dataset to test the proposed system. Out of these 50 images, only 37 images contain MAs, while the remaining 13 images do not contain any MA. The total number of MAs in these 37 images is 336. Our aim is to detect as many MAs as possible in each stage. We used the inverted green band, so MAs were bright objects. Therefore, we kept flexible threshold in all the stages to get the maximum sensitivity albeit with many false MA detections also.

4.2.1 Blood Vessel Segmentation Based on Gabor Wavelet

In the inverted green band, both blood vessel and MA are high intensity objects as both are red in color fundus images. Having same color, blood vessel are generally mistaken as MA. Therefore, it is important to remove the blood vessel before candidate MA

extraction. Based on Gabor wavelet approach proposed by Soares et al. [94], we segmented the blood vessel from ROC dataset, two examples are shown in Figure 4.1. Gabor wavelet being sensitive to edges detects most of the vessels. But

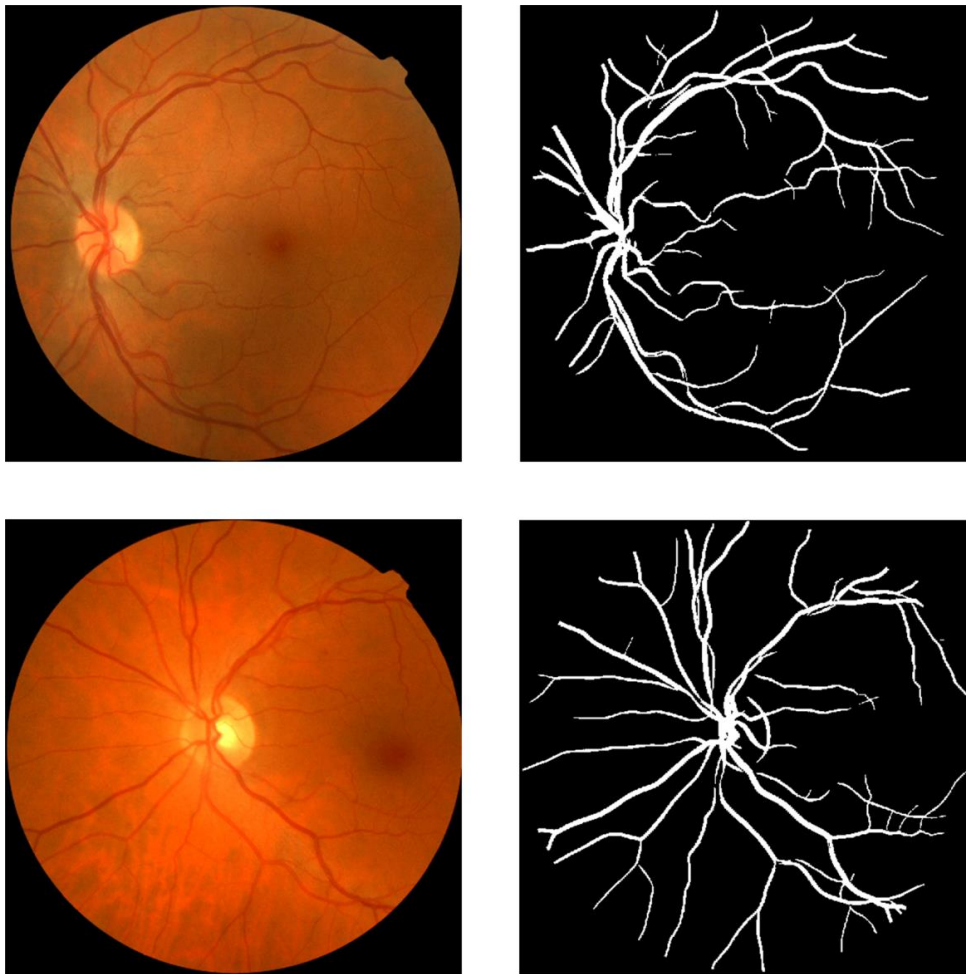


Figure 4.1: Examples of BV segmentation based on Gabor Wavelet. Right column colored ROC images, left column segmented vessels.

there are many MAs which are not only positioned close to blood vessels but also low intensity variation in the region between MA and the nearby blood vessel. In such cases keeping the same threshold as used by the Soares et al. [94] will result in removal of those MAs along with blood vessel. This is because at low threshold, MAs might be clumped together with blood vessel and will also be removed as part of the blood vessel. Thus to retain such MAs we used higher threshold values. In this way we are able to keep those such MAs. However keeping high threshold will result missing many vessels also, and in this process many broken pieces of the vessel may contribute to false positives. These false positives were expected to be removed in latter stages. Thus we could maintain the high sensitivity. In this stage, we missed only few MAs which are

clumped together with blood vessels unintentionally and removed along with the blood vessels.

4.2.2 MA Candidate Selection

As discussed in chapter 3, in the green band, MAs are dark objects with low intensity. We used 9×9 window on preprocessed blood-vessel-removed images and the pixel with lowest intensity was identified as candidate MA. In this step, most of the MAs with thousands of false positives were detected. Local thresholding was used because of the problems with global thresholding, as shown in Figure 4.2. As the intensity values of all the pixels in any MA may not be the same, and each MA may be present in more than one window, thus the candidate selection is not pixel-by-pixel. Therefore, after local thresholding, we merged all those candidates which were one pixel apart. The possible MA detection count was 196 MAs out of 336, because the rest of 140 MAs or 41.666% of the total MAs were very faint and could not be detected. After the local thresholding, a very huge number of average false positives per image remained as expected. Most of these false positives were from background, traces of blood vessels and hemorrhages.

4.2.3 Background Estimation

As the color fundus images are reddish in color, using intensity-based candidate selection will select many of the background pixels as candidate MAs. Thus it is important to estimate the background and remove those candidates from background. In this step, most of the false positives that were from background were removed. Although some of the MAs were also removed during this process, the false positive reduction was significantly more than the true positive removal. After this stage, we had a sensitivity of 52.97% (178/336 MAs) with 250 false positives per image.

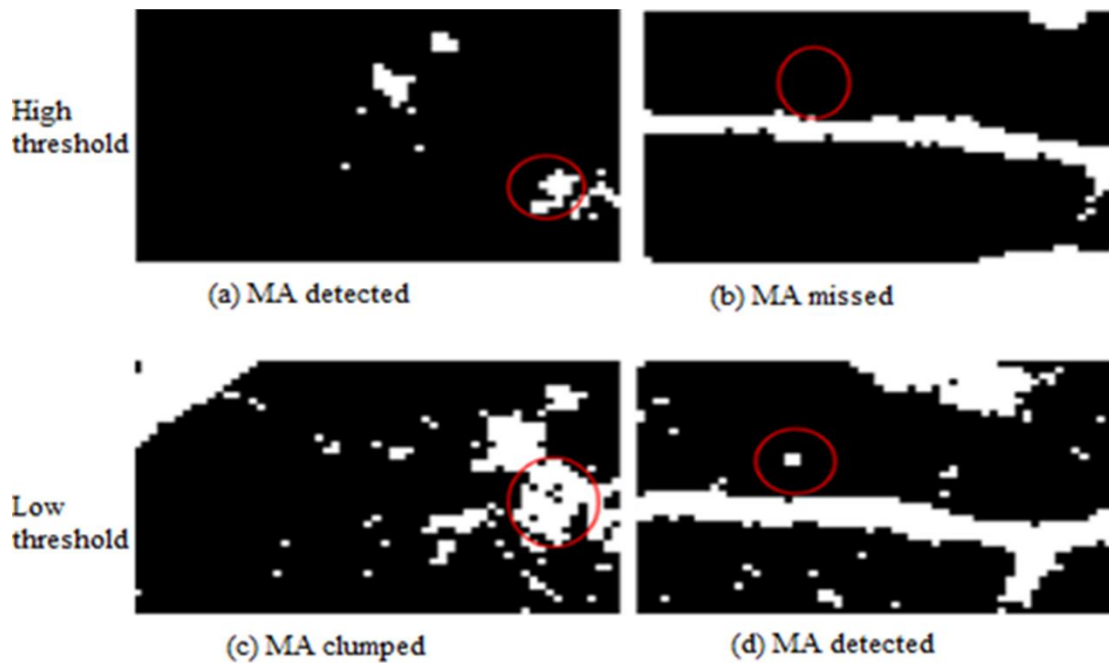


Figure 4.2: At high threshold MA (encircled in red) in (a) is detected and in (b) is missed. At low threshold, MA in (a) large cluster of pixels (c), but the MA previously missed in (b) can now be detected (d)

4.2.4 Color Based Features

The two main characteristic features of MA are their color and shape. MAs are red in color. So using this feature is helpful in differentiating between MAs and false positives. Although we could have used this feature alone without using background estimation, color fundus images suffer from non-uniform illumination and varying contrast. It is easy to mistakenly remove the MA while removing the false positives due to background. Thus to detect most of the MAs and also keeping better specificity we added an extra step of background estimation and removal of false positives due to background. The sensitivity and false positives per image were 50.59 and 144 respectively after color based features classification stage. Here we lost 2.3% of the total MAs while there was 42.4% reduction in average false positives per image. Therefore, in this step the priority was to remove as many false positives as possible, at the expense of losing several true MAs. This also shows that color features have high potential to differentiate between MAs and false positives.

4.2.5 Hessian Based Features

As described in the methodology chapter on microaneurysm detection, threshold to remove the blood vessel was kept high in order to achieve maximum sensitivity. Though high threshold enabled the system to detect most of the MA near the blood vessel, this also resulted in missing many traces of blood vessel. As Hessian based features are robust in detecting tubular structures such as blood vessels and other such objects, therefore they were utilized to remove the elongated objects such as blood vessel which were false positives. This enabled us to detect those MAs which were very close to blood, with few false positives per image.

4.2.6 Curvelet Based Features

As we have discussed in previous section, MAs are round in shape. This parameter is vital in discriminating the MAs and false positives. Most of the false positives were removed in background estimation stage, color based features stage and Hessian stage. The candidate objects that were left up to this stage were those objects which were somehow non-elongated and red in color. The problems in color fundus images i.e. non-uniform illumination and low and varying contrast, not only affects the color but it also affects the shape of the MAs. Also, there are many MAs in the ROC dataset which do not look round in shape, thus using shape parameter to detect MA in such case becomes very difficult. Using shape parameters on Curvelet coefficient, we were able to differentiate MAs and false positives. In this stage, those objects which are not circular in shape were removed. Many of the false positives were removed with very few loss of MAs. Thus we achieved better sensitivity with comparable number of average false positives per image.

4.3 The Overall Results and Discussion

The results of the proposed system and those previously reported in literature are shown in the Table 4.1. Out of the 336 MAs, the proposed approach was able to detect 162 MAs, achieving a sensitivity of 48.21% with 65 FPPI. This result is favourably-comparable to the state-of-the-arts, although only simple rule-based classifier was implemented. Unlike the method by Adal et al. [14] that employed four supervised classifiers and 87 features in total to select an optimum classifier-feature pairing to

remove False Positives, the computation of the proposed system is simpler and faster albeit at the expense of higher FPPI. In this work, we aimed to achieve high sensitivity in MA detection, i.e. to detect as many MAs as possible from fundus images. We used local thresholding technique in identifying MA candidates and kept the threshold to a low value as our approach to achieve maximum possible sensitivity, at the cost of hundreds of FPs per image. These FPs at this initial stage were mainly due to background of the fundus images and blood vessels. We used statistical features to estimate the background and remove those candidates that were from background. In addition, during the blood vessel extraction stage, we kept the threshold to a low value so that only true blood vessels were extracted. This helped us in detecting MAs near the BV and ultimately improving the sensitivity. However this resulted in introducing many FPs as there were many traces of blood vessels. To eliminate those blood vessels, we used the Hessian matrix based features. Thus the proposed system could detect MA near to the blood vessels with reasonably good specificity. Figure 4.3 illustrates examples of MA detected in close vicinity to blood vessels.

To our best knowledge, Curvelet Transform is used for the first time in MA detection. Curvelet Transform is fast and robust at detecting objects with curved singularities. We used features including shape parameters based Curvelet coefficients to discriminate between MAs and non-MAs. The results indicate that Curvelets are very effective at detecting round objects such as MAs. Table 4.1 further shows our approach achieves the highest sensitivity, among reported approaches. Admittedly, the FPPI is higher than Adal's but a simpler solution is perhaps better as Oscar's razor principle suggests. The ROC dataset is a very challenging dataset. It has been observed that general image quality, noise, low and varying contrast make it difficult to detect MAs in this dataset. Figure 4.5 depicts some of the objects detected by the proposed system. The F_p are mostly from blood vessels and hemorrhages (large red lesions). Some of the images are very dark hence in those images the background has also contributed to the F_p . Factors such as variation in fundus image background, low and varying contrast and artifact are found to further limit the MA detection rate. The

Table 4.1: Result comparison of different MA detection methods

Authors	Methodology	Sensitivity	FPPI
Spencer et al. [130]	Top-hat transform	12.00%	20.30
Abdelazeem [51]	Circular Hough Transform	28.00%	505.85
Walter et al. [131]	Diameter closing	36.00%	154.42
Zhang et al. [89]	Multiple Gaussian mask	33.00%	328.30
Lazar et al. [132, 133]	Cross-section profile	48.00%	73.94
Adal et al. [14]	Hessian operator	44.64%	35.20
Proposed method	Curvelet Transform	48.21%	65.00

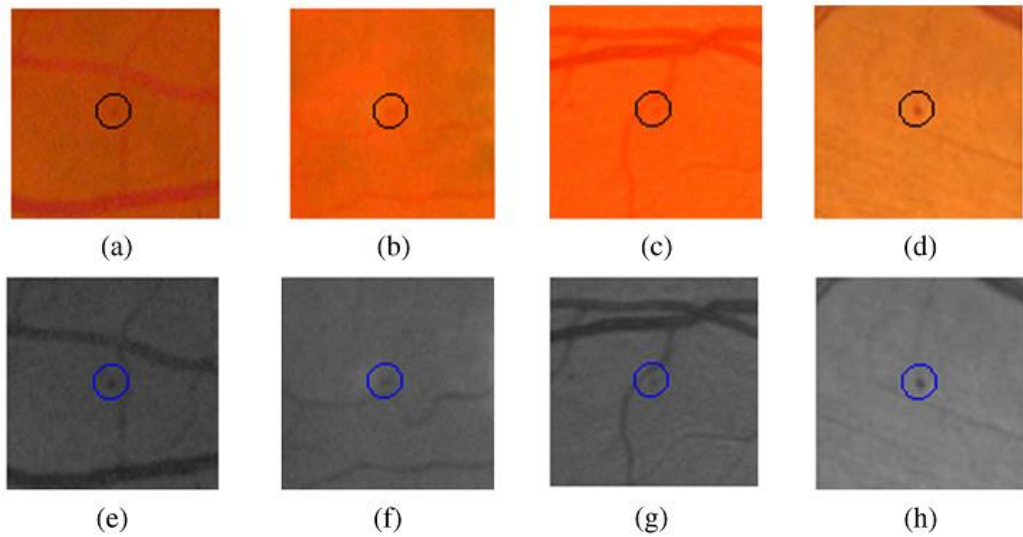


Figure 4.3: Examples of MA that are very close to the BVs but detected by the proposed system: (a)–(d) full color images and (e)–(h) in green band

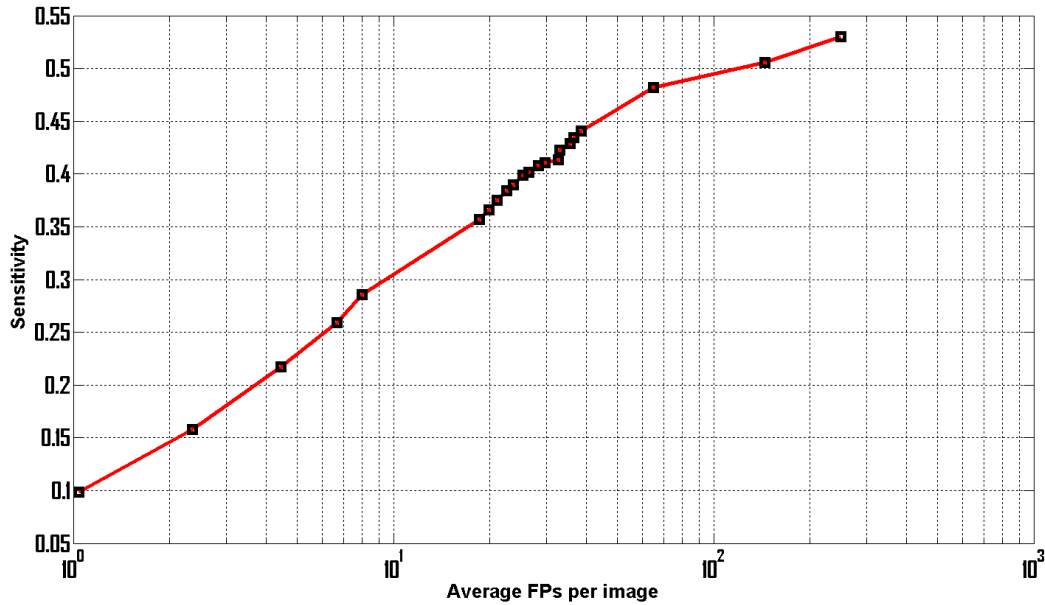


Figure 4.4: FROC plot of the proposed system

cases where the proposed system failed to detect MAs are shown in Figure 4.6, and can be summarized into three categories:

Case I: If central pixel of the MA is not the darkest point, then in some cases that MA will be missed. The hit criteria specified by ROC [66] is very strict. We assumed that the center point of the MA to be the darkest point. But in some cases the ground truth does not represent the darkest point. In such cases if the darkest point of the detected lesion is not within the specified distance from the ground truth, then it is declared as missed.

Case II: All those MAs which are very faint in color will be missed. As the candidates are extracted based on the assumption that MAs have low intensity in green band i.e. dark in color as intensity level increases from dark/black (value = 0) to faint/white (value = 255). Thus those MAs which are faint in color, i.e. having very high intensity value in green band will be missed. These are the examples of MAs which were missed in the first stage. Most of the missed MAs belong to this category.

Case III: Those MAs having abnormal shape will also be missed. Since the proposed algorithm assumes MAs to be somehow round in shape. So all those MAs selected at the initial stage will be missed in the final stage of classification if they have non-circular shape.

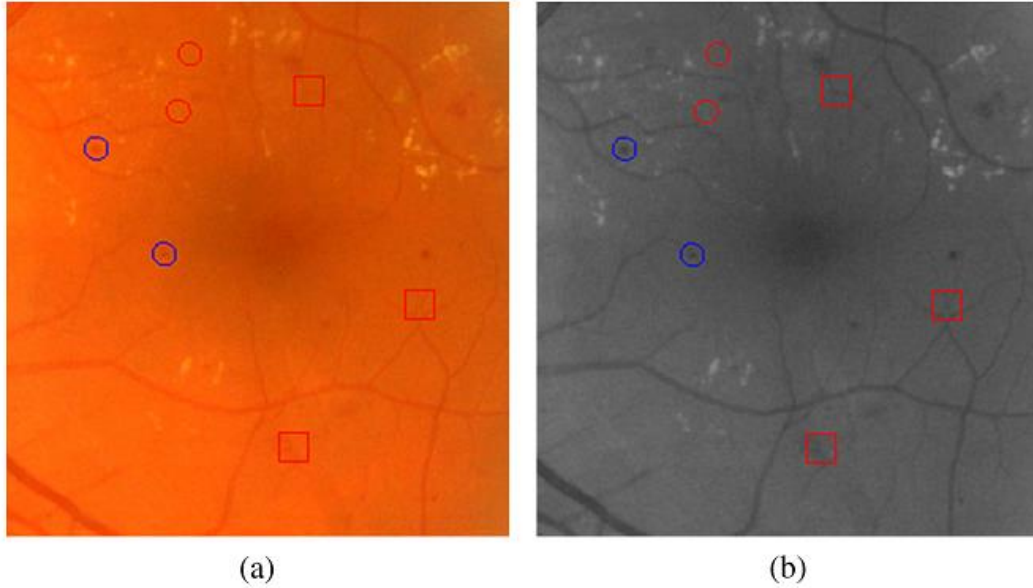


Figure 4.5: Objects encircled in blue are T_P , encircled in red are F_N , whereas objects inside the red squares are F_P , (a) full-color images while (b) in green band

4.4 Summary

In this chapter results and discussion of automated microaneurysms system have been presented. The MA candidates were extracted in two parallel steps namely: local thresholding and background foreground estimation. The candidates were classified into true positives and false positives using rule based classifier which consists of three stages. In stage one, color based features were exploited to remove the false positives. In the second stage using Hessian features, false positives were identified and removed. While in stage three, Curvelet transform was used to differentiate between MA and non-MA. In chapter one section 1.4, it was hypothesized that addressing the false positives by category and Curvelet transform may help to improve sensitivity of microaneurysm detection. We achieved highest sensitivity among all the competitors presented in Table 4.1. The proposed system achieved sen-

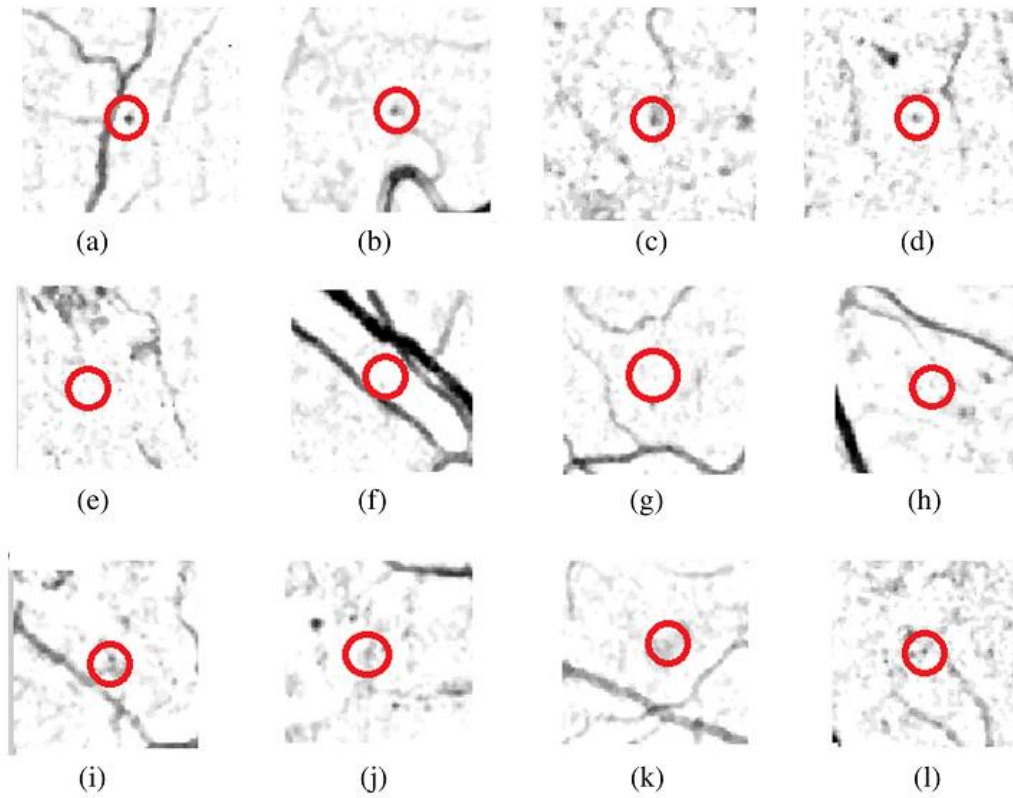


Figure 4.6: Different cases where the proposed system was unable to detect the MAs: (a)–(d) examples of missed MA because the center pixel does not have the minimum intensity, (e)–(h) examples of missed MA because their colors are very faint, and (i)–(l) examples of missed MA due to abnormal shape

sitivity of 48.21% with averaging 65 FPPI. Thus the results prove the hypothesis is positive. In chapter 5, methodology, results and discussion on blood vessel segmentation will be described.

CHAPTER 5

BLOOD VESSEL SEGMENTATION METHODOLOGY, RESULTS AND DISCUSSION

5.1 Overview

Retinal fundus images are used for diagnosing different diseases like arteriosclerosis, cardiovascular disease, stroke, glaucoma, diabetic retinopathy etc. Among these conditions, DR and glaucoma can result in vision loss. In fact these two are the leading causes of vision loss. This chapter describes the methodology, results and discussion of proposed blood vessel segmentation detection approach. In section 5.2.1, the materials used for training and testing the proposed blood vessel segmentation is presented. Similarly in section 5.2.2, the proposed blood vessel segmentation methodology is described. While the evaluation metrics for the blood vessel segmentation is presented in section 5.2.3. The results and discussion of the proposed blood vessel segmentation system are presented in section 5.3. The developed system was trained and tested using DRIVE dataset. The results at the output of a classifier are given in section 5.3.1. Results on test images are given in section 5.3.3. Discussion and comparison with state of the art methods is given in section 5.3.4. The chapter concludes with a summary provided in section 5.4.

5.2 Materials and Method for Blood Vessel Segmentation

5.2.1 Materials for Blood Vessel Segmentation

We evaluated the proposed blood vessels segmentation system using dataset called DRIVE [119]. This dataset consists of 40 color fundus images. The images were taken with three CCD camera having 45 degree field of view (FOV) and 768x584 pixels. Each pixel is represented by 24 bits (8 bits per color). These 40 images were further divided into two datasets: training dataset with 20 images and test dataset with 20 images. The dataset is accompanied by ground truths or the manually segmented blood vessels images and masks images. There are two independent sets of manual segmentations for test images called first manual segmentation and second manual segmentation. Most of the researchers use first manual segmentation to evaluate the performance of their algorithms. The masks images are about 540 pixels in diameter, representing the region of interest (ROI).

5.2.2 Method of Blood Vessel Segmentation

The proposed approach consists of three main steps, i.e. image preprocessing, feature extraction and pixel classification into vessels and non-vessels. The flow chart of the proposed system is shown in Figure 5.1 .

5.2.2.1 Image Preprocessing

As discussed in section 2.3 that retinal images contain noise as well as variations within and between the retinal images. Therefore, these images require generally preprocessing. The proposed system has blood vessels segmented in gray channel. Therefore, the RGB images were first converted to gray channel. In the gray channel, we used 3x3 median filter to remove salt and pepper noise. The blood vessels being red in color have low intensity in the gray channel while the background has the high intensity values. Hence, dot product of the gray channel with itself will improve the contrast of the blood vessels with the background. The major blood vessels are generally well contrasted while the fine vessels have mostly low contrast. To

homogenize the images, we calculated per pixel the contrast of the neighborhood in 5x5 array. This operation resulted in an image with a more homogenous background and very clear blood vessels.

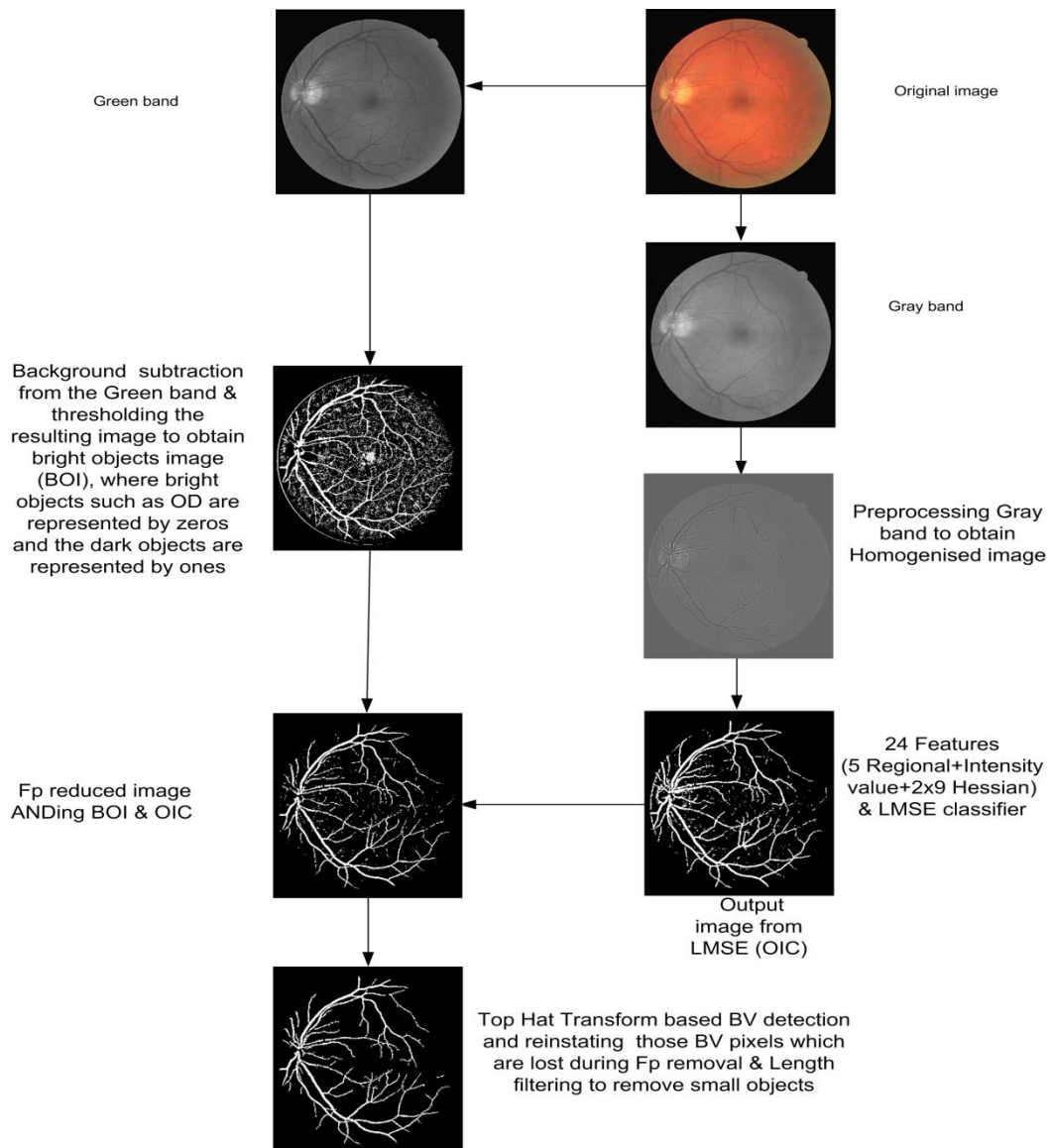


Figure 5.1: Flow chart of the proposed blood vessel segmentation system

5.2.2.2 Features Extraction

Feature extraction is one of the very important stages in blood vessel segmentation. Robust features are one of the main requirements for a good classification. Based on the preprocessed image, it could be seen that the blood vessel and background were well contrasted then. Therefore, regional statistical features similar to [134] in combination with Hessian features would be sufficient to classify the pixels into vessel and non-vessel.

a) Regional Features

We have utilized following six regional statistical features. Here I_H represents the homogenized image while $I_H(x,y)$ represents the current pixel.

1. Difference of the current pixel with the pixel in the region with the lowest intensity. Mathematically it can be written as:

$$F_{R1} = I_H(x, y) - \min_{(s,t) \in S_{x,y}^9} \{I_H(s, t)\} \quad (5.1)$$

2. Difference of the current pixel with the pixel in the region with the highest intensity. Mathematically it can be written as:

$$F_{R2} = \max_{(s,t) \in S_{x,y}^9} I_H(x, y) - I_H(x, y) \quad (5.2)$$

3. Current pixel minus mean of the surrounding. Mathematically it can be written as:

$$F_{R3} = I_H(x, y) - \text{mean}_{(s,t) \in S_{x,y}^9} \{I_H(s, t)\} \quad (5.3)$$

4. Standard deviation of the region. Mathematically it can be written as:

$$F_{R4} = \text{STD}_{(s,t) \in S_{x,y}^9} \{I_H(s, t)\} \quad (5.4)$$

5. Entropy of the region. Mathematically it can be written as:

$$F_{R5} = - \text{sum}(\text{P}_{\text{histcount}} \log_2(\text{P}_{\text{histcount}})) \quad (5.5)$$

where $\text{P}_{\text{histcount}}$ of 9x9 region.

6. Pixel intensity in the homogenized image. Mathematically it can be written as:

$$F_{R6} = I_H(x, y) \quad (5.6)$$

b) Hessian based Features

The Hessian matrix (or Hessian) is a square matrix. It is composed of second-order partial derivatives of multivariable scalar valued function. It can be used to capture the shape characteristics of objects [123]. These objects can be tubes, planes, blob surfaces etc. As discussed that Hessian matrix is symmetrical with real eigenvalues and orthogonal eigenvectors, these eigenvalues values can be used for the detection of different structures [124]. Hence they are used to detect elongated objects such as blood vessels. Due to the fact that blood vessel have different widths, we need to find the Hessian features on multiple scales. Witkin [135] introduced the formalism for the scale-space representation and Koenderink [136] developed it further. Based on this approach a family of smooth images $I(x, y; s)$ using the parameter s can be generated. These smooth images are obtained by convolving the image $I_0(x, y)$ with a Gaussian kernel $G(x, y; s)$ of size s .

$$I(x, y; s) = I_0(x, y) * G(x, y; s) \quad (5.7)$$

where $*$ represents the convolution and $G(x, y; s) = \frac{1}{2\pi s} e^{-(x^2+y^2)/2s}$

Using different values of s , we obtained different versions of the original image with some amount of blurring proportional to s . According to scale-space theory differentiation is equal to the convolution of the image with the derivative of the Gaussian kernel. Thus using scale space theory, we could find the partial derivatives of image at scale s using the following equations:

$$I_x(x, y, s) = I_0(x, y) * (G_x(x, y; s)) \quad (5.8)$$

$$I_{xx}(x, y, s) = I_0(x, y) * (G_{xx}(x, y; s)) \quad (5.9)$$

$$I_y(x, y, s) = I_0(x, y) * (G_y(x, y; s)) \quad (5.10)$$

$$I_{yy}(x, y, s) = I_0(x, y) * (G_{yy}(x, y; s)) \quad (5.11)$$

$$I_{xy}(x, y, s) = I_o(x, y) * (G_{xy}(x, y; s)) \quad (5.12)$$

Thus using equations 5.8 to 5.12, Hessian matrix was formed. In the context of blood vessel detection, second order information, the Hessian, has an intuitive justification. The second derivative of a Gaussian kernel at scale s generates a probe kernel that measures the contrast between the regions inside and outside the range $(-1,1)$ in the direction of the derivative, as shown in Figure 5.2, right: the second order ellipsoid describes the local principal directions of curvature.

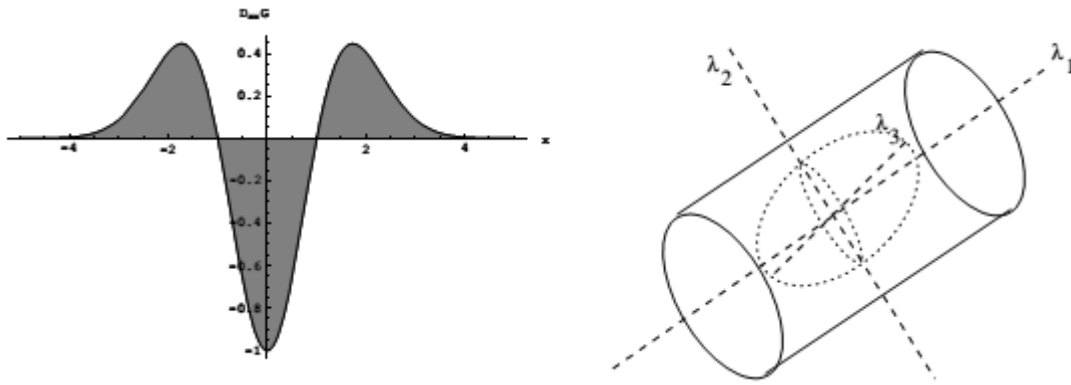


Figure 5.2: The second order derivative of a Gaussian kernel probes inside/outside contrast of the range $(-1,1)$, reproduced from [137]

Retinal vessel have different widths, therefore, Hessian features should be calculated at multiple scales. The Hessian features to be incorporated in the proposed algorithm are the eigen values (λ_1 and λ_2). Nine scales were used to accommodate all the widths of the blood vessels. Thus we have 24 features in total to describe the blood vessel. All these features were extracted from each pixel in the ROI and were normalized using equation 3.5. These features were then fed to a linear minimum squared error classifier (LMSE).

5.2.2.3 Pixel Classification

Since all the pixels in the retinal images belong to two classes vessels class (VC) and non-vessels class (NVC), thus we have a two-class problem. Based on features extracted, we needed to classify each pixel into VC or NVC. To perform this operation, we utilized the Linear Minimum Squared Error classifier (LMSE). LMSE has a very fast training process. In d -dimensional feature space, the linear classifiers are defined by linear decision function y as follows:

$$y(x) = w^T x + w_0 \quad (5.13)$$

In equation 3.36, x represents feature vector, w is the weight vector while w_0 denotes the threshold. The class is decided based on the value of the function y i.e. we have VC if $y(x) > 0$ and NVC if $y(x) \leq 0$. Equation 3.34 can also be written as:

$$y(x) = w'^T x' \quad (5.14)$$

where $w' \equiv [w^T \ w_0]^T$ and $x' \equiv [x^T \ 1]^T$

In the training phase, we try to find W such that it minimizes the sum of squared error criteria. For training the LMSE, we select samples of blood vessels and non-blood vessels from all the 20 images of training dataset. In testing phase we use the test dataset provided by DRIVE dataset.

5.2.2.4 Post processing

At the output of the classifier, the proposed system has a high sensitivity with lower specificity and accuracy. This is expected because the homogenized image is sensitive to variation in intensity. In the consequences of this sensitivity, there were a lot of false positives from the OD region of the retina. Also the bright lesions and circular boundary near the region of interest (ROI) in many of the images are contributing the false positives due to the same reason. Thus to improve the specificity, we needed post processing. To overcome the problem of false positives, we utilized the background estimation, mathematical morphology and length filtering.

1. Background Estimation

Blood vessels in green band have low intensity values compared to optic disc and bright lesions. Hence based on intensity, we divided all the pixels in fundus image into dark and non-dark objects and we called pixels that belong to dark objects as foreground pixels and the rest into background pixels. To estimate the background, green band has been selected and the highest 17 % pixels were considered as background. And all those pixels which were from background were removed. Thus in this way we removed most of the false positives. The image after this step is denoted by $\text{Img}_{\text{FP_removed}}$.

2. Mathematical Morphology Based

As stated in the previous section, using the background foreground division based on intensity removed most of the false positives but many of the true vessel pixels were also lost. Hence there would be a decrease in the sensitivity of the proposed system. Thus to regain those vessel pixel which were unintentionally lost in background foreground division, we used a mathematical morphological technique called Top Hat Transform (THT). Mathematical morphology has been used for detection of different objects in an image. The top-hat transformation of a grayscale image I is defined as I minus its opening (see appendix C). Mathematically it can be described as:

$$THT = I - (I \circ B) \quad (5.15)$$

where $(I \circ B)$ represent the opening of I with structuring element B . Based on above equation, it can be said that the desired detail can be obtained by subtracting the opened image from the original image. The opened image will remove all the small objects from the image while subtracting the opened image from the image results in leaving only those small objects. Hence using top hat transform we can extract small or narrow, bright or dark features in image. Thus by selecting a proper structuring element, we can use top hat transform to extract objects of interest.

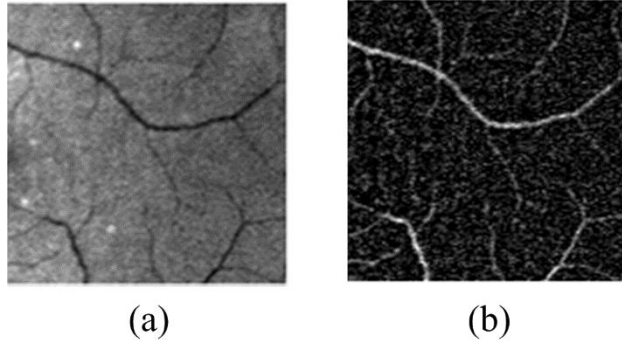


Figure 5.3: Left original image, right top hat transformed image

Figure 5.3 depicts an example of top hat transformed image where image on right is obtained by applying top hat transform with linear structuring element of length 10 pixels on left image. In case of blood vessel, we used linear structuring element with length of 10 pixels and orientations in the range of 0:180 with increment of 10 and applied the top hat transform. Before application of top hat transform the iterative region growing of the ROI has been implemented as in [94] to avoid false positives due to border of the camera's aperture. Thus summing the top hats in all the orientations results in enhancement of all the vessels regardless of their directions, sizes, and regions (even in the low local contrast regions). This enhanced image is binarized to get vessel image denoted by Img_{THt} . The image Img_{THt} is multiplied with the image obtained in previous section 5.2.2.4 1, to obtain Img_{BV_Rconst} . The image Img_{BV_Rconst} contains all those pixels which are from blood vessels and those removed during the false positives removal, however it also contains some of the false positives. The image Img_{BV_Rconst} is added to image $Img_{FP_removed}$ to obtain Img_{Mod} .

3. Length/Area Filtering

The image obtained in the previous section was length filtered to obtain the final image blood vessel image denoted by Img_{Final_BV} . Thus in this step we removed the small objects which were less than 50 pixels, and obtained the final blood vessel image.

5.2.3 Evaluation Metrics for Blood Vessel Segmentation

The performance of the automatic blood vessel segmentation system can be evaluated using different metrics. These are sensitivity or True Positive Rate (TPR), False Positive Rate (FPR) (for TPR and FPR see appendix C), Accuracy (ACC), Area under the Receiver Operating Characteristic (ROC) Curve (AUC), Matthews Correlation Coefficient (MCC) and Connectivity (C), Area (A), Length (L). If a pixel belongs to blood vessel and the system detects it as blood vessel then it is said to be true positive (T_P). While if mistakenly the system detects non-vessel pixel as blood vessel, in such case it is called False Positive (F_P). Similarly if the pixel belongs to non-vessel and the system detects it as non-vessel, then it is called True Negative (T_N). If mistakenly the system recognizes the vessels pixel as non-vessel, in such case it is called false negative (F_N). ACC can be mathematically described as:

$$\text{Sensitivity or TPR} = \frac{TP}{TP + FN} \quad (5.16)$$

$$ACC = \frac{T_P + T_N}{T_P + T_N + F_P + F_N} \quad (5.17)$$

An ideal system should have sensitivity/TPR=1, ACC=1 and Specificity=1. Ideally FPR should be zero. The ROC curve is plot of TPR vs FPR. ROC curve can be obtained by changing the threshold. When threshold is kept very high, we have very few false positives but the TPR is also very low. Reducing the threshold will improve the TPR at the cost of more false positives. Thus using a span of thresholds, we can obtain a set of points which can be plotted to obtain a curve called ROC. Now using this ROC we can find AUC. Thus the simplest way to calculate the AUC is by using trapezoidal integration. The AUC metric is frequently reported in literature. In case of an ideal system, the value of AUC = 1, while most of the automated segmentation systems have AUC values falling in between 0 and 1. MCC measures the quality of a binary classification. It was introduced by [138]. It is defined as:

$$MCC = \frac{TP \times TN - FP \times FN}{\sqrt{(TP + FP)(TP + FN)(TN + FP)(TN + FN)}} \quad (5.18)$$

The maximum value MCC can have is 1 while the minimum can be -1. MCC=1, represent the ideal case and the detection of the system is perfect while -1 means total

disagreement between detected values and the ground truth. This measurement is also suitable for those applications in which the samples in one class are far more than the other class. A different approach for the evaluation of blood vessel segmentation was proposed by Gegúndez-Arias et al. [139]. Instead of pixel by pixel comparison, connectivity, area and length of the segmented image are compared with ground truth. The function is given by:

$$f(C, A, L) = C \times A \times L \quad (5.19)$$

where C represents connectivity, A is area while L represents the length. Let S represents the segmentation to be evaluated and ground truth image is S_G . The C which represents the assessment of the fragmentation degree between S and S_G and is given by:

$$C(S, S_G) = 1 - \min \left(1, \frac{|\#c(S_G) - \#c(S)|}{\#(S_G)} \right) \quad (5.20)$$

The evaluation of the degree of overlapping areas between S and S_G is denoted by A and is given by:

$$A(S, S_G) = \frac{\#((\delta_\alpha(S) \cap S_G) \cup (S \cap \delta_\alpha(S_G)))}{\#(S \cup S_G)} \quad (5.21)$$

Function δ_α is a morphological dilation with a disc SE having α pixels in radius. L measures the degree of coincidence between segmented image S and ground truth image S_G in terms of total length and is given by:

$$L(S, S_G) = \frac{\#((\varphi(S) \cap \delta_\beta(S_G)) \cup (\delta_\beta(S) \cap \varphi(S_G)))}{\#(\varphi(S) \cup \varphi(S_G))} \quad (5.22)$$

where φ and δ_β are respectively a and morphological dilation with β pixels disc. α and β values have been set to 2. More details can be found in [139].

5.3 Results and discussion of Blood Vessel Segmentation

We have used a total of 4000 pixels of vessel and non-vessel class from the DRIVE dataset to train the LMSE classifier. These pixels were selected randomly from the 20 images of training dataset provided by the DRIVE. To cope with the varying width of blood vessel, we have used the Hessian features at nine scales.

5.3.1 Preprocessing

Blood vessels and other red lesions are dark in green and gray bands. As stated earlier that color fundus images suffer from low and varying contrast, we have preprocessed the images in gray band to obtain a homogenized image as shown in Figure 5.4(d). Using local features in conjunction with Hessian features is found to be robust enough for detection of the blood vessels.

5.3.2 Pixel Classification

In the proposed system, a LMSE classifier was trained using 24 features and randomly selected 4000 pixels of vessels and non-vessels from 20 training images of DRIVE dataset. LMSE classifier being simple is quite fast in training and testing. The proposed system was tested on test dataset.

5.3.2.1 Results at the Output of Classifier

At the output of classifier, the proposed system had a high sensitivity and most of the blood vessels were detected. But overall accuracy of the system was not very good. The false positives at this stage were mostly from the boundary region of ROI, edges of optic disc and over segmented blood vessels. We believe that false positives from boundary of ROI region and on the edges of optic disc region were introduced in image homogenization step. The average sensitivity and accuracy were 0.87 and 0.92 respectively as we have used only 4000 randomly selected vessel and non-vessel pixels, which is a very small fraction of the total pixels in the 20 training images (less than one percent of the total pixels in ROI) of the DRIVE training dataset.

5.3.2.2 Post Processing Results

As described in previous section, the system has high sensitivity but not very good specificity and accuracy.

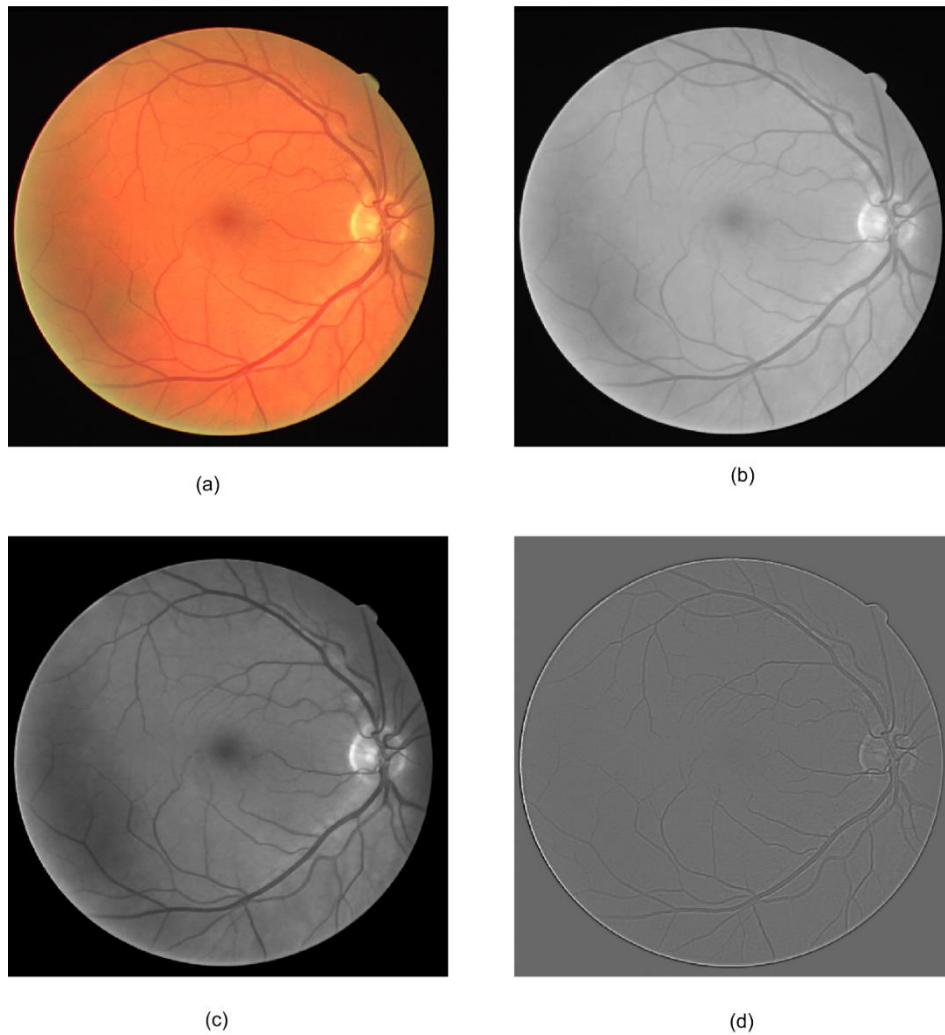


Figure 5.4: a) color fundus image (b) gray channel image (c) enhanced gray channel (d) homogenized background image with vessels

It has been observed that most of the false positives were from the circular boundary of the ROI. Many of the false positives were from optic disc region and some others from the bright regions in the image. Many of the false positives are from bright lesions and red lesions. Another group of false positives is the over segmented blood vessels. Therefore, to improve specificity while maintaining the sensitivity a two steps post processing strategy was designed.

5.3.2.3 Results after Background Estimation Post Processing

As discussed in section 5.2.2.4, all pixels in the image are either foreground (blood vessel pixels) or background (non-blood vessel pixels). Blood vessel pixels being red in color have low intensity values and can be separated from other objects based on intensity value. In this way most of the false positives are removed. These removed objects were from the bright regions in the image, bright lesions, optic disc region, circular boundary region of the ROI and in some cases the segments of the blood vessels also. Thus most of the false positives were removed. However few of the blood vessels were also removed. In this step although there was a decrease in sensitivity, there was more improvement in specificity which resulted in overall improvement in accuracy of the proposed system.

5.3.2.4 Results after Mathematical Morphology Based Post Processing

This step was required to maintain the sensitivity of the developed system at good level. In the previous step most of the false positives were removed but some of the vessel pixels were also missed in the process. Therefore, to reinstate those vessel pixels we had utilized mathematical morphology based approach. As discussed in section 5.2.2.4 2, that we had also detected blood vessels in green band using top hat transform. The top hat transform was effective in the sense that it did not detect the false positives in the optic disc region and region along the ROI of the fundus images. Thus it overcame the limitations in homogenized image. We compared all those pixels which were removed in the background estimated image as false positives with the blood vessel image obtained using top hat transform. Thus all those pixels were reinstated according to top hat transform based blood vessel image. In this way, the sensitivity of the proposed system was improved.

5.3.3 Results on the Test Images

Image by image results on test dataset of the developed system are presented in Table 5.1. The best accuracy achieved is 0.9618 on image 19 while the worst case accuracy of 0.9369 was achieved. The average accuracy achieved is 0.9479. Figure 5.5 depicts the images achieving the best sensitivity (top row) and the best specificity (bottom row),

shown in column on the left are the color images while column on right are the segmented blood vessel. These results are based on first manual segmentation.

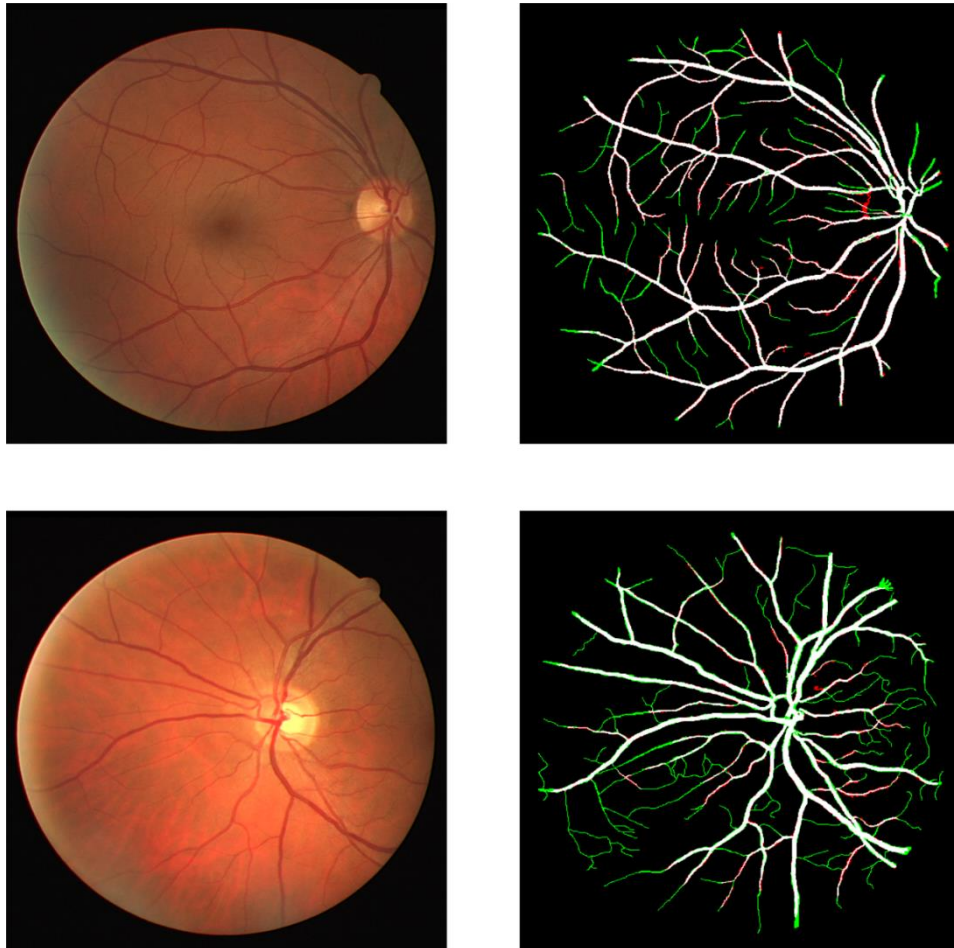


Figure 5.5: Left column color images while right column segmented vessel. Shown in top row is image with the best sensitivity and bottom row image with the best specificity, green pixel are the F_N and red are the F_P

While the results for the proposed system using second manual segmentation are presented in Table 5.2. Based on second manual segmentation the highest accuracy achieved is 0.9629 (image 5) while the lowest accuracy achieved is 0.9401 (image 13). Performance comparison of the proposed method with existing works is presented in Table 5.3. It can be noticed that the proposed method achieves similar accuracy as the state of the art algorithms. However, in terms of false positive rate the proposed system achieves lower false positive rate than the second observer.

Table 5.1: Image by image results of the developed system on test dataset based on first manual segmentation

Image No	Accuracy	Sensitivity	Specificity	MCC
01	0.9479	0.7760	0.9738	0.7667

02	0.9513	0.7590	0.9852	0.7994
03	0.9370	0.6929	0.97862	0.7311
04	0.9490	0.6833	0.9899	0.7633
05	0.9480	0.6903	0.9884	0.7625
06	0.9408	0.6803	0.9836	0.7386
07	0.9458	0.6816	0.9862	0.7470
08	0.9405	0.62783	0.9854	0.7045
09	0.9499	0.6973	0.9835	0.7425
10	0.9496	0.7100	0.9821	0.7464
11	0.9458	0.6936	0.9833	0.7435
12	0.9480	0.7338	0.9787	0.7519
13	0.9403	0.6701	0.9849	0.7362
14	0.9489	0.7782	0.9717	0.7534
15	0.9539	0.7300	0.97977	0.7428
16	0.9471	0.7156	0.9820	0.7540
17	0.9473	0.7139	0.9800	0.7432
18	0.9507	0.7697	0.9742	0.7543
19	0.9618	0.8163	0.9817	0.816
20	0.9540	0.7891	0.9737	0.7598
Average	0.9479	0.7205	0.9814	0.7529

Bold in column 2 are the worst, the best, and average accuracy respectively while bold in bottom row represent the average values.

Table 5.2: Image by image results of the developed system on test dataset based on second manual segmentation

Image No	Accuracy	Sensitivity	Specificity	MCC
01	0.9520	0.7973	0.9748	0.7828
02	0.9576	0.7841	0.9877	0.8243
03	0.9485	0.7603	0.9766	0.7649
04	0.9548	0.7153	0.9897	0.7830
05	0.9629	0.7825	0.9870	0.8137
06	0.9457	0.7064	0.9831	0.7531
07	0.9597	0.7984	0.9784	0.7819
08	0.9525	0.7262	0.9769	0.7231

09	0.9514	0.704	0.9841	0.7498
10	0.9592	0.7868	0.9792	0.7780
11	0.9567	0.7538	0.9845	0.7860
12	0.9560	0.7879	0.9787	0.7843
13	0.9401	0.6636	0.9876	0.7426
14	0.9537	0.8226	0.9698	0.7695
15	0.9505	0.7058	0.9802	0.7303
16	0.9578	0.7717	0.9840	0.7965
17	0.9577	0.7922	0.9777	0.7782
18	0.956	0.7535	0.9875	0.8007
19	0.9509	0.7265	0.9886	0.7890
20	0.9478	0.7063	0.9852	0.760904
Average	0.9536	0.7523	0.9821	0.7747

Bold in column 2 are the best, the worst and average accuracy respectively, while bold in bottom row represent the average values.

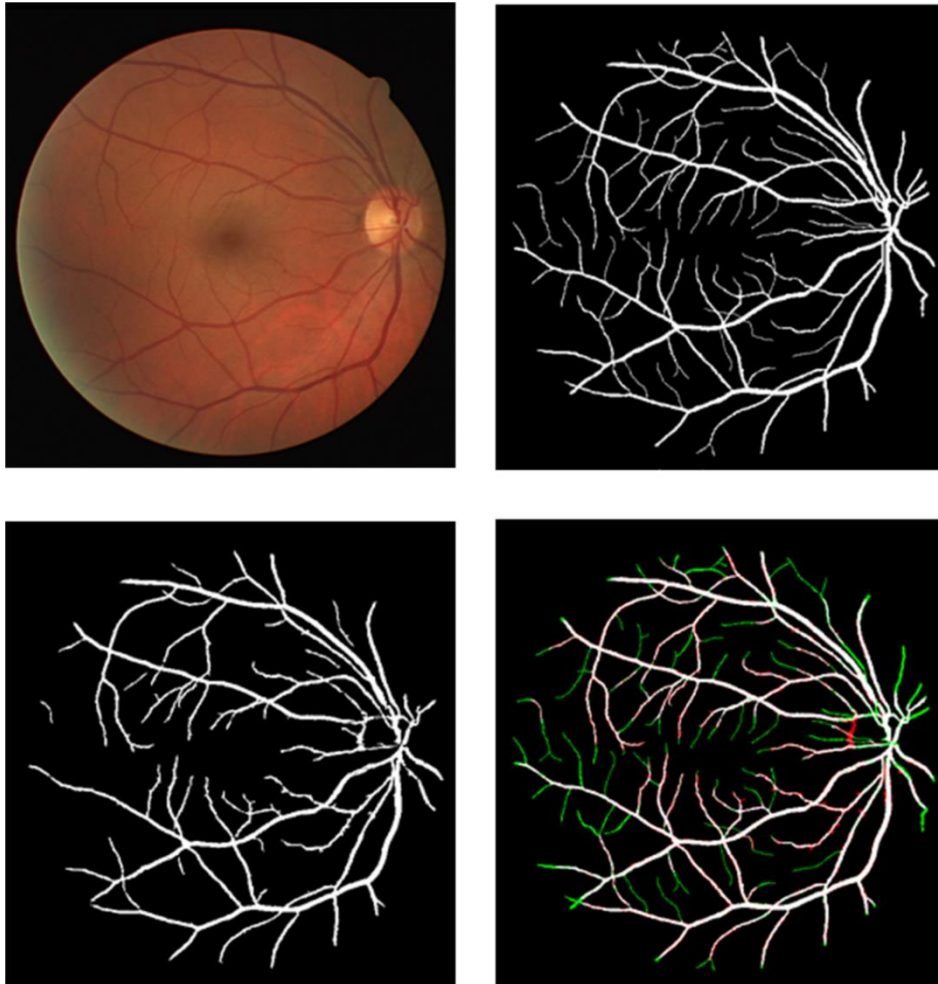


Figure 5.6: Image achieving the best accuracy. Top row: left color image, right ground truth. Bottom row: left segmented BV while on the right, green pixel are the F_N and red are the F_P

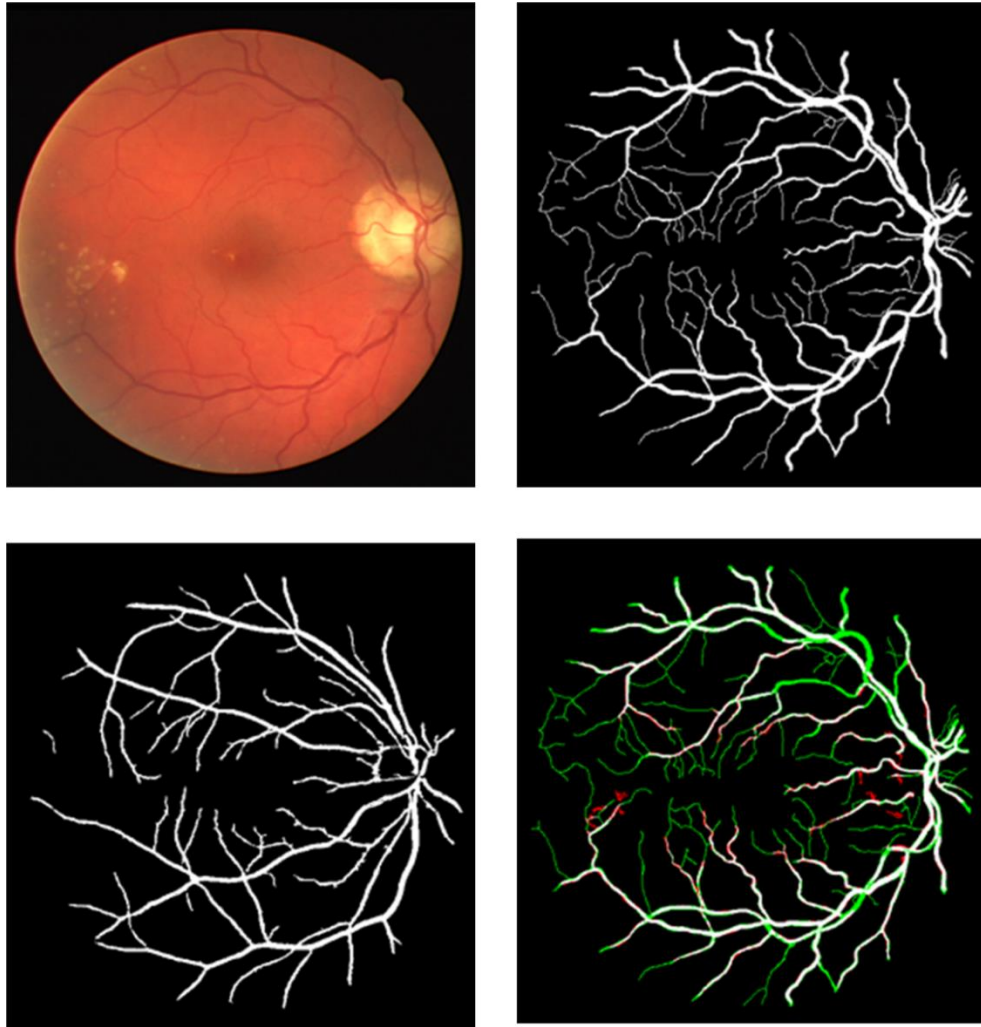


Figure 5.7: Image achieving the worst accuracy. Top row: left color image and right ground truth. Bottom row: Left segmented BV, right, green pixel represent the F_N and red are the F_P

5.3.4 Discussion and Comparison

The images with the best and worst case accuracies are shown in Figure 5.6 and Figure 5.7 respectively. Here white color are T_P , red are F_P and green are F_N . Based on width of the blood vessel, we can divide them into three groups: big/thick vessel (width > 8 pixels), medium vessel (3 < width < 9 pixels) and very fine vessel (width < 3 pixels). It can be observed that all the big/thick vessels detected by the proposed system are very accurate with negligible number of F_P or F_N pixels. It can be noticed that even in the worst case, the proposed system is able to accurately detect the width of thick blood vessels. The system in this case has however over-estimated the medium blood vessels. Thus it can be said that the proposed system has the ability to accurately detect the widths of the thick blood vessels. For the second case of blood vessel, which we call

medium vessel, the proposed system has lower accuracy in comparison with thick blood vessel. This lower accuracy is due to the over-estimation of blood vessels in many cases while in some cases as a result of missing the blood vessels. Thus in case of medium width blood vessel, we have many F_P but fewer F_N , whereas for the case of fine vessel, the developed system is unable to detect many of these resulting in very low accuracy in comparison with the first two cases.

The F_P in the developed system can be categorized into three categories

1. Those on the edges of the medium width blood vessel
2. The edges of the Optic disc region
3. Lesions (bright/dark)

Table 5.3 contains the comparison results of the proposed method with other methods. The average sensitivity of the proposed system is found to be with average accuracy of 0.9479, while the average FPR and MCC values of the proposed system are 0.0186 and 0.7529 respectively. Based on the MCC values in Table 5.3, it is clear that the proposed system achieved the best value among all the reported studies and it is only second to human observer. In terms of the specificity, it can be said that the proposed system has very -low false positive rate with comparative sensitivity.

On DRIVE test dataset, segmented vessel images of Soares et al. [94] available on (<https://sourceforge.net/projects/retinal/>) were compared with those segmented using the proposed method. It is observed that the two systems perform similar in detecting the fine vessels. However, we see that the proposed system has slightly better overall average accuracy (0.9466 vs. 0.9479). The Soares system performed better in detecting medium blood vessels. Also in terms of FPR, the proposed system has better FPR with average of 0.0186 while Soares system has average FPR of 0.0212. In some of the cases, they are not able to differentiate between two very closely positioned ve-

Table 5.3: Comparative performance of the proposed method with existing works

Methods	ACC	TPR	FPR	AUC	CAL	MCC
2nd Observer	0.9473	0.7761	0.0275	-	0.849	0.760

Marin et al. [134] 2011	0.9452	0.7067	0.0275	0.959	-	-
Soares et al. [94] 2006	0.9466	0.7283	0.0212	0.961	0.751	0.749
Niemeijer et al. [140] 2004	0.9416	0.6898	0.0304	0.929	0.686	0.718
Staal et al. [119] 2004	0.9442	0.6780	0.0170	0.952	0.716	0.732
Fraz et al. [141] 2012	0.9480	0.7406	0.0193	0.975	-	-
Jianget al. [142] 2003	0.9212	-	-	0.933	-	-
Mendonça. [101] 2006	0.9463	0.7315	0.0219	-	-	-
Zana et al. [100] 2001	0.9377				0.640	0.724
Martinez-Pere. [143] 1999	0.9344	0.7246	0.0345	-	0.578	0.662
Al-diri et al. [144] 2009	0.9258	-	-	-	-	-
Zhang et al. [89] 2010	0.9382	0.712	0.0276	0.788	-	-
Li et al. [145] 2012	0.9310	0.6455	0.0337	-	-	-
Bankhead et al. [97] 2012	0.9371	0.7027	0.0283	0.782	0.625	0.706
Yin et al. [146] 2014	0.9475	0.7556	0.0344	-	-	-
Zhao et al. [115] 2015	0.953	0.744	0.0220	0.861	-	-
Oliveira et al. [114] 2016 Weighted mean using ORSF	0.9356	0.7988	0.0475	0.912	0.702	0.694
Weighted mean using FCM	0.9402	0.9106	0.0569	0.912	0.553	0.704
Median ranking	0.9464	0.8644	0.0444	0.951	0.683	0.743
Proposed Method	0.9479	0.7205	0.0186	0.942	0.67	0.753

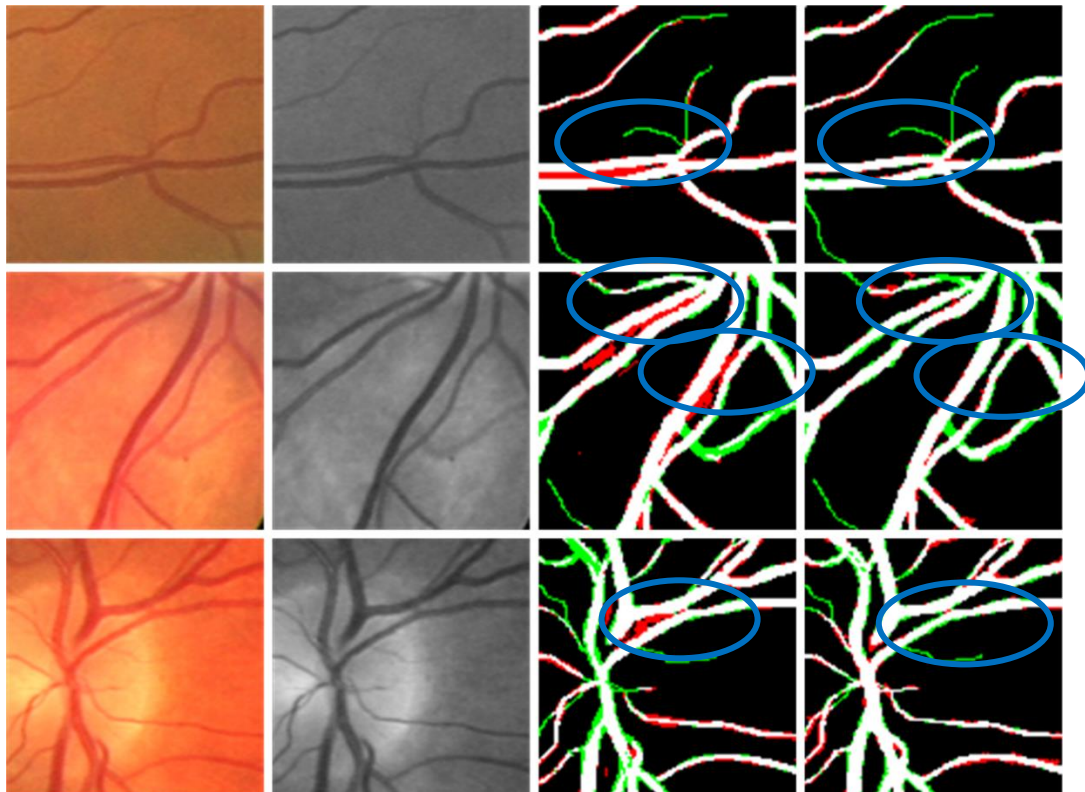


Figure 5.8: 1st and 2nd column are respectively colored and green patches of the image, 3rd and 4th column patches represents the vessel detected using Gabor wavelet method and the proposed method respectively

-ssel and their system detected them as one lump vessel while the proposed system is able to differentiate the very close blood vessels. Few of such instances are shown in Figure 5.8, green pixels represent the missed vessel pixels while red represent the false positives and white are the true positives. Encircled in blue are the examples where two vessels are mistakenly merged.

While working on MA detection, we observed that most of the false positives are from blood vessels. Moreover it has been noticed that due to non-uniform illumination, low and varying contrast, the overall sensitivity at low FPR ($FPR \leq 0.03$) in vessel segmentation has been affected severely. Thus to overcome the stated problems which are inherent in the color fundus images, we proposed a new method based on image homogenization. Hessian and regional features are extracted from the homogenized image to segment the blood vessel. It was believed that the vessel segmented in such a way might achieve a very good sensitivity. Although the developed blood vessel segmentation system has very good sensitivity (0.7205 for DRIVE dataset) but failing in the case of fine vessels. As such, we did not apply the developed blood vessel segmentation system for removing the blood vessel in automated MA detection[85] because it has poor sensitivity in detecting fine blood vessel. In addition, in MA detection system, those F_P which are hard to remove are from the fine vessel. Therefore, the proposed vessel segmentation will have similar performance as the Gabor wavelet used in automated MA detection system of Shah et al. [85].

5.4 Summary

In this chapter, methodology, results and discussion about blood vessel segmentation system have been presented. For blood vessel segmentation, to overcome the problem of low and varying contrast, images were homogenized. However the procedure is sensitive to variation in intensity, thus produced many false positives especially on the boundary of ROI and near the optic disc. To overcome this shortcoming, it has been proposed to use the mathematical morphology in parallel so that the developed blood vessel segmentation system have false positive rate similar to state of the art methods but with better sensitivity. Using LMSE classifier and Hessian features at multiple scale and regional features, the proposed algorithm achieves sensitivity of 0.77 with false

positive rate of 0.0283 and accuracy of 0.9459. The sensitivity and FPR is similar to human observer. But at a comparable accuracy of 0.9479, we have sensitivity of 0.7205 with 0.0186 average FPPI. Thus it proves the hypothesis that addressing the issue of low and varying contrast and by using multiscale feature based technique can improve automated BV segmentation. In next chapter, conclusion and future work will be described.

CHAPTER 6

CONCLUSION AND FUTURE WORK

6.1 Overview

This chapter describes the summary of all the work presented in this thesis. In section 6.2, conclusion of MA detection system is presented while in section 6.3 conclusion about the blood vessel segmentation system is presented. Section 6.4 discusses about the future work.

6.2 Conclusion of the Microaneurysms Detection System

This thesis aims to design a tool for diagnosing diabetic retinopathy. Microaneurysm (MA), one of the earliest signs of DR, is important to be detected not only for screening purposes but also for monitoring the progression of DR. Thus MA detection is of paramount importance. Therefore, our target was to design a system which can have high sensitivity while keeping the comparable average false positives per image. Therefore, the two main parameters which are color and shape of the MA are utilized in effective way to optimize the overall sensitivity of the developed system. In any automated MA detection system, most of the false positives come from background and blood. Hence we have specialized stages for removal of each type of false positives. To remove false positives due to background, we have estimated the background and using only two parameters we could remove most of the false positives from the background. Also the color of MAs is very important for distinguishing between MA and false positives due to non-red objects. As we selected the initial candidates based on local thresholding, we have many false positives due to none-red objects also. So using color features is very effective in removing non-red objects. For removal of blood vessel and

other elongated objects, the two stage strategy is, by using 2-D Gabor wavelet and Hessian based features. The blood vessels could have been removed using Gabor wavelet only but many of the MAs near the blood vessel were also removed resulting in unintentional loss of MAs. We proposed to remove the blood vessel in two steps. By keeping the higher thresholds in blood vessel segmentation helps in keeping MAs near the blood vessel intact. Thus many of the MAs near the blood vessel were preserved, while removing the blood vessels. The consequences of the of higher threshold results in many broken vessel parts as false positives. To remove those parts and other elongated objects, Hessian features have been utilized. In this way we are able to detect those MAs which are near the blood vessels and would be otherwise removed as part of blood vessel. Further false positives were removed in the Curvelet transform stage. In Curvelet transform stage, aspect ratio, circulatory, mean energy, and standard deviation of energy were used to differentiate between MA and non-MAs. As hypothesized in chapter one, we could keep the maximum number of the microaneurysms if the false positives were addressed by category and Curvelet transform was used. The results proved that the hypothesis was true.

6.3 Conclusion of the Blood Vessel Detection System

Ocular manifestations of different medical conditions like arteriosclerosis, cardiovascular disease, stroke, glaucoma, DR hyper tension etc. are important in confirming the diagnosis. Also the accuracy of any automated DR detection system can be improved if blood vessels were properly detected. Therefore, automated detection and analysis of retinal blood vessels is an extremely important task. The second aim of this thesis is to accurately detect and segment blood vessels. While working on MA detection, we realized the fact that it is very important to get rid of low and varying contrast which is inherent in color fundus images. Therefore, we have designed a preprocessing strategy to homogenize the images. We used gray channel in which red objects such as blood vessels and red lesions have low intensity values. In the first step, we multiplied the gray band image with itself. The multiplication of gray band image with itself will lower intensity values for dark objects, which results in improved contrast for blood vessel with background. While in second step of preprocessing, we calculated the contrast image using 5x5 window on contrast enhanced image. The

homogenized image thus obtained has almost uniform contrast. However, since this operation is dependent on variation in intensity, the homogenized image contains generally false edges near the boundary of optic disc and around the round ROI of the fundus images and the areas with change in intensity, no matter these are bright or dark areas. Thus regional and Hessian features and very simple classifier (LMSE) were utilized in combination. We achieved very good sensitivity but with accuracy not as good as expected. Many false positives were there. Such a post processing scheme was designed to keep maximum number of the vessel pixels and remove most of false positive. Thus we achieved comparable accuracy with the state of the art methods, but using not as many features and a simple classifier. Thus it proves the hypothesis that addressing the issue of low and varying contrast and by using multiscale feature based technique can improve automated BV segmentation.

6.4 Future Work

This section presents some of the limitations in the algorithms designed for the detection of MA and blood vessel along with guidelines for future work.

6.4.1 MA Detection

We observed that the main sources/contributors of FPs in automated MA detection such as proposed one are image background and BVs while hemorrhages are the third category of FPs although with fewer in numbers. The proposed system has a high sensitivity and is able to detect MAs near the BVs. However the number of false positive per image was still high. Therefore, improvement can made in the reduction of false positives. Also the system is not able to differentiate between hemorrhages and MAs. One more area to be investigated is the removal of fine vessels. The analysis of designed MA detection on other datasets such as DIARETDB1 etc should be explored. The designed MA detection is based on rule-based classifier. One of the possible future works will be the implementation of supervised classifier such as Support Vector Machine (SVM) or Neural Network (NN). Other possible approach to improve the sensitivity and specificity of the MA detection system is the utilization of multispectral imaging (MSI) approach. Applications of MSI have shown promising results in

different areas of biomedical image analysis. Nowadays deep learning is getting very popular due to its outstanding performance in computer vision and image analysis tasks[147]. Thus it is believed that utilization of deep learning can improve the sensitivity of the automated MA detection system and it may also result in reduction of false positives.

6.4.2 Blood Vessel Segmentation

The proposed system is able to detect the big and medium vessels but most of the fine vessels are missed. Also in the case of medium vessel, many of these vessels were over estimated. Thus there is room for improvement both in sensitivity and specificity which will ultimately result in better accuracy. The proposed system for blood vessel segmentation is very accurate at detecting the width of blood vessel. Thus this system can be tested for the datasets where width of the vessel detected are measured for diagnosis of different medical conditions. The other direction for future work could be the hierarchical system for high sensitivity in which medium and big vessels are detected using the designed system and some mechanism for fine vessels detection could be developed and results are combined to get highly sensitive system. One other direction will be the utilization of some high performance classifier such as SVM/NN.

REFERENCES

- [1] G. Hasler, W. C. Drevets, H. K. Manji, and D. S. Charney, "Discovering endophenotypes for major depression," *Neuropsychopharmacology*, vol. 29, pp. 1765-1781, 2004.
- [2] H. Kolb, "<http://webvision.med.utah.edu/book/part-i-foundations/gross-anatomy-of-the-eye> accessed on 2-6-2016."
- [3] C. Garhart and V. Lakshminarayanan, "Anatomy of the Eye," in *Handbook of visual display technology*, ed: Springer, 2012, pp. 73-83.
- [4] N. Yusoff, W. Y. Low, and C.-H. Yip, "Psychometric properties of the Malay Version of the hospital anxiety and depression scale: A study of husbands of breast cancer patients in Kuala Lumpur, Malaysia," *Asian Pacific Journal of Cancer Prevention*, vol. 12, pp. 915-917, 2011.
- [5] M. D. Abramoff, M. K. Garvin, and M. Sonka, "Retinal imaging and image analysis," *IEEE reviews in biomedical engineering*, vol. 3, pp. 169-208, 2010.
- [6] B. M. Ege, O. K. Hejlesen, O. V. Larsen, K. Møller, B. Jennings, D. Kerr, *et al.*, "Screening for diabetic retinopathy using computer based image analysis and statistical classification," *Computer methods and programs in biomedicine*, vol. 62, pp. 165-175, 2000.
- [7] O. Faust, R. Acharya, E. Y.-K. Ng, K.-H. Ng, and J. S. Suri, "Algorithms for the automated detection of diabetic retinopathy using digital fundus images: a review," *Journal of medical systems*, vol. 36, pp. 145-157, 2012.
- [8] H. Nema and N. Nema, *Textbook of ophthalmology*: JP Medical Ltd, 2011.
- [9] A. Fryczkowski, R. Chambers, E. Craig, J. Walker, and F. Davidorf, "Scanning electron microscopic study of microaneurysms in the diabetic retina," *Annals of ophthalmology*, vol. 23, pp. 130-136, 1991.
- [10] T. Walter, P. Massin, A. Erginay, R. Ordonez, C. Jeulin, and J.-C. Klein, "Automatic detection of microaneurysms in color fundus images," *Medical image analysis*, vol. 11, pp. 555-566, 2007.
- [11] T. Walter and J.-C. Klein, "Automatic detection of microaneurysms in color fundus images of the human retina by means of the bounding box closing," in *Medical Data Analysis*, ed: Springer, 2002, pp. 210-220.

- [12] D. S. Fong, L. Aiello, T. W. Gardner, G. L. King, G. Blankenship, J. D. Cavallerano, *et al.*, "Retinopathy in diabetes," *Diabetes care*, vol. 27, pp. s84-s87, 2004.
- [13] B. Dupas, T. Walter, A. Erginay, R. Ordonez, N. Deb-Joardar, P. Gain, *et al.*, "Evaluation of automated fundus photograph analysis algorithms for detecting microaneurysms, haemorrhages and exudates, and of a computer-assisted diagnostic system for grading diabetic retinopathy," *Diabetes & metabolism*, vol. 36, pp. 213-220, 2010.
- [14] K. M. Adal, D. Sidibé, S. Ali, E. Chaum, T. P. Karnowski, and F. Mériaudeau, "Automated detection of microaneurysms using scale-adapted blob analysis and semi-supervised learning," *Computer methods and programs in biomedicine*, vol. 114, pp. 1-10, 2014.
- [15] I. Lazar, A. Hajdu, and R. J. Quareshi, "Retinal microaneurysm detection based on intensity profile analysis," in *8th International Conference on Applied Informatics*, 2010.
- [16] I. Lazar and A. Hajdu, "Retinal microaneurysm detection through local rotating cross-section profile analysis," *Medical Imaging, IEEE Transactions on*, vol. 32, pp. 400-407, 2013.
- [17] B. Zhang, X. Wu, J. You, Q. Li, and F. Karray, "Detection of microaneurysms using multi-scale correlation coefficients," *Pattern Recognition*, vol. 43, pp. 2237-2248, 2010.
- [18] S. Abdelazeem, "Micro-aneurysm detection using vessels removal and circular hough transform," in *Radio Science Conference, 2002.(NRSC 2002). Proceedings of the Nineteenth National*, 2002, pp. 421-426.
- [19] J. Ma and G. Plonka, "The curvelet transform," *IEEE signal processing magazine*, vol. 27, pp. 118-133, 2010.
- [20] B. A. Olshausen and D. J. Field, "Emergence of simple-cell receptive field properties by learning a sparse code for natural images," *Nature*, vol. 381, p. 607, 1996.
- [21] "wiki https://en.wikipedia.org/wiki/Fundus_photography/ accessed on 1-6-2016."
- [22] J. D. M. Gass, R. J. Sever, D. Sparks, and J. Goren, "A combined technique of fluorescein funduscopy and angiography of the eye," *Archives of Ophthalmology*, vol. 78, pp. 455-461, 1967.

- [23] A. Agarwal, *Fundus fluorescein and indocyanine green angiography: a textbook and atlas*: SLACK Incorporated, 2007.
- [24] K. A. Kwiterovich, M. G. Maguire, R. P. Murphy, A. P. Schachat, N. M. Bressler, S. B. Bressler, *et al.*, "Frequency of adverse systemic reactions after fluorescein angiography: results of a prospective study," *Ophthalmology*, vol. 98, pp. 1139-1142, 1991.
- [25] V. Fineschi, G. Monasterolo, R. Rosi, and E. Turillazzi, "Fatal anaphylactic shock during a fluorescein angiography," *Forensic science international*, vol. 100, pp. 137-142, 1999.
- [26] D. A. Salz and A. J. Witkin, "Imaging in diabetic retinopathy," *Middle East African journal of ophthalmology*, vol. 22, p. 145, 2015.
- [27] M. Witmer, M. Cho, G. Favarone, R. P. Chan, D. D'Amico, and S. Kiss, "Ultra-wide-field autofluorescence imaging in non-traumatic rhegmatogenous retinal detachment," *Eye*, vol. 26, pp. 1209-1216, 2012.
- [28] M. E. Tyler, "Stereo fundus photography: Principles and technique," *J Ophthalmic Photogr*, vol. 18, pp. 68-89, 1996.
- [29] D. J. Coleman, F. L. Lizzi, and R. L. Jack, *Ultrasonography of the Eye and Orbit*: Lea & Febiger Philadelphia, 1977.
- [30] D. McLEOD and M. Restori, "Ultrasonic examination in severe diabetic eye disease," *British Journal of ophthalmology*, vol. 63, pp. 533-538, 1979.
- [31] D. Huang, E. A. Swanson, C. P. Lin, J. S. Schuman, W. G. Stinson, W. Chang, *et al.*, "Optical coherence tomography," *Science (New York, NY)*, vol. 254, p. 1178, 1991.
- [32] R. J. Winder, P. J. Morrow, I. N. McRitchie, J. Bailie, and P. M. Hart, "Algorithms for digital image processing in diabetic retinopathy," *Computerized Medical Imaging and Graphics*, vol. 33, pp. 608-622, 2009.
- [33] A. Hoover and M. Goldbaum, "Locating the optic nerve in a retinal image using the fuzzy convergence of the blood vessels," *IEEE transactions on medical imaging*, vol. 22, pp. 951-958, 2003.
- [34] M. J. Cree, J. A. Olson, K. C. McHardy, P. F. Sharp, and J. V. Forrester, "The preprocessing of retinal images for the detection of fluorescein leakage," *Physics in medicine and biology*, vol. 44, p. 293, 1999.

- [35] M. Foracchia, E. Grisan, and A. Ruggeri, "Detection of optic disc in retinal images by means of a geometrical model of vessel structure," *IEEE transactions on medical imaging*, vol. 23, pp. 1189-1195, 2004.
- [36] T. Spencer, J. A. Olson, K. C. McHardy, P. F. Sharp, and J. V. Forrester, "An image-processing strategy for the segmentation and quantification of microaneurysms in fluorescein angiograms of the ocular fundus," *Computers and biomedical research*, vol. 29, pp. 284-302, 1996.
- [37] N. P. Ward, S. Tomliivson, and C. J. Taylor, "Image analysis of fundus photographs: the detection and measurement of exudates associated with diabetic retinopathy," *Ophthalmology*, vol. 96, pp. 80-86, 1989.
- [38] G. E. Øien and P. Osnes, "Diabetic retinopathy: Automatic detection of early symptoms from retinal images," in *Proc. Norwegian Signal Processing Sym*, 1995.
- [39] T. Walter and J.-C. Klein, "A computational approach to diagnosis of diabetic retinopathy," in *Proceedings of the 6th Conference on Systemics, Cybernetics and Informatics (SCI2002)*, 2002, pp. 521-526.
- [40] H. Wang, W. Hsu, K. G. Goh, and M. L. Lee, "An effective approach to detect lesions in color retinal images," in *Computer Vision and Pattern Recognition, 2000. Proceedings. IEEE Conference on*, 2000, pp. 181-186.
- [41] A. Osareh, "Automated identification of diabetic retinal exudates and the optic disc," University of Bristol, 2004.
- [42] K. A. Goatman, A. D. Whitwam, A. Manivannan, J. A. Olson, and P. F. Sharp, "Colour normalisation of retinal images," in *Proceedings of Medical Image Understanding and Analysis*, 2003, pp. 49-52.
- [43] A. Osareh, M. Mirmehdi, B. Thomas, and R. Markham, "Automated identification of diabetic retinal exudates in digital colour images," *British Journal of Ophthalmology*, vol. 87, pp. 1220-1223, 2003.
- [44] M. J. Cree, E. Gamble, and D. Cornforth, "Colour normalisation to reduce inter-patient and intra-patient variability in microaneurysm detection in colour retinal images," 2005.
- [45] C. Sinthanayothin, J. F. Boyce, H. L. Cook, and T. H. Williamson, "Automated localisation of the optic disc, fovea, and retinal blood vessels from digital colour fundus images," *British Journal of Ophthalmology*, vol. 83, pp. 902-910, 1999.

- [46] M. J. Cree, E. Gamble, and D. Cornforth, pp. Colour normalisation to reduce inter-patient and intra-patient variability in microaneurysm detection in colour retinal images, 2005.
- [47] D. Usher, M. Dumskyj, M. Himaga, T. Williamson, S. Nussey, and J. Boyce, "Automated detection of diabetic retinopathy in digital retinal images: a tool for diabetic retinopathy screening," *Diabetic Medicine*, vol. 21, pp. 84-90, 2004.
- [48] K. Rapantzikos, M. Zervakis, and K. Balas, "Detection and segmentation of drusen deposits on human retina: Potential in the diagnosis of age-related macular degeneration," *Medical image analysis*, vol. 7, pp. 95-108, 2003.
- [49] M. A. Fadzil, H. A. Nugroho, H. Nugroho, and I. L. Iznita, "Contrast enhancement of retinal vasculature in digital fundus image," in *Digital Image Processing, 2009 International Conference on*, 2009, pp. 137-141.
- [50] E. Daniel and J. Anitha, "Optimum green plane masking for the contrast enhancement of retinal images using enhanced genetic algorithm," *Optik-International Journal for Light and Electron Optics*, vol. 126, pp. 1726-1730, 2015.
- [51] S. Abdelazeem, in *Radio Science Conference, 2002.(NRSC 2002). Proceedings of the Nineteenth National*, 2002, pp. 421-426 Micro-aneurysm detection using vessels removal and circular hough transform.
- [52] R. Klein, S. M. Meuer, S. E. Moss, and B. E. Klein, "Retinal microaneurysm counts and 10-year progression of diabetic retinopathy," *Archives of Ophthalmology*, vol. 113, pp. 1386-1391, 1995.
- [53] L. Ribeiro, S. Nunes, and J. Cunha-Vaz, "Microaneurysm turnover in the macula is a biomarker for development of clinically significant macular edema in type 2 diabetes," *Current Biomarker Findings*, vol. 3, pp. 11-15, 2013.
- [54] B. Lay, C. Baudoin, and J.-C. Klein, "Automatic detection of microaneurysms in retinopathy fluoro-angiogram," in *27th Annual Technical Symposium*, 1984, pp. 165-173.
- [55] C. Baudoin, B. Lay, and J. Klein, "Automatic detection of microaneurysms in diabetic fluorescein angiography," *Revue d'épidémiologie et de santé publique*, vol. 32, pp. 254-261, 1983.
- [56] T. Walter and J.-C. Klein, "Automatic detection of microaneurysms in color fundus images of the human retina by means of the bounding box closing," in *International Symposium on Medical Data Analysis*, 2002, pp. 210-220.

- [57] J. Hipwell, F. Strachan, J. Olson, K. McHardy, P. Sharp, and J. Forrester, "Automated detection of microaneurysms in digital red-free photographs: a diabetic retinopathy screening tool," *Diabetic medicine*, vol. 17, pp. 588-594, 2000.
- [58] A. D. Fleming, S. Philip, K. A. Goatman, J. A. Olson, and P. F. Sharp, "Automated microaneurysm detection using local contrast normalization and local vessel detection," *IEEE Transactions on Medical Imaging*, vol. 25, pp. 1223-1232, 2006.
- [59] T. Spencer, R. P. Phillips, P. F. Sharp, and J. V. Forrester, "Automated detection and quantification of microaneurysms in fluorescein angiograms," *Graefe's archive for clinical and experimental ophthalmology*, vol. 230, pp. 36-41, 1992.
- [60] M. J. Cree, J. A. Olson, K. C. McHardy, J. V. Forrester, and P. F. Sharp, "Automated microaneurysm detection," in *Image Processing, 1996. Proceedings., International Conference on*, 1996, pp. 699-702.
- [61] M. J. Cree, "The waikato microaneurysm detector," *the University of Waikato, Tech. Rep*, 2008.
- [62] G. B. Kande, T. S. Savithri, and P. V. Subbaiah, "Automatic detection of microaneurysms and hemorrhages in digital fundus images," *Journal of digital imaging*, vol. 23, pp. 430-437, 2010.
- [63] G. Gardner, D. Keating, T. Williamson, and A. Elliott, "Automatic detection of diabetic retinopathy using an artificial neural network: a screening tool," *British journal of Ophthalmology*, vol. 80, pp. 940-944, 1996.
- [64] M. Kamel, S. Belkassim, A. M. Mendonca, and A. Campilho, "A neural network approach for the automatic detection of microaneurysms in retinal angiograms," in *Neural Networks, 2001. Proceedings. IJCNN'01. International Joint Conference on*, 2001, pp. 2695-2699.
- [65] C. I. Sánchez, R. Hornero, A. Mayo, and M. García, "Mixture model-based clustering and logistic regression for automatic detection of microaneurysms in retinal images," in *SPIE medical imaging*, 2009, pp. 72601M-72601M-8.
- [66] M. Niemeijer, B. Van Ginneken, M. J. Cree, A. Mizutani, G. Quellec, C. Sánchez, *et al.*, "Retinopathy online challenge: automatic detection of microaneurysms in digital color fundus photographs," *Medical Imaging, IEEE Transactions on*, vol. 29, pp. 185-195, 2010.

- [67] A. Mizutani, C. Muramatsu, Y. Hatanaka, S. Suemori, T. Hara, and H. Fujita, "Automated microaneurysm detection method based on double ring filter in retinal fundus images," in *SPIE medical imaging*, 2009, pp. 72601N-72601N-8.
- [68] L. Giancardo, F. Mériaudeau, T. P. Karnowski, K. W. Tobin, Y. Li, and E. Chaum, "Microaneurysms detection with the radon cliff operator in retinal fundus images," in *SPIE Medical Imaging*, 2010, pp. 76230U-76230U-8.
- [69] L. Giancardo, F. Meriaudeau, T. Karnowski, Y. Li, K. Tobin, and E. Chaum, "Microaneurysm detection with radon transform-based classification on retina images," in *2011 Annual International Conference of the IEEE Engineering in Medicine and Biology Society*, 2011, pp. 5939-5942.
- [70] B. Antal and A. Hajdu, "An ensemble-based system for microaneurysm detection and diabetic retinopathy grading," *IEEE transactions on biomedical engineering*, vol. 59, pp. 1720-1726, 2012.
- [71] G. Quellec, M. Lamard, P. M. Josselin, G. Cazuguel, B. Cochener, and C. Roux, "Optimal wavelet transform for the detection of microaneurysms in retina photographs," *IEEE Transactions on Medical Imaging*, vol. 27, pp. 1230-1241, 2008.
- [72] M. U. Akram, S. Khalid, and S. A. Khan, "Identification and classification of microaneurysms for early detection of diabetic retinopathy," *Pattern Recognition*, vol. 46, pp. 107-116, 2013.
- [73] T. Kauppi, V. Kalesnykiene, J.-K. Kamarainen, L. Lensu, I. Sorri, H. Uusitalo, *et al.*, "DIARETDB0: Evaluation database and methodology for diabetic retinopathy algorithms," *Machine Vision and Pattern Recognition Research Group, Lappeenranta University of Technology, Finland*, 2006.
- [74] R. V. J. P. H. Kälviäinen and H. Uusitalo, "DIARETDB1 diabetic retinopathy database and evaluation protocol," *Medical Image Understanding and Analysis 2007*, p. 61, 2007.
- [75] K. Zuiderveld, "Contrast limited adaptive histogram equalization," in *Graphics gems IV*, 1994, pp. 474-485.
- [76] S. Ravishankar, A. Jain, and A. Mittal, "Automated feature extraction for early detection of diabetic retinopathy in fundus images," in *Computer Vision and Pattern Recognition, 2009. CVPR 2009. IEEE Conference on*, 2009, pp. 210-217.

- [77] A. A. Youssif, A. Z. Ghalwash, and A. S. Ghoneim, "Comparative study of contrast enhancement and illumination equalization methods for retinal vasculature segmentation," *Proc. Cairo International Biomedical Engineering Conferemce*, 2006.
- [78] I. Lazar and A. Hajdu, "Microaneurysm detection in retinal images using a rotating cross-section based model," in *2011 IEEE International Symposium on Biomedical Imaging: From Nano to Macro*, 2011, pp. 1405-1409.
- [79] K. Ram, G. D. Joshi, and J. Sivaswamy, "A successive clutter-rejection-based approach for early detection of diabetic retinopathy," *IEEE Transactions on Biomedical Engineering*, vol. 58, pp. 664-673, 2011.
- [80] S. Wang, H. L. Tang, Y. Hu, S. Sanei, G. M. Saleh, and T. Peto, "Localising Microaneurysms in Fundus Images Through Singular Spectrum Analysis," 2016.
- [81] M. Niemeijer, B. Van Ginneken, J. Staal, M. S. Suttorp-Schulten, and M. D. Abràmoff, "Automatic detection of red lesions in digital color fundus photographs," *IEEE Transactions on medical imaging*, vol. 24, pp. 584-592, 2005.
- [82] Y. Hatanaka, T. Inoue, S. Okumura, C. Muramatsu, and H. Fujita, "Automated microaneurysm detection method based on double-ring filter and feature analysis in retinal fundus images," in *Computer-Based Medical Systems (CBMS), 2012 25th International Symposium on*, 2012, pp. 1-4.
- [83] L. Seoud, T. Hurtut, J. Chelbi, F. Cheriet, and J. P. Langlois, "Red lesion detection using dynamic shape features for diabetic retinopathy screening," *IEEE transactions on medical imaging*, vol. 35, pp. 1116-1126, 2016.
- [84] G. Quellec, M. Lamard, P. M. Josselin, G. Cazuguel, B. Cochener, and C. Roux, "Optimal wavelet transform for the detection of microaneurysms in retina photographs," *Medical Imaging, IEEE Transactions on*, vol. 27, pp. 1230-1241, 2008.
- [85] S. A. A. Shah, A. Laude, I. Faye, and T. B. Tang, "Automated microaneurysm detection in diabetic retinopathy using curvelet transform," *Journal of biomedical optics*, vol. 21, pp. 101404-101404, 2016.
- [86] S. Chaudhuri, S. Chatterjee, N. Katz, M. Nelson, and M. Goldbaum, "Detection of blood vessels in retinal images using two-dimensional matched filters," *Medical Imaging, IEEE Transactions on*, vol. 8, pp. 263-269, 1989.

- [87] A. Hoover, V. Kouznetsova, and M. Goldbaum, "Locating blood vessels in retinal images by piecewise threshold probing of a matched filter response," *Medical Imaging, IEEE Transactions on*, vol. 19, pp. 203-210, 2000.
- [88] M. Al-Rawi, M. Qutaishat, and M. Arrar, "An improved matched filter for blood vessel detection of digital retinal images," *Computers in Biology and Medicine*, vol. 37, pp. 262-267, 2007.
- [89] B. Zhang, L. Zhang, L. Zhang, and F. Karray, "Retinal vessel extraction by matched filter with first-order derivative of Gaussian," *Computers in biology and medicine*, vol. 40, pp. 438-445, 2010.
- [90] M. G. Cinsdikici and D. Aydın, "Detection of blood vessels in ophthalmoscope images using MF/ant (matched filter/ant colony) algorithm," *Computer methods and programs in biomedicine*, vol. 96, pp. 85-95, 2009.
- [91] L. Gang, O. Chutatape, and S. M. Krishnan, "Detection and measurement of retinal vessels in fundus images using amplitude modified second-order Gaussian filter," *Biomedical Engineering, IEEE Transactions on*, vol. 49, pp. 168-172, 2002.
- [92] M. S. Miri and A. Mahloojifar, "Retinal image analysis using curvelet transform and multistructure elements morphology by reconstruction," *Biomedical Engineering, IEEE Transactions on*, vol. 58, pp. 1183-1192, 2011.
- [93] M. Esmaeili, H. Rabbani, A. Mehri, and A. Dehghani, "Extraction of retinal blood vessels by curvelet transform," in *Image Processing (ICIP), 2009 16th IEEE International Conference on*, 2009, pp. 3353-3356.
- [94] J. V. Soares, J. J. Leandro, R. M. Cesar Jr, H. F. Jelinek, and M. J. Cree, "Retinal vessel segmentation using the 2-D Gabor wavelet and supervised classification," *Medical Imaging, IEEE Transactions on*, vol. 25, pp. 1214-1222, 2006.
- [95] M. E. Martínez-Pérez, A. D. Hughes, A. V. Stanton, S. A. Thom, A. A. Bharath, and K. H. Parker, "Retinal blood vessel segmentation by means of scale-space analysis and region growing," in *Medical Image Computing and Computer-Assisted Intervention—MICCAI'99*, 1999, pp. 90-97.
- [96] M. E. Martinez-Perez, A. D. Hughes, S. A. Thom, A. A. Bharath, and K. H. Parker, "Segmentation of blood vessels from red-free and fluorescein retinal images," *Medical image analysis*, vol. 11, pp. 47-61, 2007.

- [97] P. Bankhead, C. N. Scholfield, J. G. McGeown, and T. M. Curtis, "Fast retinal vessel detection and measurement using wavelets and edge location refinement," *PloS one*, vol. 7, p. e32435, 2012.
- [98] M. U. Akram and S. A. Khan, "Multilayered thresholding-based blood vessel segmentation for screening of diabetic retinopathy," *Engineering with computers*, vol. 29, pp. 165-173, 2013.
- [99] D. Cornforth, H. Jelinek, J. Leandro, J. Soares, R. Cesar Jr, M. J. Cree, *et al.*, "Development of retinal blood vessel segmentation methodology using wavelet transforms for assessment of diabetic retinopathy," in *Proc. 8th Asia Pacific Symp. Intell. Evolution. Syst*, 2004, pp. 50-60.
- [100] F. Zana and J.-C. Klein, "Segmentation of vessel-like patterns using mathematical morphology and curvature evaluation," *Image Processing, IEEE Transactions on*, vol. 10, pp. 1010-1019, 2001.
- [101] A. M. Mendonca and A. Campilho, "Segmentation of retinal blood vessels by combining the detection of centerlines and morphological reconstruction," *Medical Imaging, IEEE Transactions on*, vol. 25, pp. 1200-1213, 2006.
- [102] M. Vlachos and E. Dermatas, "Multi-scale retinal vessel segmentation using line tracking," *Computerized Medical Imaging and Graphics*, vol. 34, pp. 213-227, 2010.
- [103] J. J. Leandro, R. M. Cesar Jr, and H. F. Jelinek, "Blood vessels segmentation in retina: Preliminary assessment of the mathematical morphology and of the wavelet transform techniques," in *Computer Graphics and Image Processing, 2001 Proceedings of XIV Brazilian Symposium on*, 2001, pp. 84-90.
- [104] K. A. Vermeer, F. M. Vos, H. Lemij, and A. M. Vossepoel, "A model based method for retinal blood vessel detection," *Computers in Biology and Medicine*, vol. 34, pp. 209-219, 2004.
- [105] S. Roychowdhury, D. D. Koozekanani, and K. K. Parhi, "Blood Vessel Segmentation of Fundus Images by Major Vessel Extraction and Subimage Classification," *Biomedical and Health Informatics, IEEE Journal of*, vol. 19, pp. 1118-1128, 2015.
- [106] Y. Yang, S. Huang, and N. Rao, "An automatic hybrid method for retinal blood vessel extraction," *International Journal of Applied Mathematics and Computer Science*, vol. 18, pp. 399-407, 2008.

- [107] L. Xu and S. Luo, "A novel method for blood vessel detection from retinal images," *Biomedical engineering online*, vol. 9, p. 14, 2010.
- [108] S. Wang, Y. Yin, G. Cao, B. Wei, Y. Zheng, and G. Yang, "Hierarchical retinal blood vessel segmentation based on feature and ensemble learning," *Neurocomputing*, vol. 149, pp. 708-717, 2015.
- [109] Y. Zhao, L. Rada, K. Chen, S. P. Harding, and Y. Zheng, "Automated Vessel Segmentation Using Infinite Perimeter Active Contour Model with Hybrid Region Information with Application to Retinal Images," *Medical Imaging, IEEE Transactions on*, vol. 34, pp. 1797-1807, 2015.
- [110] B. S. Y. Lam and H. Yan, "A novel vessel segmentation algorithm for pathological retina images based on the divergence of vector fields," *IEEE Transactions on Medical Imaging*, vol. 27, pp. 237-246, 2008.
- [111] A. Salazar-Gonzalez, D. Kaba, Y. Li, and X. Liu, "Segmentation of the blood vessels and optic disk in retinal images," *Biomedical and Health Informatics, IEEE Journal of*, vol. 18, pp. 1874-1886, 2014.
- [112] J. I. Orlando and M. Blaschko, "Learning fully-connected CRFs for blood vessel segmentation in retinal images," in *Medical Image Computing and Computer-Assisted Intervention—MICCAI 2014*, ed: Springer, 2014, pp. 634-641.
- [113] G. Azzopardi, N. Strisciuglio, M. Vento, and N. Petkov, "Trainable COSFIRE filters for vessel delineation with application to retinal images," *Medical image analysis*, vol. 19, pp. 46-57, 2015.
- [114] W. S. Oliveira, J. V. Teixeira, T. I. Ren, G. D. Cavalcanti, and J. Sijbers, "Unsupervised Retinal Vessel Segmentation Using Combined Filters," *PloS one*, vol. 11, p. e0149943, 2016.
- [115] Y. Zhao, Y. Liu, X. Wu, S. P. Harding, and Y. Zheng, "Retinal vessel segmentation: An efficient graph cut approach with retinex and local phase," *PloS one*, vol. 10, p. e0122332, 2015.
- [116] S. Theodoridis and K. Koutroumbas, "Pattern Recognition, Academic Press," *New York*, 1999.
- [117] R. O. Duda, P. E. Hart, and D. G. Stork, *Pattern classification*: John Wiley & Sons, 2012.
- [118] J. V. Soares, J. J. Leandro, R. M. Cesar, H. F. Jelinek, and M. J. Cree, "Retinal vessel segmentation using the 2-D Gabor wavelet and supervised

- classification," *IEEE Transactions on medical Imaging*, vol. 25, pp. 1214-1222, 2006.
- [119] J. Staal, M. D. Abràmoff, M. Niemeijer, M. A. Viergever, and B. Van Ginneken, "Ridge-based vessel segmentation in color images of the retina," *Medical Imaging, IEEE Transactions on*, vol. 23, pp. 501-509, 2004.
- [120] S. S. A. Ali, T. B. Tang, A. Laude, and I. Faye, "Making every microaneurysm count: A hybrid approach to monitor progression of diabetic retinopathy," in *Intelligent and Advanced Systems (ICIAS), 2014 5th International Conference on*, 2014, pp. 1-4.
- [121] L. d. F. D. Costa and R. M. Cesar Jr, *Shape analysis and classification: theory and practice*: CRC Press, Inc., 2000.
- [122] A. R. Smith, "Color gamut transform pairs," *ACM Siggraph Computer Graphics*, vol. 12, pp. 12-19, 1978.
- [123] O. Tankyevych, "Filtering of thin objects: applications to vascular image analysis," Université Paris-Est, 2010.
- [124] A. F. Frangi, W. J. Niessen, K. L. Vincken, and M. A. Viergever, "Multiscale vessel enhancement filtering," in *Medical Image Computing and Computer-Assisted Intervention—MICCAI'98*, ed: Springer, 1998, pp. 130-137.
- [125] E. Candes, L. Demanet, D. Donoho, and L. Ying, "Fast discrete curvelet transforms," *Multiscale Modeling & Simulation*, vol. 5, pp. 861-899, 2006.
- [126] T. Guha and Q. J. Wu, *Curvelet based feature extraction*: INTECH Open Access Publisher, 2010.
- [127] L. Dettori and L. Semler, "A comparison of wavelet, ridgelet, and curvelet-based texture classification algorithms in computed tomography," *Computers in biology and medicine*, vol. 37, pp. 486-498, 2007.
- [128] M. M. Eltoukhy, I. Faye, and B. B. Samir, "Breast cancer diagnosis in digital mammogram using multiscale curvelet transform," *Computerized Medical Imaging and Graphics*, vol. 34, pp. 269-276, 2010.
- [129] B. Li and M. Q.-H. Meng, "Texture analysis for ulcer detection in capsule endoscopy images," *Image and Vision computing*, vol. 27, pp. 1336-1342, 2009.
- [130] T. Spencer, R. P. Phillips, P. F. Sharp, and J. V. Forrester, *Graefe's archive for clinical and experimental ophthalmology*, vol. 230, pp. 36-41 Automated detection and quantification of microaneurysms in fluorescein angiograms, 1992.

- [131] T. Walter, P. Massin, A. Erginay, R. Ordonez, C. Jeulin, and J.-C. Klein, *Medical image analysis*, vol. 11, pp. 555-566 Automatic detection of microaneurysms in color fundus images, 2007.
- [132] I. Lazar and A. Hajdu, *Medical Imaging, IEEE Transactions on*, vol. 32, pp. 400-407 Retinal microaneurysm detection through local rotating cross-section profile analysis, 2013.
- [133] I. Lazar, A. Hajdu, and R. Quareshi, in *8th International Conference on Applied Informatics*, 2010, p. Retinal microaneurysm detection based on intensity profile analysis.
- [134] D. Marín, A. Aquino, M. E. Gegúndez-Arias, and J. M. Bravo, "A new supervised method for blood vessel segmentation in retinal images by using gray-level and moment invariants-based features," *Medical Imaging, IEEE Transactions on*, vol. 30, pp. 146-158, 2011.
- [135] A. P. Witkin, "Scale-space filtering: A new approach to multi-scale description," in *Acoustics, Speech, and Signal Processing, IEEE International Conference on ICASSP'84.*, 1984, pp. 150-153.
- [136] J. J. Koenderink, "The structure of images," *Biological cybernetics*, vol. 50, pp. 363-370, 1984.
- [137] A. F. Frangi, W. J. Niessen, K. L. Vincken, and M. A. Viergever, "Multiscale vessel enhancement filtering," in *International Conference on Medical Image Computing and Computer-Assisted Intervention*, 1998, pp. 130-137.
- [138] B. W. Matthews, "Comparison of the predicted and observed secondary structure of T4 phage lysozyme," *Biochimica et Biophysica Acta (BBA)-Protein Structure*, vol. 405, pp. 442-451, 1975.
- [139] M. E. Gegúndez-Arias, A. Aquino, J. M. Bravo, and D. Marin, "A function for quality evaluation of retinal vessel segmentations," *Medical Imaging, IEEE Transactions on*, vol. 31, pp. 231-239, 2012.
- [140] M. Niemeijer, J. Staal, B. van Ginneken, M. Loog, and M. D. Abramoff, "Comparative study of retinal vessel segmentation methods on a new publicly available database," in *Medical Imaging 2004*, 2004, pp. 648-656.
- [141] M. M. Fraz, P. Remagnino, A. Hoppe, B. Uyyanonvara, A. R. Rudnicka, C. G. Owen, *et al.*, "An ensemble classification-based approach applied to retinal blood vessel segmentation," *IEEE Transactions on Biomedical Engineering*, vol. 59, pp. 2538-2548, 2012.

- [142] X. Jiang and D. Mojon, "Adaptive local thresholding by verification-based multithreshold probing with application to vessel detection in retinal images," *IEEE Transactions on Pattern Analysis and Machine Intelligence*, vol. 25, pp. 131-137, 2003.
- [143] M. E. Martinez-Perez, A. D. Hughes, A. V. Stanton, S. A. Thom, A. A. Bharath, and K. H. Parker, "Segmentation of retinal blood vessels based on the second directional derivative and region growing," in *Image Processing, 1999. ICIP 99. Proceedings. 1999 International Conference on*, 1999, pp. 173-176.
- [144] B. Al-Diri, A. Hunter, and D. Steel, "An active contour model for segmenting and measuring retinal vessels," *IEEE Transactions on Medical imaging*, vol. 28, pp. 1488-1497, 2009.
- [145] Q. Li, J. You, and D. Zhang, "Vessel segmentation and width estimation in retinal images using multiscale production of matched filter responses," *Expert Systems with Applications*, vol. 39, pp. 7600-7610, 2012.
- [146] X. Yin, B. W. Ng, J. He, Y. Zhang, and D. Abbott, "Accurate image analysis of the retina using hessian matrix and binarisation of thresholded entropy with application of texture mapping," *PloS one*, vol. 9, p. e95943, 2014.
- [147] M. D. Abràmoff, Y. Lou, A. Erginay, W. Clarida, R. Amelon, J. C. Folk, *et al.*, "Improved Automated Detection of Diabetic Retinopathy on a Publicly Available Dataset Through Integration of Deep LearningDeep Learning Detection of Diabetic Retinopathy," *Investigative Ophthalmology & Visual Science*, vol. 57, pp. 5200-5206, 2016.
- [148] M. Coster and J.-L. Chermant, "Image analysis and mathematical morphology for civil engineering materials," *Cement and Concrete Composites*, vol. 23, pp. 133-151, 2001.
- [149] R. Fisher, S. Perkins, A. Walker, and E. Wolfart, "Hypermedia image processing reference," *Department of Artificial Intelligence, University of Edinburgh*, 1994.

APPENDIX A

LIST OF PUBLICATION

Journal Publications

1. Shah, Syed Ayaz Ali, et al. "Automated microaneurysm detection in diabetic retinopathy using Curvelet transform." *Journal of biomedical optics* 21.10 (2016): 101404-101404. (IF:2.55,Q1)
2. Shah, Syed Ayaz Ali, et al. "Blood vessel segmentation in color fundus images based on regional and Hessian features." *Graefe's Archive for Clinical and Experimental Ophthalmology* (2017): 1-9. (IF:1.99,Q2)

Conference Publications

1. Shah, Syed Ayaz Ali, et al. "Automated Detection of Microaneurysms Using Curvelet Transform." *Investigative Ophthalmology & Visual Science* 56.7 (2015): 5266-5266.
2. Ali, Shah Syed Ayaz, et al. "Making every microaneurysm count: A hybrid approach to monitor progression of diabetic retinopathy." *Intelligent and Advanced Systems (ICIAS), 2014 5th International Conference on*. IEEE, 2014.

APPENDIX B

FUNDUS IMAGES DATASETS

Some of the well-known datasets for evaluation of the Blood Vessel segmentation

- I. DRIVE: DRIVE which stands for Digital Retinal Images for Vessel Extraction is publically available dataset. It enables comparative studies on segmentation of blood vessels in retinal images. Forty images are randomly selected from 400 images from a diabetic retinopathy screening program in The Netherlands. Out of these forty images, seven images show signs of mild early diabetic retinopathy. Each image has been JPEG compressed. These 40 images are divided into 20 training images and 20 test images. The dataset can be downloaded from:

<http://www.isi.uu.nl/Research/Databases/DRIVE/>

- II. STARE: STructured Analysis of the Retina (STARE) is publically available dataset for blood vessel segmentation. It contains 20 images with ground truth. Out of the 20 images, 10 images contain retinal abnormality. The dataset can be downloaded from:

<http://cecas.clemson.edu/~ahoover/stare/>

- III. CHASE DB: Child Heart And Health Study in England (CHASE) is another publically available dataset for blood vessel segmentation. It consists of 28 images of UK children of different origins. It is a detailed investigation of patterns of risk factors for cardiovascular disease and type 2 diabetes. The dataset can be downloaded from:

<http://www.chasestudy.ac.uk/>

Some of the well-known datasets for evaluation of the Microaneurysm detection

- I. ROC: Retinopathy Online Challenge (ROC) is publically available dataset for microaneurysm (MA) detection. 100 images are selected from 150,000 images. The images are taken at multiple resolution. Therefore MA detection is very challenging task in ROC dataset. Following is the link to download the dataset:

<http://webeye.ophth.uiowa.edu/ROC/>

- IV. DIARETDB: Diabetic Retinopathy Database (DIARETDB) is another publically available dataset. It consists of 89 color images. Out of 89, 84 images

contains MA while 5 of the images does not contain any diabetic retinopathy signs. Images are taken at single resolution. The dataset can be downloaded from:

<http://www.it.lut.fi/project/imageret/diaretdb1/>

- II. MESSIDOR :Methods to evaluate segmentation and indexing techniques in the field of retinal ophthalmology or Messidor dataset is another publically available dataset. It is composed of 1200 color fundus images acquired using a variety of retinographs. Medical experts provide two diagnoses for each image ie Retinopathy grade and Risk of macular edema. Following is the link for dataset:

<http://www.adcis.net/en/Download-Third-Party/Messidor.html>

APPENDIX C

TECHNICAL TERMS

A confusion matrix is basically a table where the performance of a classifier is described and or visualized. It consists of rows and columns. The values in columns are the predicted values of a classifier whereas those in rows are the actual values. In the current research work (for MA detection and blood vessel segmentation), we have a two-class problem i.e. in case of automated MA detection it can be MA or non-MA or in case of BV segmentation it can be BV or non-BV. Therefore, the confusion matrix is formed for two-class problem only. As shown in the Figure C below, for two-class or binary classification problem, it consists of two rows and two columns.

		Predicted	
		Class A	Class B
Actual Class	Class A	$T_N = 50$	$F_P = 10$
	Class B	$F_N = 5$	$T_P = 100$

Figure C: Confusion matrix

The predicted value of a classifier can be True Positive, False Positive, True Negative or False Negative.

True Positive (T_P): classifier predicts Class B and actually, it is Class B.

False Positive (F_P): classifier predicts Class B and actually, it is Class A

True Negative (T_N): classifier predicts Class A and actually, it is Class A

False Negative (F_N): classifier predicts Class A and actually, it is Class B

Sensitivity or True Positive Rate (TPR): Fraction of class B correctly classified as class B.

Mathematically it can be described as:

$$\text{Sensitivity or TPR} = \frac{TP}{TP+FN} \quad (C.1)$$

Based on values in the confusion matrix, sensitivity is 0.952 (100/105)

Specificity: Fraction of class A correctly classified class A. Mathematically it can be described by:

$$\text{Specificity} = \frac{T_N}{T_N+F_P} \quad (C.2)$$

Based on values in the confusion matrix, specificity is 0.833 (50/60)

False Positive Rate (FPR): Fraction of class A incorrectly classified as class B.

Mathematically it can be described by:

$$FPR = \frac{F_P}{F_P + T_N} \text{ or } (1 - \text{Specificity}) \quad (C.3)$$

Based on values in the confusion matrix, FPR is 0.167 (10/60)

Average number of False Positives Per Image (FPPI): Average number of false positives per image is defined as the total number of false positives in all the images divided by total number of images. For example in dataset of 10 images, if there are 250 false positives detected in total, then the FPPI will be 25 (250/10).

Mathematical morphology

In case of mathematical morphology, images are treated as a set and by probing the image with a known shape, desired objects are extracted. This probing shape is called the Structuring Element (SE) [148]. The SE can have different shapes and sizes depending upon the objects to be extracted as shown in Figure C.1. The origin of SE is marked by a ring. In each case the origin is marked by a ring around that point. Note that for illustration purpose, Figures explaining dilation, erosion and opening are on binary images.

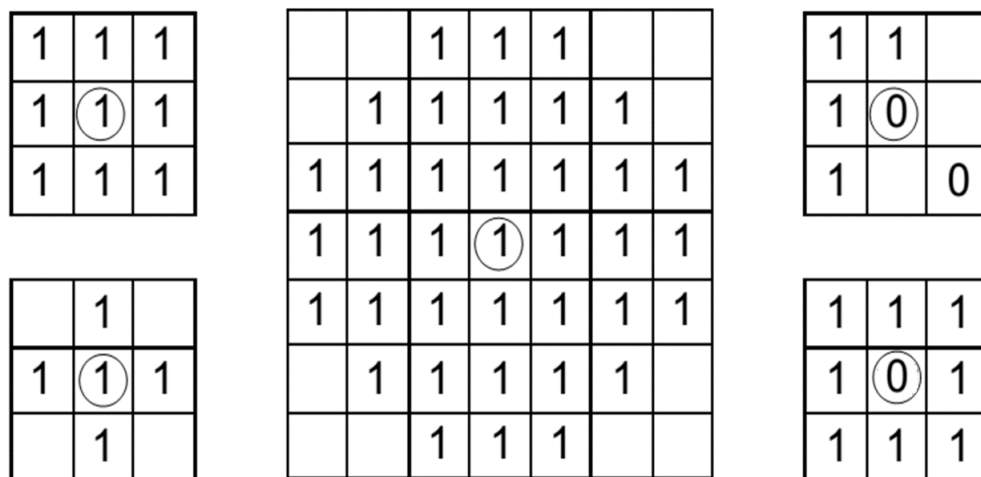


Figure C.1 : Examples of different structuring elements

To understand Top Hat Transform (THT), we need to define the following operators:

1. Morphological Dilation: This morphological operation causes objects to grow in size. How much and how it will grow depends on the SE. Let's say we have image A and structuring element B, dilation of A by B can be described as :

$$A \oplus B = \{Z | (\hat{B})_z \cap A \neq \emptyset\} \quad (C.4)$$

where \hat{B} : the reflection of B about its origin and shifting this reflection by z. The effect of this operator is to enlarge the foreground pixel boundaries gradually. This results in growth of foreground pixels and making holes smaller within those regions, as shown in Figure C.2. In case of grayscale image, dilation corresponds to local maximum over the area defined by the structure element.

2. Morphological Erosion: This morphological operation causes objects to shrink. And similar to morphological dilation, it also depends upon SE. The operation of erosion for image A by SE B is defined as

$$A \ominus B = \{z | (\hat{B})_z \subseteq A\} \quad (C.5)$$

To find the erosion of an image, each of the foreground pixels is considered in turn. For each foreground pixel, SE is superimposed on top of the image such that the origin of the SE coincides with the input pixel coordinates. If all the pixels under the SE are foreground pixels, then the corresponding pixel in the image is kept as it is otherwise it is set to background pixel. Figure C.3 illustrates the operation of erosion. While in case of grayscale image, erosion corresponds to local minimum over the area defined by the structure element.

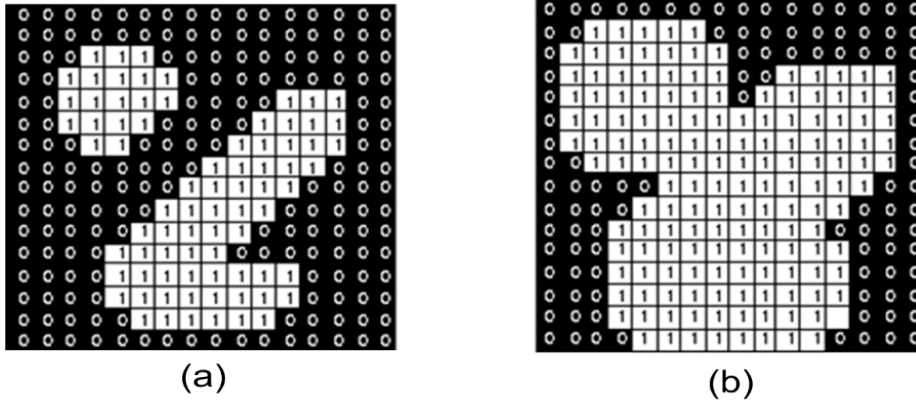


Figure C.2: Morphological dilation with 3x3 square structuring element. (a) Original image (b) image obtained after dilation by 3x3 square element [149]

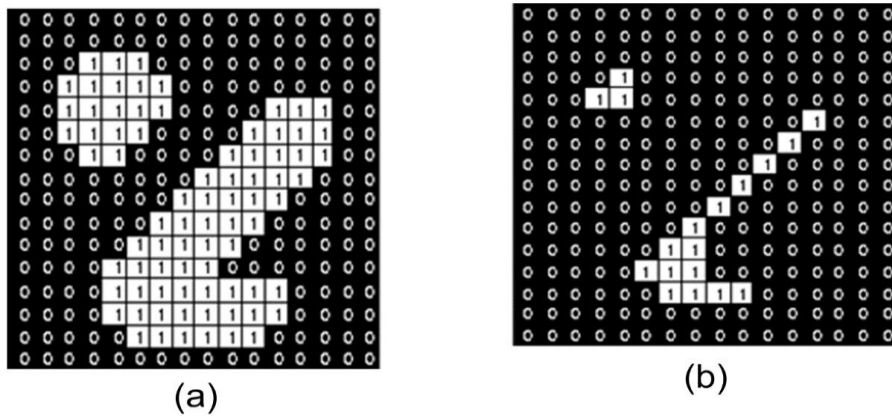


Figure C.3: Morphological Erosion. (a) Original object (b) Using a 3x3 square SE, a layer of pixels have been stripped away from an object [149]

3. Morphological Opening: An opening is defined as an erosion followed by a dilation using the same structuring element for both operations. The opening operator therefore requires two inputs: an image to be opened, and a structuring element. Mathematically, it can be described as:

$$\begin{aligned}
 A \circ B &= (A \ominus B) \oplus B \\
 A \circ B &= \cup \{(B)_z \mid (B)_z \subseteq A\}
 \end{aligned}
 \tag{C.6}$$

Shown in Figure C.4, left (original image) and right is the result of binary opening using 3x9 and 9x3 structuring elements respectively.

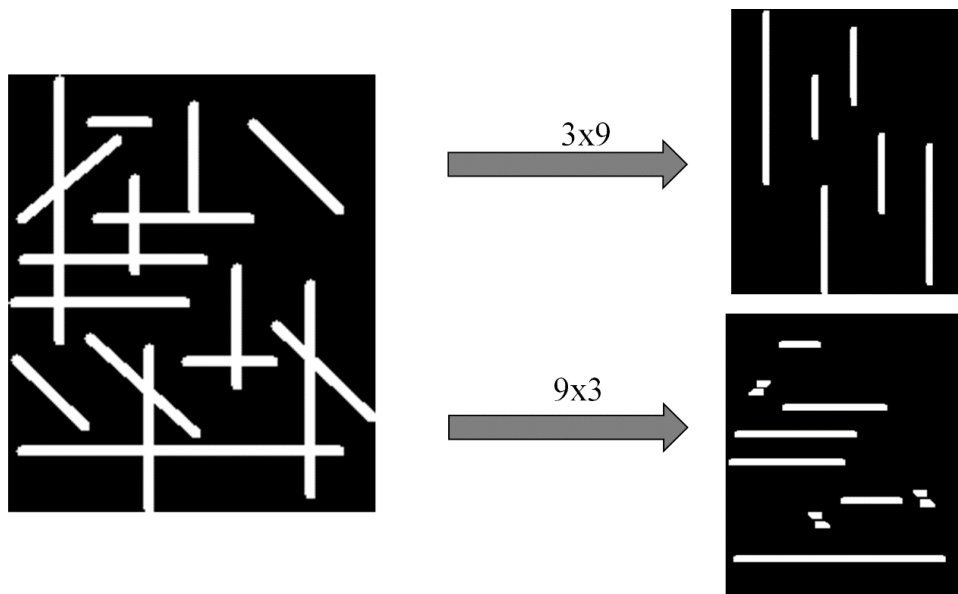


Figure C.4: Opening by 3x9 and 9x3 respectively [149]

4. Morphological Closing: It is defined as dilation followed by erosion using the same structuring element. It smoothens sections of contours but it generally fuses narrow breaks and long thin gulfs, eliminates small holes, and fills gaps in the contour. Opening is the opposite of closing, i.e. opening the foreground pixels with a particular structuring element is equivalent to closing the background pixels with the same element. Mathematically it can be described as:

$$A \bullet B = (A \oplus B) \ominus B \quad (C.7)$$